Dissertation
submitted to the
Combined Faculties for the Natural Sciences and Mathematics
of the Ruperto-Carola University of Heidelberg, Germany
for the degree of
Doctor of Natural Sciences

put forward by
Dipl.–Phys. Karsten Staack
born in Finsterwalde
oral examination: 6. November 2013

Image Analysis of Microfluidic Flows Using Partial Differential Equations

Submission date 23. September 2013
Referees PD Dr. rer. nat. Christoph Sebastian Garbe
Prof. Dr. rer. nat. Rolf Rannacher

Abstracts

This thesis deals with advanced models to characterize microfluidic flows from image sequences. The governing equations and boundary conditions for viscous flows are introduced as a global model in order to impose physically sound motion results. The connection between the computational fluid simulations and experimental measurement data is established by using constrained optimization. This framework also allows to introduce control variables, which are determined in agreement with the underlying data.
In this context, the thesis focuses on the study of the influence of i) the image data, ii) the underlying motion and iii) the boundary conditions on the estimation of the control variables and the corresponding physical quantities. These questions are assessed by the application to synthetic images that allow to measure the induced errors. It is shown that the application of physically motivated differential equations as global motion models increase the robustness and accuracy of the motion estimation. Control variables are used to change the equations in a modeled manner, so that the solution describes the processes that are inherent in the images. The strength of global models lies in the combination with sparsely distributed information in the images, where common state-of-the-art methods have extreme difficulties to obtain reasonable results. It is demonstrated that the optimal control framework allows to relax the governing equations in order to model uncertainty of the measurement setting parameters, such as wall-slip. And finally, such a parameter model is extended to three dimensions and allows to estimate the pressure drop of the flow and the diffusion coefficient of the trace substance *caged Q-rhodamine dextran* in water.

Diese Arbeit befasst sich mit der verbesserten Modellierungen von Mikrokanalströmungen, die eine genauere Charakterisierung durch Bildsequenzen ermöglicht. Die geltenden Gesetzmäßigkeiten und Randbedingungen werden als globales Model verwendet, um physikalisch plausible Resultate des Bewegungsfeldes zu erzielen. Die Kombination von Strömungssimulationen und experimentellen Messdaten wird durch die Verwendung von Optimierungsmethoden unter Nebenbedingungen erreicht. Dieser Ansatz erlaubt die Einführung von Kontrolvariablen, die in Übereinstimmung zu den Messdaten bestimmt werden.
In diesem Zusammenhang konzentriert sich diese Arbeit auf die Untersuchung der Einflüsse durch i) die Bilddaten, ii) das zugrunde liegende Bewegungsfeld und iii) die Randbedingungen auf die Kontrolvariablen und die dadurch bestimmten physikalischen Größen. Diese Fragenstellungen werden mit synthetischen Bilddaten quantitativ erfasst und erlauben somit eine Abschätzung der Genauigkeit. Es wird gezeigt, dass die Verwendung von Stömungsgleichungen als Bewegungsmodel die Robustheit und Genauigkeit der Geschwindigkeitsbestimmung aus Bildern verbessert. Kontrollvariablen werden verwendet um die Lösungen der Gleichungen in geeigneter Weise zu verändern, so dass diese die Prozesse in den Bildern beschreiben. Die Stärke von globalen Bewegungsmodellen beruht auf der Tatsache, dass wenige vereinzelte Bildinformationen für eine sinnvolle Bestimmung ausreichen, wogegen Methoden mit lokalen Bewegungsmodellen große Probleme haben. Es wird gezeigt, dass mit Hilfe von optimaler Steuerung die physikalischen Gesetze abgeschwächt werden können, um Ungenauigkeiten der gegebenen Referenzeparameter zu modellieren. Und schließlich wird der Ansatz auf drei Dimensionen erweitert, was eine Bestimmung des Druckabfalls und des Diffusionskoeffizienten vom Farbstoff *caged Q-rhodamine dextran* in Wasser aus Fluoreszenzmessbilden ermöglicht.

Acknowledgements

First and foremost I would like to express my sincere gratitude to my supervisor Christoph Garbe, who gave me the chance to write this thesis as a member of his research group. I am grateful for all his contributions of time, ideas, encouragements and fundings that made this Ph.D. possible. I appreciate that he provided many interesting research opportunities and always left sufficient space to develop individual ideas.

Furthermore, I like to thank Prof. Rannacher, who agreed to write the second review for this thesis and to be a member of my examination committee.

Of course, I would like to thank the HGS MathComp for the scholarship that made it possible to start this study and the additional fundings for attending conferences that broadened my scientific field of view.

Fruitful discussions have been made with my two colleagues Matthias Klinger and Jevgeni Vihharev, that allowed a vivid exchange of knowledge during my Ph.D. time. They were always open to answer patiently my mathematical and numerical questions.

I want to thank the people from the HCI department, especially the secretaries Tanja, Barbara, Karin and Evelyn and the computer administrator Jürgen Moldenhauer, who helped to organize and manage the fundamental things that are related to this work. Moreover, my colleagues from the Image Processing and Modeling Group but also the people from the Research Group Graphical Model earn my acknowledgment for making this time memorable.

Special credit deserve my colleagues Henrik Schäfer, Julian Stampf, Jana Schnieder and Bernhard Schmitzer, who probably did not know what they were up to, when they generously offered to check the spelling this thesis. Thanks very much for helping with this tedious work.

Last but not least I want to say thank you to my family, who always had confidence in me and gave me not only moral support to achieve my goals. Not yet officially part of the family, I want to thank Kerstin for being there, supporting me, distracting me, believing in me and giving me power to follow my course.

Karsten Staack
University of Heidelberg
August 2013

Contents

List of Figures

Nomenclature

α	regularizing parameter	K	diffusivity
β	slip length	Kn	Knudsen number
δp	pressure drop	$\mathcal{L}$	Lagrangian function
ℓ	length scale	$\mathscr{L}$	likelihood function
κ	diffusion coefficient	L	length of the domain
κ_{Tay}	Taylor dispersion	$\boldsymbol{M}$	stiffness matrix
Λ	diagonal matrix	$\boldsymbol{e}$	eigenvector $\boldsymbol{e} = (e_1, e_2, e_3)^T$
λ	mean free path length between molecules or eigenvalues of a matrix	$\boldsymbol{n}$	wall normal
		$\mathcal{N}$	normal distribution
μ	dynamic viscosity	n	number of dimensions
ν	kinematic viscosity	N	number of images in a sequence
ϕ	test function	p	pressure
ρ	fluorescence density	Pe	Péclet number
σ	standard deviation	pdf	probability density function
σ_v	tangential momentum accommodation coefficient	$\boldsymbol{Q}$	orthogonal matrix
		Q	flow rate
ε	small real number	q	control parameter
$\boldsymbol{a}$	vector of equality constraints	Re	Reynolds number
c	scaling factor	$\boldsymbol{S}$	structure tensor in image processing
$\boldsymbol{d}$	displacement	s	scaling parameter
$\boldsymbol{f}$	external force	t	time coordinate
Fr	Froud number	$\boldsymbol{u}$	velocity $(u, v)^T$ or $(u, v, w)^T$
func	general function	$\boldsymbol{u}_e$	extended velocity $(u, v, 1)^T$
$\boldsymbol{G}$	mass matrix	U	reference velocity
$\boldsymbol{H}$	Hessian	$\boldsymbol{u}_{slip}$	slip velocity at the wall
H	height of the domain	$\boldsymbol{u}_{wall}$	velocity of the wall
I	image or image sequence	W	width of the domain
j	reduced cost functional	w	weighting function
J	cost functional	$\boldsymbol{x}$	spatial coordinate
$\boldsymbol{k}$	wave number	$\boldsymbol{z}$	adjoint or dual variable

Spaces & Sets

$\emptyset$	empty set
Γ	border segment of a domain
Ω	image domain
Ω_3	volume domain
$\partial\Omega$	boundary of Ω
$\mathcal{C}$	set of constraints
H^1	Sobolev vector space
$\mathcal{I}$	intensity domain
L^2	vector space of square-integrable functions
$\mathcal{N}$	local neighborhood
$\mathcal{O}$	complexity class, limiting behavior
$\mathbb{R}^n$	vector space of real numbers
S_h	finite dimensional vector space
T	time domain
$\mathcal{U}$	vector space of velocity fields
X	normed vector space
Y	normed vector space

Operators

∂_a	partial derivative with respect to a
ψ	norm
φ	norm
$\mathbb{1}$	identity mapping
$\|\cdot\|_\infty$	maximum norm
$\|\cdot\|_1$	absolute norm
$\|\cdot\|_2$	Euclidean norm
$\star$	one-dimensional convolution
$*$	two-dimensional convolution
Δ	Laplace operator
∇_3	spatio-temporal gradient operator
∇	gradient operator
div	divergence operator
curl	vorticity operator
$\hat{D}$	displacement operator
G_σ	Gaussian function with std deviation σ
$\hat{L}$	second-order differential operator
$\hat{P}^\downarrow$	projection operator
$\hat{P}^\uparrow$	reconstruction operator
S	solution operator in optimization

Indices

$_0$	initial state at t_0
$_{12}$	first and second component of the variable
$'_a$	derivative with respect to a
$\overline{}$	averaged quantity
δ	small variation
*	optimal solution state or non-dimensional variable
$^\perp$	perpendicular
^{T}	transpose
$\tilde{}$	Fourier transformed
$_i$	variable at time t_i
$_{max}$	maximum of the variable
$_n$	normal derivative
$_{ref}$	reference variable
$_t$	time derivative
$_{x,y,z}$	spatial derivatives

Abbreviations

2D2C	two dimensions and two components
3D3C	three dimensions and three components
BCCE	brightness constancy constraint equation
CFD	computational fluid dynamics
CG	conjugate gradient method
FE	finite element
FEM	finite element method
IW	interrogation window for PIV
LIF	laser induced fluorescence
LPS	local projection stabilization
MTV	molecular tagging velocimetry
OF	optical flow
PDE	partial differential equation
pdf	probability density function
PIV	particle image velocimetry
px	pixels
Q_1	linear quadrilateral finite element
SNR	signal-to-noise ratio
SSD	sum of squared differences
s.t.	subject to

CHAPTER 1

Introduction

1.1 Motivation

The characterization and accurate description of dynamical processes are among the most interesting topics in the field of physics. In order to understand these processes it is necessary to observe the kinematic behavior and conclude physical properties and models. In this context motion takes a key role because it describes the change of position of objects or more general matter in time.

The measurement of kinematic properties is of special interest for fluid dynamical questions. Figure 1.1 shows the wide range of relevant flows on earth that are of scientific interest. For many relevant cases the accurate characterization and prediction of dynamical systems is not possible because their governing equations are non-linear and the initial state of the system or the exact boundary conditions are not known precisely enough. For many flow phenomena it is not possible to develop models that describe the

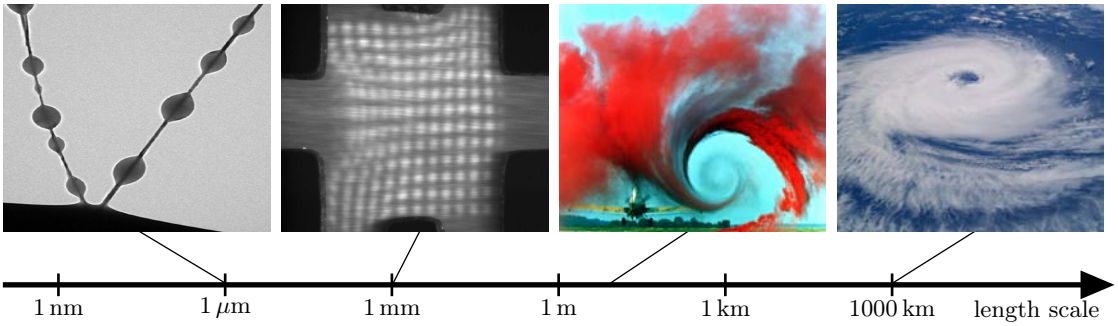

Figure 1.1: This scheme illustrates the wide range of length scales for flow phenomena on earth, which covers up more than 9 orders of magnitude. Starting from nano-flows (Huang et al., 2013, Courtesy of Yu-Chieh Lo), micro-flows (Roetmann, 2008, Courtesy of Laser-Laboratorium Göttingen e.V.), moderate-scale flows (NASA, 1994) up to large-scale flows (NASA, 2004).

behavior sufficiently accurate because the system is too complex. Simplifications help to find mathematical descriptions of the phenomena but often these approximations are not accurate enough to predict dynamical processes. As a consequence, it is quite common to conduct experiments as a means to verify numerically simulated results. With respect to aerodynamics or environmental physics, the standard procedure of estimating quantities of interest include scaled model experiments besides numerical evaluations. Whenever necessary and possible a field test is also conducted to dismiss all doubts about deficiencies of the laboratory experiments and numerical results.

Simplified fluid motion models make use of corrections that include empirical constants and terms that make up for the inadequate modeling (e.g. Reynolds stress models). The following list gives a selection of challenging fluid phenomena, which are not only of scientific interest but also relevant for engineers in order to optimize the performance of processes and products:

- fluid-structure interaction (e.g. bird flight, pumping heart)
- multiphase flows (e.g. sprays)
- reacting flows (e.g. combustion)
- fluid interfaces (e.g. wind-wave interaction)
- aerodynamic flows (e.g. airplanes)
- atmospheric flows (e.g. weather forecast, hurricane trajectories)
- turbulence (e.g. jets, wake) .

For all these problems experimental assessment is necessary in order to verify numerical results and to determine properties and relationships that help to improve state-of-the-art models while increasing the accuracy of the estimate. This is certainly relevant for flows that have to be described by time-dependent, non-linear models (e.g. aerodynamics) but it also applies to stationary linear models as in microfluidics. Measurements help to tell whether model assumptions are justifiable or should be adapted to match the experiment and of course reality.

The velocity is one of the crucial quantities that describes the kinematics and is therefore the main subject of most investigations. An accurate and robust assessment of the velocity is mandatory in order to validate existing dynamical models or to improve them. Most often motion estimation from experimental data is based on local motion models (e.g. differential models) that do not include a global description of the flow. Such global relations can be exploited to achieve higher accuracies and robustness and allow to estimate physically sound results. However, the combination of fluid simulation and fluid measurements is highly desirable because it allows to benefit from both fields: the comprehensive knowledge of all physical quantities from the simulation and the fidelity from experimental data.

1.2 Previous work

In the beginning, photographs were mostly used for visualizing flows in order to get a qualitative understanding of the kinematics. The books of Merzkirch (1987) and Samimy et al. (2003) show a large variety of flow visualization methods. These images are well suited for estimating geometries, orientations and length scales of flow structures, but

the accuracy of quantitative evaluations of the motion was limited. From a current point of view, many of these visualizations seem rather artistic than an actual scientific measurement (Gharib et al., 2002). Since these visualization images were not suitable for quantitative investigations, scientists started to generate highly structured images by introducing tracer particles into the fluid. The fluid acts as a carrier medium for the dispersed particles that follow the fluid motion and can be tracked. The velocity was locally estimated by an optical measurement technique called *Young's Fringe* method (Meynart, 1983; Arnold and Hinsch, 1989; Keane and Adrian, 1990), which analyses interference patterns that encode the velocity. With the advent of digital images in the early 90's this technique was imitated on computers and became known as particle image velocimetry (Adrian, 1991; Willert and Gharib, 1991). This was the first motion estimation method acting on digital images that could estimate fluid motion quantitatively.

But motion estimation is not just important for fluid dynamicists but also to computer scientists, whose aim is to estimate object or camera motions. More than 10 years before the fluid dynamicists, the computer vision community had already developed methods to estimate motion from images, which they called *optical flow* (OF) (Horn and Schunck, 1981; Lucas and Kanade, 1981). Optical flow is very flexible because it is based on a cost function that can be easily adapted to model the underlying effects that describe the evolution of the image sequences structures.

Just recently, before the turn of the millennium, these methods have been rediscovered for fluid motion estimation (Wildes et al., 1997; Quénot et al., 1998) and have been extended to deal with individual characteristics of the recorded scene. The standard optical flow method is a differential method, which assumes the conservation of image intensity. Therefore, it is very sensitive to illumination changes, which will be interpreted wrongly as motion (Horn, 1986). In order to account for this effect Gennert and Negahdaripour (1987) introduced additional brightness terms that model contrast changes and mean intensity shifts. A generalized illumination model was presented by Haußecker and Fleet (2001), which uses a parameterized model function to describe the brightness changes along one streamline. With this model, it was possible to include physical processes as exponential decay or diffusion into the motion estimation. Much effort has been done to improve the motion estimation by using not only the conservation of the brightness, but also the conservation of its derivatives (Uras et al., 1988; Brox et al., 2004). However, local sinks or sources of brightness were still problematic, which might occur due to motion towards or away from the camera. Wildes et al. (1997) extended the optical flow method to deal with such situations by allowing divergent flows.

Other than object motion, fluid motion has the advantage that additional information exists that can be used to enhance the quality of the estimate. First and foremost, there are the partial differential equations (PDEs) that fluid flows satisfy, which allow to deduce certain properties that can be enforced during the motion estimation. Examples for local properties are given in Corpetti et al. (2002) and Corpetti et al. (2006), where the estimated velocity is biased towards a divergence-free and irrotational flow. However, a real strength of fluid flow estimation is the global description by its governing equations, which can be used to improve the motion estimation. Depending on the type of flow visualization, the PDEs of the physical flow can be remodeled to get PDEs for the projected two-dimensional flow in the images (Liu and Shen, 2008). Including PDEs

brings the advantage of a global motion model that rigidly connects all local estimates and gives physically sound results. The governing partial differential equations of turbulent flows are non-linear and therefore small changes of the initial state or boundary conditions can change the result globally. As a consequence, scientists tried to work with simpler global models like stream functions (Luttman et al., 2011, 2013) or a two-dimensional description of turbulent flows (Nakajima et al., 2003; Doshi and Bors, 2007), in order to exploit the benefit of physically-based, global motion models. The advantage of such methods is that they establish a connection between *Computational Fluid Dynamics* (CFD) and measurement data. The idea is to find a solution of the governing equations which also explains the motion in the measurement data.

In case of not too turbulent flows, the solution of the flow equations can be calculated if the boundary conditions are known. However, very often these are not known precisely enough, so assumptions have to be made. A way to overcome this problem is to use optimal control theory (Lions, 1971; Tröltzsch, 2009), which allows to introduce scalar or distributed parameters into the PDEs and compute them in such a way that a quantity of interest is optimal. With respect to image sequences, the possible quantity of interest can be the error between the recorded and the predicted image of a model.

The first appearance of optimal control in combination with image motion was presented by Borzì et al. (2002), who estimated the image motion as control variable in such a way that it was in accordance with the provided measurement data. Ruhnau (2006) published a variational optimal control approach, which determines the underlying motion from images that also satisfy some fluid dynamical PDE constraints. His work dealt with the estimation of the pressure and the velocity for two-dimensional synthetic data of a viscous non-turbulent flow (Ruhnau and Schnörr, 2006). An extension to turbulent flows was presented one year later, where he focused on the two-dimensional vorticity transport equation (Ruhnau et al., 2007). He proved in his work that variational optimal control methods are well suited to deal with fluid dynamical measurement data. Moreover, it has the advantage to estimate physical variables that are included in the constraints and are not measurable by other methods (e.g. pressure, body forces,...).

1.3 Contribution of this work

This thesis focuses on optimal control and parameter estimation methods for the estimation of motion from images using global motion models. These methods are applied to microflow applications and with special emphasis to *Molecular Tagging Velocimetry* (MTV) measurement data. The benefits and difficulties of the approaches are investigated and compared to standard estimation methods that include no global model. Of special interest is the accuracy with respect to the flow rate and the noise level, which was tested for a two-dimensional model. Such a parameter study is not available yet, since previous optimal control publications deal only with flow test cases to prove the concept. Another issue is the influence of the noise level, which has not been studied in detail so far.

In contrast to previous research that restricted their investigation to the estimation of two-dimensional flows, the given microfluidic images show integrated intensities of three-dimensional flows, which require of course three-dimensional modeling. The presented approach allows to estimate the fluid motion along with the molecular diffusion coefficient

of the tracer material. Especially in biology and medicine there is a keen interest in knowing diffusion coefficients of molecules in a solution.

The flexible optimal control framework RoDoBo (Becker et al., 2005) and PDE solver Gascoigne (Becker and Braack, 2005) were adapted to deal with image processing tasks and allowed optimal performance in terms of computational effort. Additional extensions of the framework allow a variable application in order to deal with arbitrary geometries of the fluid motion.

1.4 Outline of this thesis

This thesis is organized in such a way that the notation and necessary fundamental mathematics will be introduced in the second chapter. Special effort is given to the description of the efficient computation of optimization and optimal control problems. It includes a brief section about second-order partial differential equations, which are required to describe fluid motions. Furthermore, the *finite element method* (FEM) is presented as a technique to solve PDEs. The third chapter focuses on the estimation of motion from images in general. It clarifies the differences between real-world motion and image motion and presents the most prevailing methods to recover them. The main advantages and disadvantages of each technique will be pointed out and discussed. The fourth chapter deals with the specific application of these techniques to microfluidic images. The topic of microfluidics is introduced along with a set of applications and intrinsic problems that accompany it. Special measurement data of microfluidic devices are presented, which require a thorough modeling and adequate motion estimation method in order to give accurate results. Standard motion estimation methods are compared to optimal control and parameter estimation approaches that include the governing fluid motion equations. The accuracy of these approaches is investigated with respect to the flow rate and the level of noise. The final chapter contains the conclusions that can be drawn from the results, shown in the previous chapter and emphasizes the advantage of combining fluid simulations with measurement data in an optimal control framework. Finally, an outlook is given that points out the potential improvements and developments concerning this approach.

CHAPTER 2

Mathematical Preliminaries

2.1 Notation

Before proceeding with the concept of image motion it is necessary to introduce some mathematical definitions and notations that will be used in this thesis to describe methods and algorithms in the following chapters. Vector-valued functions of $\mathbb{R}^n$ are row vectors and are denoted with boldface variables and the components are labeled with numerical indices (e.g. $\boldsymbol{x} = (x_1, x_2, x_3)^T$). A row vector can be turned to a column vector by taking its transpose. The common notation is used for partial derivatives $\partial_x \boldsymbol{u} := \frac{\partial \boldsymbol{u}}{\partial x}$ and outer normal derivatives $\partial_{\boldsymbol{n}} \boldsymbol{u} := (\boldsymbol{n}^T \nabla)\boldsymbol{u}$. Derivatives with respect to functions are denoted by a prime symbol with the corresponding variable as subscript index (e.g. $j'_{\boldsymbol{u}}$). Furthermore, it is assumed that all variables are sufficiently smooth so that the derivatives exist. For the sake of readability the dependent variables (e.g. $\boldsymbol{x}$, t) are omitted whenever the formulation is self-explanatory. Photographic cameras provide area-integrated image intensities at discrete locations, the pixels. Consequently, the spatial domain Ω and the temporal domain T are discretized. In the following, all equations will be formulated using continuous spatial domains and discrete temporal domains. Nevertheless, all the conclusions and statements remain also valid for the actual discrete domains.

Definition An *image* I is defined as a square-integrable function that maps from a bounded coordinate domain Ω to an intensity domain $\mathcal{I}$. If there is also a temporal dependency $t \in T$, it is refer to it as *image sequence*.

$$\text{Image:} \qquad I \colon \Omega \to \mathcal{I} \tag{2.1}$$

$$\text{Image sequence:} \qquad I \colon \Omega \times T \to \mathcal{I} \tag{2.2}$$

In a most general sense, the domains Ω and T, $\mathcal{I}$ can be assumed to be compact subsets of $\mathbb{R}^2$ and $\mathbb{R}$, respectively. The temporal domain $\mathcal{T}$ is a set of N discrete time values $\{t_1, \dots t_N\}$. Any appropriate interpolation scheme can be used to extend the discrete domain to a continuous domain. In order to simplify the mathematical

expressions, the temporal variable is being omitted by using indices, $I_i(\boldsymbol{x}) \equiv I(\boldsymbol{x}, t_i)$, $\forall i = \{1 \dots N\}$. Since most algorithms use two images to determine motion, two consecutive images are usually denoted I_i and I_{i+1}, assuming $i + 1 \leq N$.

Definition An inner product of two variables $\boldsymbol{a}, \boldsymbol{b} : \mathcal{D} \to \mathbb{R}^m$ with $\mathcal{D} \subset \mathbb{R}^n$ is defined as

$$\langle \boldsymbol{a}, \boldsymbol{b} \rangle_{\mathcal{D}} := \int_{\mathcal{D}} \boldsymbol{a}^T(\boldsymbol{x}) \boldsymbol{b}(\boldsymbol{x}) \mathrm{d}\boldsymbol{x} \,, \tag{2.3}$$

which induces the standard Euclidean L^2-norm

$$\|\boldsymbol{a}\|_{\mathcal{D}} = \|\boldsymbol{a}\|_{L^2(\mathcal{D})} := \sqrt{\langle \boldsymbol{a}, \boldsymbol{a} \rangle_{\mathcal{D}}} \,. \tag{2.4}$$

If no domain is specified as index, the inner product and norm are with respect to the image domain Ω. In order to allow this notation also when $\boldsymbol{a}$ and $\boldsymbol{b}$ are matrices, they are reshaped as row vectors. Along with this norm, the maximum norm $\|\cdot\|_\infty = \|\cdot\|_{L^\infty(\mathcal{D})}$ and the L^1-norm $\|\cdot\|_{L^1(\mathcal{D})}$ will also be used.

Furthermore, it is necessary to define the displacement field $\boldsymbol{d} : \Omega \to \mathbb{R}^2$, which contains the information about the displacement of each pixel's intensity from one image to the next.

Definition The displacement function D acts on the spatial image domain by applying a coordinate transformation

$$D \colon \Omega \to \Omega \tag{2.5}$$

$$D \colon \boldsymbol{x} \mapsto \boldsymbol{x} + \boldsymbol{d}(\boldsymbol{x}) \,. \tag{2.6}$$

The displacement field $\boldsymbol{d}(\boldsymbol{x}) : \Omega \mapsto \mathbb{R}^2$ can easily be converted into a velocity field $\boldsymbol{u}$ if divided by the separation time δt between two images. It has to be noted that $\boldsymbol{x} + \boldsymbol{d}(\boldsymbol{x})$ does not necessarily have to be in Ω. In this case the function D returns the coordinate that is closest to it (Euclidean distance) and still in Ω. In order keep the notation condensed, a displacement operator $\hat{D}$ is introduced that acts on an image: $\hat{D}I := I \circ D$.

2.2 Optimization

Optimization is done in many scientific disciplines where a certain quantity needs to be the lowest or highest for a given situation. In economy it is usually monetary quantities that have to be optimal while for engineering purposes the fuel consumption of an engine or more general production processes have to be optimized. Physical optimization usually deals with the minimization of energy in order to determine the state of a system. In general, optimization describes the selection of the element $\boldsymbol{u}$ of a given set of elements $\mathcal{U}$ that is best with respect to some criterion. The criterion is an objective function J that maps each element of $\mathcal{U}$ onto a real number, $J : \mathcal{U} \to \mathbb{R}$. The best element $\boldsymbol{u}^* \in \mathcal{U}$ could either minimize or maximize J, depending on what is defined as optimal. Without

loss of generality it can be assumed to find the minimum of J because any maximization problem can be converted into a minimization problem by changing the sign of the objective function. The objective function for minimization problems is usually called cost function. Therefore, the problem can be formulated as

$$\boldsymbol{u}^* = \arg\min_{\boldsymbol{u}\in\mathcal{U}} J(\boldsymbol{u})\,. \tag{2.7}$$

This means that for any other element $\boldsymbol{u} \in \mathcal{U}\backslash\{u^*\}$ the objective functional is larger or just equal to $J(\boldsymbol{u}^*)$

$$J(\boldsymbol{u}^*) \leq J(\boldsymbol{u}), \qquad \forall \boldsymbol{u} \in \mathcal{U}\backslash\{u^*\} \tag{2.8}$$

The above definition includes discrete and continuous optimization. However, for many physical questions $\boldsymbol{u}$ is a function that is defined over some spatial and temporal domain. Therefore, in the following the focus will be on the continuous optimization.

2.3 Optimality conditions

Let $\mathcal{U} \subseteq L^2(\Omega)$ be the vector space of square-integrable functions over Ω, then the extreme value theorem guarantees the existence of a solution $\boldsymbol{u}^*$, if $J \in C^1(\Omega)$ is a continuous function and Ω is a compact domain in $\mathbb{R}^n$ (Heuser, 2009, §36.3). However, the uniqueness of the solution is not guaranteed in general. Most often it is unfeasible to find the global minimum within the entire solution space. Therefore, most algorithms try to find critical points by satisfying general properties of minima. For this purpose, a general definition of derivatives with respect to functions has to be introduced. The Gâteaux derivative is the generalization of a directional derivative in the context of differential calculus.

Definition Let X and Y be two normed vector spaces and $f : X \to Y$ be a mapping between them. Then the directional derivative of f at x in direction of δx is defined as

$$f'(x)(\delta x) = \lim_{\varepsilon\to 0} \frac{f(x+\varepsilon\delta x) - f(x)}{\varepsilon} = \left.\frac{\partial f(x+\varepsilon\delta x)}{\partial \varepsilon}\right|_{\varepsilon=0}, \tag{2.9}$$

if the limit exists for all $\delta x \in X$. If $f'(x)$ is a continuous linear mapping from X to Y, it is called Gâteaux derivative (Gateaux, 1919) and f is Gâteaux differentiable in x. Since f might be non-linear, the linear variables of f' are separated with additional parenthesis, here (δx). If f depends on a number of variables, the Gâteaux derivative with respect to one variable is indicated by a subscript of the variable, e.g. $f'_y(x, y)$ for the directional derivative with respect to the second variable y. For functions with just one dependent variable, the subscript is usually omitted. Higher-order derivatives are denoted in the same fashion, e.g. $f''_{xy}(x, y)$.

This definition can be used to formulate conditions that the critical point has to fulfill in order to be the optimal solution. Let J be Gâteaux differentiable at $\boldsymbol{u}^*$, then the minimizer satisfies the first-order necessary condition

$$J'(\boldsymbol{u}^*)(\boldsymbol{u}^* - \delta\boldsymbol{u}) = 0 \qquad \forall \delta\boldsymbol{u} \in \mathcal{U} \qquad \text{(first-order necessary condition)}\,, \tag{2.10}$$

which means that any small variation of the candidate solution $\boldsymbol{u}^*$ does not change the value of the cost functional J. In most cases this is not sufficient to tell whether the critical point satisfying (2.10) is the actual minimizer. The candidate solution could also be a maximizer or a saddle point. Wrong candidate solutions can be ruled out by testing the second-order sufficient condition

$$J''(\boldsymbol{u}^*)(\boldsymbol{u}^* - \delta\boldsymbol{u}, \boldsymbol{u}^* - \delta\boldsymbol{u}) \geq 0 \quad \forall \delta\boldsymbol{u} \in \mathcal{U} \qquad \text{(second-order sufficient condition)}\,. \tag{2.11}$$

If both conditions are satisfied at $\boldsymbol{u}^*$, the cost functional J has a at least a local minimum. For special cases the local minimum can coincide with the global minimum, e.g. if J is a convex function in $\boldsymbol{u}$.

2.3.1 Euler-Lagrange equation

If the cost functional can be formulated as an integral over a compact domain Ω of a twice continuously differentiable function $\mathcal{L}$ (see equation (2.12)), the first-order necessary condition can be expressed as a partial differential equation. Let Ω be a compact domain in $\mathbb{R}^n$ and $\mathcal{L}$ be an element of $C^2(\Omega)$ that depends on the spatial coordinate $\boldsymbol{x}$, a function $\boldsymbol{u}(\boldsymbol{x})$ and its spatial derivative $\boldsymbol{u}'(\boldsymbol{x})$.

$$J(\boldsymbol{u}) = \int_\Omega \mathcal{L}(\boldsymbol{x}, \boldsymbol{u}(\boldsymbol{x}), \boldsymbol{u}'(\boldsymbol{x}))dx \tag{2.12}$$

A function $\boldsymbol{u}$ has to be found that renders the cost functional J stationary. Furthermore, it is assumed that the solution $\boldsymbol{u}^*$ has prescribed boundary values at $\partial\Omega$. As a consequence any variation $\delta\boldsymbol{u}$ needs to vanish at $\partial\Omega$ so that the boundary values remain the same. Calculating the first-order necessary condition gives

$$\begin{aligned} 0 = J'(\boldsymbol{u}) &= J'_\varepsilon(\boldsymbol{u} + \varepsilon\delta\boldsymbol{u})\big|_{\varepsilon=0} \\ &= \int_\Omega \partial_\varepsilon \mathcal{L}(\boldsymbol{x}, \boldsymbol{u} + \varepsilon\delta\boldsymbol{u}, \boldsymbol{u}' + \varepsilon\delta\boldsymbol{u}')\big|_{\varepsilon=0} dx \\ &= \int_\Omega \left(\mathcal{L}'_{\boldsymbol{x}} \frac{\partial x}{\partial \varepsilon} + \mathcal{L}'_{\boldsymbol{u}} \frac{\partial(\boldsymbol{u} + \varepsilon\delta\boldsymbol{u})}{\partial\varepsilon}\Big|_{\varepsilon=0} + \mathcal{L}'_{\boldsymbol{u}'} \frac{\partial(\boldsymbol{u}' + \varepsilon\delta\boldsymbol{u}')}{\partial\varepsilon}\Big|_{\varepsilon=0} \right) dx \\ &= \int_\Omega \left(\mathcal{L}'_{\boldsymbol{u}} \delta\boldsymbol{u} + \mathcal{L}'_{\boldsymbol{u}'} \delta\boldsymbol{u}' \right) dx\,. \end{aligned} \tag{2.13}$$

The second term under the integral can be integrated by parts and leads to the expression

$$\begin{aligned} 0 &= \int_\Omega \left(\mathcal{L}'_{\boldsymbol{u}} \delta\boldsymbol{u} \right) dx + \mathcal{L}'_{\boldsymbol{u}'} \delta\boldsymbol{u}\Big|_{\partial\Omega} - \int_\Omega \left(\mathcal{L}''_{\boldsymbol{u}'\boldsymbol{x}} \delta\boldsymbol{u} \right) dx \\ &= \mathcal{L}'_{\boldsymbol{u}'} \delta\boldsymbol{u}\Big|_{\partial\Omega} + \int_\Omega \left(\mathcal{L}'_{\boldsymbol{u}} - \mathcal{L}''_{\boldsymbol{u}'\boldsymbol{x}} \right) \delta\boldsymbol{u} dx\,, \end{aligned} \tag{2.14}$$

where the first term is evaluated at the boundaries of Ω and vanishes due to $\delta\boldsymbol{u}\big|_{\partial\Omega} = 0$. The remaining integrand consists of the product of $\mathcal{L}'_{\boldsymbol{u}} - \mathcal{L}''_{\boldsymbol{u}'\boldsymbol{x}}$ with the variation $\delta\boldsymbol{u}$. The fundamental lemma of variational calculus (Byerly, 1917) states that if this equation holds for any variation that vanishes at $\partial\Omega$, than $\mathcal{L}'_{\boldsymbol{u}} - \mathcal{L}''_{\boldsymbol{u}'\boldsymbol{x}}$ must be identically zero within Ω. This leads to the *Euler-Lagrange* equation

$$0 = \mathcal{L}'_{\boldsymbol{u}} - \mathcal{L}''_{\boldsymbol{u}'\boldsymbol{x}}\,. \tag{2.15}$$

This equation is especially important for optimization tasks since it can be used to find stationary solutions. This concept is well-known and widely applied in physics, in particular in the field of classical mechanics.

2.4 Constrained optimization

For many optimization problems there are also restrictions on the solution. The sought solution has to fulfill certain constraints that can not be introduced directly into the cost functional. This can be due to non-linear constraints with no explicit representation or due to inequality constraints. The general constraint optimization problem can be written as

$$J(\boldsymbol{u}) \rightarrow min \qquad s.t. \qquad \begin{cases} a_i(\boldsymbol{u}) & = 0 \quad \text{(equality constraints)} \\ h_j(\boldsymbol{u}) & \leq 0 \quad \text{(inequality constraints)}\,, \end{cases} \tag{2.16}$$

where the indexes $1 \leq i \leq N$ and $1 \leq j \leq M$ indicate the individual constraints, N equality and M inequality constraints. Since inequality constraints will not play a role for this thesis, they are going to be omitted from this point on.

Constrained optimization problems can be converted into unconstrained optimization problems by using the Lagrangian function $\mathcal{L}$, which introduces additional variables for each constraint, the Lagrangian multipliers $\boldsymbol{z}$, which are also called adjoint variables or dual variables. The new unconstrained formulation of the problem reads

$$\mathcal{L}(\boldsymbol{u}, \boldsymbol{z}) = J(\boldsymbol{u}) - \boldsymbol{z}^T\boldsymbol{a}(\boldsymbol{u}) \tag{2.17}$$

where $\boldsymbol{z}^T\boldsymbol{a}$ can be viewed as an inner product and the equality constraints are bundled in the vector $\boldsymbol{a}$. The optimal solution $\boldsymbol{u}^*$ of the constraint problem in equation (2.16) coincides with the optimal solution $(\boldsymbol{u}^*, \boldsymbol{z}^*)$ of the unconstrained problem in equation (2.17). The solution for the unconstrained problem can be found by standard optimization algorithms, which search for stationary points that fulfill

$$\mathcal{L}'_{\boldsymbol{u}} = \boldsymbol{0} \tag{2.18}$$

$$\mathcal{L}'_{\boldsymbol{z}} = \boldsymbol{0}\,. \tag{2.19}$$

Of course, the second-order sufficient condition must be satisfied in order to test whether the solution is really a local minimizer.

2.5 Optimal control

Optimal control is an extension of the variational calculus, where a cost functional has to be minimized with respect to so-called state and control variables $\boldsymbol{u}$ and $\boldsymbol{q}$. The optimal control $\boldsymbol{q}^*$ is a function that minimizes a given cost functional J under certain constraints, usually partial differential equations that link the state and control variables. This mathematical field has gained a lot of interest since many processes in the world are governed by PDEs. One of the most prominent examples is the so-called *Brachistochrone* problem, where the trajectory has to be found, on which a body travels from one position to another position in the shortest time under a constant gravity force. There are many applications emerging from economical, technical and biological descriptions. The books of Lions (1971) and Tröltzsch (2009) give a detailed overview about optimal control under PDE constraints while the book of Gunzburger (2003) focuses on the application towards flow phenomena.

The general optimization formulation with equality constraints reads

$$\begin{aligned} & & J(\boldsymbol{u},\boldsymbol{q}) \rightarrow & \quad min \\ s.t. & & \boldsymbol{a}(\boldsymbol{u},\boldsymbol{q}) = & \quad \boldsymbol{0}\,. \end{aligned} \tag{2.20}$$

This problem resembles the unconstrained optimization with the difference, that the dependent variables are separated into state $\boldsymbol{u}$ and control $\boldsymbol{q}$ variables that are connected by a system of equality constraints $\boldsymbol{a}$. However, the procedure for solving the problem remains the same. The constrained formulation is converted into an unconstrained optimization problem by using the Lagrangian multiplier method

$$\mathcal{L}(\boldsymbol{u},\boldsymbol{q},\boldsymbol{z}) = J(\boldsymbol{u},\boldsymbol{q}) - \boldsymbol{z}^T\boldsymbol{a}(\boldsymbol{u},\boldsymbol{q}) \tag{2.21}$$

The optimum can be found by searching the solution $(\boldsymbol{u}^*,\boldsymbol{q}^*,\boldsymbol{z}^*)$ that renders J stationary. The first-order necessary condition reads

$$\nabla\mathcal{L} = 0\,, \tag{2.22}$$

where ∇ denotes the vector of Gâteaux derivatives with respect to $\boldsymbol{u}$, $\boldsymbol{q}$ and $\boldsymbol{z}$. The ensemble of these three equations is called the *optimality system*.

$$\text{optimality system} \quad \begin{cases} \mathcal{L}'_{\boldsymbol{z}} & = 0 & \rightarrow & \text{state equation} \\ \mathcal{L}'_{\boldsymbol{u}} & = 0 & \rightarrow & \text{adjoint equation} \\ \mathcal{L}'_{\boldsymbol{q}} & = 0 & \rightarrow & \text{optimality condition} \end{cases} . \tag{2.23}$$

State equation:

For an arbitrary variation $\delta\boldsymbol{z}$ of the adjoint state, the derivative can be written using the Gâteaux derivative.

$$
\begin{aligned}
0 &= \mathcal{L}'_{\boldsymbol{z}} \\
&= \lim_{\epsilon \to 0} \left(\frac{\mathcal{L}(\boldsymbol{u}, \boldsymbol{q}, \boldsymbol{z} + \epsilon\delta\boldsymbol{z}) - \mathcal{L}(\boldsymbol{u}, \boldsymbol{q}, \boldsymbol{z})}{\epsilon} \right) \\
&= \lim_{\epsilon \to 0} \left(\frac{J(\boldsymbol{u}, \boldsymbol{q}) - (\boldsymbol{z} + \epsilon\delta\boldsymbol{z})^T \boldsymbol{a}(\boldsymbol{u}, \boldsymbol{q}) - \left[J(\boldsymbol{u}, \boldsymbol{q}) - \boldsymbol{z}^T \boldsymbol{a}(\boldsymbol{u}, \boldsymbol{q}) \right]}{\epsilon} \right) \\
&= \lim_{\epsilon \to 0} \left(\frac{\epsilon\delta\boldsymbol{z}^T \boldsymbol{a}(\boldsymbol{u}, \boldsymbol{q})}{\epsilon} \right) \\
&= \delta\boldsymbol{z}^T \boldsymbol{a}(\boldsymbol{u}, \boldsymbol{q})
\end{aligned}
\tag{2.24}
$$

Since the equation has to be valid for any variation $\delta\boldsymbol{z}$, it follows that $\boldsymbol{a}(\boldsymbol{u}, \boldsymbol{q}) = 0$, which is the original constraint equation.

Adjoint equation:

The very same is done for an arbitrary variation $\delta\boldsymbol{u}$ of the state variable.

$$
\begin{aligned}
0 &= \mathcal{L}'_{\boldsymbol{u}} \\
&= \lim_{\epsilon \to 0} \left(\frac{\mathcal{L}(\boldsymbol{u} + \epsilon\delta\boldsymbol{u}, \boldsymbol{q}, \boldsymbol{z}) - \mathcal{L}(\boldsymbol{u}, \boldsymbol{q}, \boldsymbol{z})}{\epsilon} \right) \\
&= \lim_{\epsilon \to 0} \left(\frac{J(\boldsymbol{u} + \epsilon\delta\boldsymbol{u}, \boldsymbol{q}) - \boldsymbol{z}^T \boldsymbol{a}(\boldsymbol{u} + \epsilon\delta\boldsymbol{u}, \boldsymbol{q}) - \left[J(\boldsymbol{u}, \boldsymbol{q}) - \boldsymbol{z}^T \boldsymbol{a}(\boldsymbol{u}, \boldsymbol{q}) \right]}{\epsilon} \right)
\end{aligned}
\tag{2.25}
$$

Introducing the Taylor series in order to replace $J(\boldsymbol{u} + \epsilon\delta\boldsymbol{u}, \boldsymbol{q})$ yields

$$
J(\boldsymbol{u} + \epsilon\delta\boldsymbol{u}, \boldsymbol{q}) = J(\boldsymbol{u}, \boldsymbol{q}) + J'_{\boldsymbol{u}}(\boldsymbol{u}, \boldsymbol{q})(\epsilon\delta\boldsymbol{u}) + O(\epsilon^2)\,. \tag{2.26}
$$

Substituting this into the derivative equation gives

$$
\begin{aligned}
0 &= \lim_{\epsilon \to 0} \left(\frac{J(\boldsymbol{u},\boldsymbol{q}) + J'_{\boldsymbol{u}}(\boldsymbol{u},\boldsymbol{q})(\epsilon\delta\boldsymbol{u}) - \boldsymbol{z}^T [\boldsymbol{a}(\boldsymbol{u},\boldsymbol{q}) + \boldsymbol{a}'_{\boldsymbol{u}}(\boldsymbol{u},\boldsymbol{q})(\epsilon\delta\boldsymbol{u})] - \left[J(\boldsymbol{u},\boldsymbol{q}) - \boldsymbol{z}^T \boldsymbol{a}(\boldsymbol{u},\boldsymbol{q}) \right]}{\epsilon} \right) \\
&= \lim_{\epsilon \to 0} \left(\frac{J'_{\boldsymbol{u}}(\boldsymbol{u},\boldsymbol{q})(\epsilon\delta\boldsymbol{u}) - \boldsymbol{z}^T \boldsymbol{a}'_{\boldsymbol{u}}(\boldsymbol{u},\boldsymbol{q})(\epsilon\delta\boldsymbol{u})}{\epsilon} \right) \\
&= \left[J'_{\boldsymbol{u}}(\boldsymbol{u},\boldsymbol{q}) - \boldsymbol{z}^T \boldsymbol{a}'_{\boldsymbol{u}}(\boldsymbol{u},\boldsymbol{q}) \right] (\delta\boldsymbol{u}).
\end{aligned}
\tag{2.27}
$$

Since the variation $\delta\boldsymbol{u}$ is arbitrary, the term in the brackets has to be zero within the entire domain Ω. This yields the adjoint equation

$$
J'_{\boldsymbol{u}}(\boldsymbol{u}, \boldsymbol{q}) = \boldsymbol{z}^T \boldsymbol{a}'_{\boldsymbol{u}}(\boldsymbol{u}, \boldsymbol{q})\,. \tag{2.28}
$$

Optimality condition:

For an arbitrary variation of the control by $\delta\boldsymbol{q}$, the Gâteaux derivative reads

$$\begin{aligned} 0 &= \mathcal{L}'_{\boldsymbol{q}} \\ &= \lim_{\epsilon \to 0} \left(\frac{\mathcal{L}(\boldsymbol{u}, \boldsymbol{q} + \epsilon\delta\boldsymbol{q}, \boldsymbol{z}) - \mathcal{L}(\boldsymbol{u}, \boldsymbol{q}, \boldsymbol{z})}{\epsilon} \right) . \end{aligned} \tag{2.29}$$

After substitution of the first-order Taylor approximation of J and a the equation becomes

$$\begin{aligned} 0 &= \lim_{\epsilon \to 0} \left(\frac{J(\boldsymbol{u},\boldsymbol{q}) + J'_{\boldsymbol{q}}(\boldsymbol{u},\boldsymbol{q})(\epsilon\delta\boldsymbol{q}) - \boldsymbol{z}^T \left[\boldsymbol{a}(\boldsymbol{u},\boldsymbol{q}) + \boldsymbol{a}'_{\boldsymbol{q}}(\boldsymbol{u},\boldsymbol{q})(\epsilon\delta\boldsymbol{q}) \right] - \left[J(\boldsymbol{u},\boldsymbol{q}) - \boldsymbol{z}^T \boldsymbol{a}(\boldsymbol{u},\boldsymbol{q}) \right]}{\epsilon} \right) \\ &= \lim_{\epsilon \to 0} \left(\frac{J'_{\boldsymbol{q}}(\boldsymbol{u},\boldsymbol{q})(\epsilon\delta\boldsymbol{q}) - \boldsymbol{z}^T \boldsymbol{a}'_{\boldsymbol{q}}(\boldsymbol{u},\boldsymbol{q})(\epsilon\delta\boldsymbol{q})}{\epsilon} \right) \\ &= \left[J'_{\boldsymbol{q}}(\boldsymbol{u},\boldsymbol{q}) - \boldsymbol{z}^T \boldsymbol{a}'_{\boldsymbol{q}}(\boldsymbol{u},\boldsymbol{q}) \right] (\delta\boldsymbol{q}). \end{aligned} \tag{2.30}$$

Since the variation $\delta\boldsymbol{q}$ is arbitrary, the so-called optimality equation reads

$$J'_{\boldsymbol{q}}(\boldsymbol{u}, \boldsymbol{q}) = \boldsymbol{z}^T \boldsymbol{a}'_{\boldsymbol{q}}(\boldsymbol{u}, \boldsymbol{q}) \, . \tag{2.31}$$

Collecting all three first-order necessary equations leads to the optimality system of the following equations

$$\text{optimality system} \quad \left\{ \begin{array}{rcl} \boldsymbol{a}(\boldsymbol{u}, \boldsymbol{q}) & = & \boldsymbol{0} \\ J'_{\boldsymbol{u}}(\boldsymbol{u}, \boldsymbol{q}) & = & \boldsymbol{z}^T \boldsymbol{a}'_{\boldsymbol{u}}(\boldsymbol{u}, \boldsymbol{q}) \\ J'_{\boldsymbol{q}}(\boldsymbol{u}, \boldsymbol{q}) & = & \boldsymbol{z}^T \boldsymbol{a}'_{\boldsymbol{q}}(\boldsymbol{u}, \boldsymbol{q}) \end{array} \right. . \tag{2.32}$$

The above equations can be used to determine the optimal solution $(\boldsymbol{u}^*, \boldsymbol{q}^*, \boldsymbol{z}^*)$. Since this is just a necessary condition for the optimum, the second-order condition from equation (2.11) has to be fulfilled in order to be sufficient.

2.5.1 Reduced Lagrangian

Most optimization algorithms utilize the gradient to approach the optimum in an iterative manner, such as steepest descent, conjugate gradient or the Newton method (Wright and Nocedal, 1999). The previous section introduced the state and control variables explicitly. An alternative approach is the *reduced* Lagrangian j, where the state variable $\boldsymbol{u}$ is eliminated and treated implicitly. It is assumed that there is a solution operator S, which maps a given control parameter onto a unique state $\boldsymbol{u}$:

$$S(\boldsymbol{q}) = \boldsymbol{u} \, , \tag{2.33}$$

where $\boldsymbol{u}$ is a solution of the state equation. Putting this into the cost functional yields the reduced cost functional

$$j(\boldsymbol{q}) = J(S(\boldsymbol{q}), \boldsymbol{q})\,. \tag{2.34}$$

In order to find local minima, it is just necessary to calculate the derivatives with respect to the controls $\boldsymbol{q}$. Now, the reduced cost functional depends only on the control $\boldsymbol{q}$. The derivative of j with respect to the control is

$$\begin{aligned} j'(\boldsymbol{q})(\delta\boldsymbol{q}) &= J'_{\boldsymbol{u}}(\boldsymbol{u}, \boldsymbol{q})(\underbrace{S'(\boldsymbol{q})(\delta\boldsymbol{q})}_{\delta\boldsymbol{u}}) + J'_{\boldsymbol{q}}(\boldsymbol{u}, \boldsymbol{q})(\delta\boldsymbol{q}) \\ &= J'_{\boldsymbol{u}}(\boldsymbol{u}, \boldsymbol{q})(\delta\boldsymbol{u}) + J'_{\boldsymbol{q}}(\boldsymbol{u}, \boldsymbol{q})(\delta\boldsymbol{q}) \end{aligned} \tag{2.35}$$

The unknown term $\delta\boldsymbol{u}$ is the sensitivity and is related to the variation of the control variable via $\delta\boldsymbol{u} = S'(\boldsymbol{q})(\delta\boldsymbol{q})$. The linearized state equation can be used to calculate $\delta\boldsymbol{u}$ from $\delta\boldsymbol{q}$

$$\boldsymbol{a}'_{\boldsymbol{u}}(\boldsymbol{u}, \boldsymbol{q})(\delta\boldsymbol{u}) = \boldsymbol{a}'_{\boldsymbol{q}}(\boldsymbol{u}, \boldsymbol{q})(\delta\boldsymbol{q}) \tag{2.36}$$

The resulting $\delta\boldsymbol{u}$ can be put together with $\delta\boldsymbol{q}$ into equation (2.35) to calculate the gradient of j. However, this procedure gets easily unfeasible, if the control is a distributed variable because after discretization of Ω, the equation (2.36) has to be solved for each basis function of Ω.

A way to circumvent this problem is to calculate the derivative via the adjoint approach (Meidner, 2008; Duffy, 2009; Tröltzsch, 2009). Using the solution operator S, the Lagrangian from equation (2.17) has to be equal to the reduced cost functional j for all possible choices of the adjoint state $\boldsymbol{z}$.

$$j(\boldsymbol{q}) = J(S(\boldsymbol{q}), \boldsymbol{q}) = \mathcal{L}(S(\boldsymbol{q}), \boldsymbol{q}, \boldsymbol{z}) \qquad , \forall \boldsymbol{z} \in \mathcal{U} \tag{2.37}$$

As a consequence the gradient $j'(\boldsymbol{q})(\delta\boldsymbol{q})$ can also be calculated by using derivatives of the Lagrangian

$$j'(\boldsymbol{q})(\delta\boldsymbol{q}) = \mathcal{L}'_{\boldsymbol{u}}(\boldsymbol{u}, \boldsymbol{q}, \boldsymbol{z})(\delta\boldsymbol{u}) + \mathcal{L}'_{\boldsymbol{q}}(\boldsymbol{u}, \boldsymbol{q}, \boldsymbol{z})(\delta\boldsymbol{q})\,. \tag{2.38}$$

The advantage is, that this equation holds for any arbitrary $\boldsymbol{z}$ if $\boldsymbol{u} = S(\boldsymbol{q})$. Therefore, the adjoint state $\boldsymbol{z}$ can be chosen in such a way that the first term

$$\mathcal{L}'_{\boldsymbol{u}}(\boldsymbol{u}, \boldsymbol{q}, \boldsymbol{z})(\delta\boldsymbol{u}) = 0 \tag{2.39}$$

for any variation $\delta\boldsymbol{u}$. This simplifies the equation for the gradient to

$$\begin{aligned} j'(\boldsymbol{q})(\delta\boldsymbol{q}) &= \mathcal{L}'_{\boldsymbol{q}}(\boldsymbol{u}, \boldsymbol{q}, \boldsymbol{z})(\delta\boldsymbol{q}) \\ &= J'_{\boldsymbol{q}}(\boldsymbol{u}, \boldsymbol{q})(\delta\boldsymbol{q}) - \boldsymbol{z}^T \boldsymbol{a}'_{\boldsymbol{q}}(\boldsymbol{u}, \boldsymbol{q})(\delta\boldsymbol{q})\,. \end{aligned} \tag{2.40}$$

Determining the gradient via the adjoint approach involves the computation of the adjoint state $\boldsymbol{z}$ via equation (2.39), inserting it into equation (2.40) and computing $j'(\boldsymbol{q})$ for the given direction $\delta\boldsymbol{q}$. The computation via the adjoint method is independent from the discretization of Ω. Unlike the sensitivity approach, the gradient can be calculated all at once because the adjoint equation does not depend on $\delta\boldsymbol{q}$.

Similar to the calculation of the first-order derivative, the second-order derivative can be computed easier by choosing appropriate adjoint states and solving corresponding auxiliary problems. At this point, the interested reader is referred to Meidner (2008) for a rigorous and lengthy derivation of the second derivative. The second derivative for the two directions $\delta\boldsymbol{q}$ and $\tau\boldsymbol{q}$ reads

$$\begin{aligned} j''(\boldsymbol{q})(\delta\boldsymbol{q},\tau\boldsymbol{q}) =& J''_{\boldsymbol{qq}}(\boldsymbol{u},\boldsymbol{q})(\delta\boldsymbol{q},\tau\boldsymbol{q}) + J''_{\boldsymbol{uq}}(\boldsymbol{u},\boldsymbol{q})(\delta\boldsymbol{u},\tau\boldsymbol{q}) + J''_{\boldsymbol{qq}}(\boldsymbol{u},\boldsymbol{q})(\delta\boldsymbol{q},\tau\boldsymbol{q}) \\ & - \delta\boldsymbol{z}^T\boldsymbol{a}'_{\boldsymbol{q}}(\boldsymbol{u},\boldsymbol{q})(\tau\boldsymbol{q}) - \boldsymbol{z}^T\boldsymbol{a}''_{\boldsymbol{uq}}(\boldsymbol{u},\boldsymbol{q})(\delta\boldsymbol{u},\tau\boldsymbol{q}) - \boldsymbol{z}^T\boldsymbol{a}''_{\boldsymbol{qq}}(\boldsymbol{u},\boldsymbol{q})(\delta\boldsymbol{q},\tau\boldsymbol{q}) \end{aligned} \tag{2.41}$$

and involves the computation of axillary equations.

Having the first- and second-order derivatives with respect to the control $\boldsymbol{q}$ allows to use the efficient iterative Newton method to compute the optimal solution $(\boldsymbol{u}^*,\boldsymbol{q}^*,\boldsymbol{z}^*)$. Using this method the solution can be computed by

$$\boldsymbol{q}^{(i+1)} = \boldsymbol{q}^{(i)} - \left[j''(\boldsymbol{q}^{(i)})(\delta\boldsymbol{q},\tau\boldsymbol{q})\right]^{-1} j'(\boldsymbol{q}^{(i)})(\delta\boldsymbol{q}) \qquad \forall\delta\boldsymbol{q},\tau\boldsymbol{q}\,, \tag{2.42}$$

where i indicates the iteration. For many problems the hessian is too large to be inverted or to calculate the matrix vector product. Therefore, one often tries to compute the update $\boldsymbol{q}^{(i+1)} - \boldsymbol{q}^{(i)}$ between two iterations rather than the actual variables. The advantage lies in the fact that for the update, the hessian does not need to be inverted. The update is computed by solving

$$j'(\boldsymbol{q}^{(i)})(\delta\boldsymbol{q}) = j''(\boldsymbol{q}^{(i)})(\delta\boldsymbol{q},\tau\boldsymbol{q}) \cdot (\boldsymbol{q}^{(i+1)} - \boldsymbol{q}^{(i)}) \qquad \forall\delta\boldsymbol{q},\tau\boldsymbol{q}\,, \tag{2.43}$$

which can be done with a conjugate gradient method (CG) because the hessian is a positive semi-definite matrix. The presented optimal control method is implemented in the C++ framework RoDoBo[1] (Becker et al., 2005) and combined with the finite element solver Gascoigne (Becker and Braack, 2005) in order to allow solving PDE constrained problems.

2.6 Boundary value problems

For many processes in nature, the dynamics of the system depend not only on the magnitude of some variables but also on their derivatives with respect to time and space. This dependency can be formulated as a partial differential equation of the form

$$F(\boldsymbol{x},\boldsymbol{u}(\boldsymbol{x}),\boldsymbol{u}'_{\boldsymbol{x}}(\boldsymbol{x}),\boldsymbol{u}''_{\boldsymbol{xx}}(\boldsymbol{x}),\dots) = \boldsymbol{0}\,, \tag{2.44}$$

[1] http://www.rodobo.org

where $\boldsymbol{x} \in \Omega$ and $\boldsymbol{u} : \Omega \to \mathbb{R}^n$ and F is a function mapping to $\mathbb{R}^n$. If F is a linear function in all its variables then the PDE is called linear. Special interest of this thesis lies upon linear second-order PDEs. For this purpose we introduce the differential operator $\hat{L}$ to formulate the general second-order PDE

$$\hat{L}\boldsymbol{u} = \sum_n a_{ij}\partial_i\partial_j\boldsymbol{u} + \sum_n a_i\partial_i\boldsymbol{u} + a\boldsymbol{u} = f\,. \tag{2.45}$$

The functions a, a_i, a_{ij} are coefficient functions for the $\boldsymbol{u}$ associated variables and f is the right-hand-side. Without loss of generality it can be assumed that $a_{ij} = a_{ji}$. Linear second-order PDEs can be categorized into three types: *elliptic*, *parabolic* and *hyperbolic*. Similar to cone sections, a determinant criterion is used to classify them into the categories, which depends just on the coefficient functions. Since this thesis deals just with elliptic boundary value problems, the other two categories will not be treated in this context. A thorough description can be found in many graduate mathematical textbooks dealing with PDEs or numerical mathematics, e.g. Tveito and Winther (2005), Evans (1998), Wright and Nocedal (1999). In the normal form an elliptic operator $\hat{L}$ does not contain mixed second-order derivatives but just the Laplacian Δ and lower-order derivatives. The prototypical example is the *Poisson* equation.

$$\Delta\boldsymbol{u} = \boldsymbol{f} \tag{2.46}$$

In combination with some boundary conditions on $\partial\Omega$ the problem is called *boundary value problem*. The general boundary condition can be formulated as

$$\alpha\boldsymbol{u} + \beta\frac{\partial\boldsymbol{u}}{\partial\boldsymbol{n}} = \boldsymbol{g} \qquad \text{on } \partial\Omega\,, \tag{2.47}$$

where α and β are coefficients. If the constant β is zero, the boundary condition is of *Dirichlet*-type. Alternatively, if α is zero it is called *Neumann*-type. A mixed combination is referred to as *Robin* boundary condition.

2.6.1 Weak solutions

Focusing on the *Dirichlet*-type boundary value problems, it has to be mentioned that the existence of a *classical solution* is hardly ever given. A classical solution $\boldsymbol{u}$ for a second-order PDE is a function that is at least twice continuously differentiable in Ω, continuous up to the border $\partial\Omega$ and satisfies the boundary conditions. In cases of discontinuous boundary data $\boldsymbol{g}$ or non-smooth domains Ω, there might not exist a *classical solution*. However, it is possible to find so-called *weak* solutions that do not satisfy the original boundary value problem but the corresponding variational problem. The benefit lies in the larger solution space that requires less regularity on the solution. The variational formulation of the *Poisson* equation (2.46) can be derived by applying the *fundamental lemma of variational calculus* that introduces test functions ϕ so

$$\int_\Omega (\Delta\boldsymbol{u} + \boldsymbol{f})\,\phi = 0 \tag{2.48}$$

is valid for any appropriate choice of ϕ. Certainly, if $\boldsymbol{u}$ is a *classical solution*, the equation holds true for any ϕ if the integral is well defined. Suppose the test functions are sufficiently smooth, the smoothness of the solution $\boldsymbol{u}$ can be reduced by applying the product rule of derivation

$$\int_\Omega \phi \nabla^2 \boldsymbol{u} = -\int_\Omega \nabla \boldsymbol{u} \cdot \nabla \phi + \int_\Omega \nabla \cdot (\phi \nabla \boldsymbol{u}) \,. \tag{2.49}$$

It is assumed that the border $\partial\Omega$ can be separated into a distinctive Dirichlet boundary $\partial\Omega_D$ and Neumann boundary $\partial\Omega_N$ with $\boldsymbol{u} = \boldsymbol{g}$ on $\partial\Omega_D$ and $\partial_n \boldsymbol{u} = \boldsymbol{g}$ on $\partial\Omega_N$, respectively. For the *Dirichlet* boundary condition, the last integral cancels out because ϕ has to be identical zero at $\partial\Omega_D$. For *Neumann* boundary conditions, the integral can be rewritten with the divergence theorem and the boundary condition from equation (2.47) to

$$\begin{aligned} \int_\Omega \phi \nabla^2 \boldsymbol{u} &= -\int_\Omega \nabla \boldsymbol{u} \cdot \nabla \phi + \int_{\partial\Omega_N} \phi \frac{\partial \boldsymbol{u}}{\partial \boldsymbol{n}} \\ &= -\int_\Omega \nabla \boldsymbol{u} \cdot \nabla \phi + \int_{\partial\Omega_N} \phi \boldsymbol{g} \end{aligned} \tag{2.50}$$

The solution $\boldsymbol{u}$ and the test function ϕ need to have certain properties in order to have well defined integrals. Their gradients have to be square-integrable in Ω. This leads to the definition of the *Sobolev* vector spaces

$$H^1(\Omega) := \left\{ \boldsymbol{u} : \Omega \to \mathbb{R}^n \,\middle|\, \boldsymbol{u}, \partial_i \boldsymbol{u} \in L^2(\Omega) \,,\ \forall i = 1 \dots n \right\} , \tag{2.51}$$

$$H_0^1(\Omega, \Gamma) := \left\{ \phi \in H^1(\Omega) \,\middle|\, \phi\big|_\Gamma = 0 \right\} , \tag{2.52}$$

$$H_g^1(\Omega, \Gamma) := \left\{ \phi \in H^1(\Omega) \,\middle|\, \phi\big|_\Gamma = \boldsymbol{g} \right\} . \tag{2.53}$$

A *weak* solution $\boldsymbol{u} \in \mathrm{H}_g^1(\Omega, \partial\Omega_D)$ that satisfies the Poisson equation (2.46) with Dirichlet boundaries $\boldsymbol{u}\big|_{\partial\Omega_D} = \boldsymbol{g}$ and Neumann boundary $\partial_n \boldsymbol{u}\big|_{\partial\Omega_N} = \boldsymbol{g}$ satisfies also its variational formulation

$$\int_\Omega \nabla \boldsymbol{u} \cdot \nabla \phi = \int_\Omega \boldsymbol{f} \phi + \int_{\partial\Omega_N} \phi \boldsymbol{g} \qquad \forall \phi \in H_0^1(\Omega, \partial\Omega_D) \,. \tag{2.54}$$

The variational formulation can be written rather shortly by using the following notations:

$$(\boldsymbol{u}, \boldsymbol{v}) = \int_\Omega \boldsymbol{u}(\boldsymbol{x}) \boldsymbol{v}(\boldsymbol{x}) \mathrm{d}\boldsymbol{x}, \qquad (\boldsymbol{u}, \boldsymbol{v})_V = \int_V \boldsymbol{u}(\boldsymbol{x}) \boldsymbol{v}(\boldsymbol{x}) \mathrm{d}\boldsymbol{x} \,. \tag{2.55}$$

In the condensed notation the variational Poisson problem reads

$$(\nabla \boldsymbol{u}, \nabla \phi) = (\boldsymbol{f}, \phi) + (\boldsymbol{g}, \phi)_{\partial\Omega_N} \qquad \forall \phi \in H_0^1(\Omega, \partial\Omega_D) \,. \tag{2.56}$$

It can be proved that if there is a *classical solution* of an elliptical second-order boundary value problem, it is equal to the *weak* solution of the variational formulation (Braess, 2007, p. 35). Also, the *Lax-Milgram Theorem* can be used to show that there always exists a *weak* solution to elliptic boundary value problems and that it is unique (Evans, 1998, chap. 6.2).

2.7 Finite element method

The finite elements method (FEM) is a numerical technique for solving partial differential equations. Instead of finding a solution in $H_0^1(\Omega, \partial\Omega)$ to the linear problem in equation (2.56), the solution space is replaced by a suitable finite dimensional vector space S_h. The parameter h characterized the discretization and for $h \to 0$ the solution in S_h converges to the solution of the continuous problem. Let $\{e_1, \dots e_N\}$ be the basis for S_h, then the weak formulation of Poisson equation with zero Dirichlet boundaries is equivalent to

$$(\nabla \boldsymbol{u}, \nabla e_i) = (\boldsymbol{f}, e_i) \qquad \forall i \in \{1, \dots N\}\,, \tag{2.57}$$

because the test functions ϕ can be composed by a linear combination of the basis functions. The solution $\boldsymbol{u}$ and $\boldsymbol{f}$ can be also represented in this basis by

$$\boldsymbol{u} = \sum_{j=1}^{N} a_j e_j \qquad \text{and} \qquad \boldsymbol{f} = \sum_{j=1}^{N} b_j e_j\,, \tag{2.58}$$

which in combination with the previous equation leads to the linear system

$$\sum_{j=1}^{N} \underbrace{(\nabla e_j, \nabla e_i)}_{M_{ij}} a_j = \sum_{j=1}^{N} \underbrace{(e_j, e_i)}_{G_{ij}} b_j \qquad , \forall i \in \{1, \dots N\}\,. \tag{2.59}$$

The entire system of equations can be written as a vector matrix product of the form

$$\boldsymbol{M}\boldsymbol{a} = \boldsymbol{G}\boldsymbol{b}\,, \tag{2.60}$$

where $\boldsymbol{M}$ is referred to as *stiffness matrix* and $\boldsymbol{G}$ is called the *mass matrix*. If the basis functions are chosen in such a way that they have a small local support, then the matrices are very sparse and there are efficient numerical techniques to solve them.

The set of basis functions is intrinsically connected to the discretization of the domain. The domain Ω is divided in tiles $\{T_1, T_2, \dots\}$ of finite size, the so-called elements. In two dimensions the tiles have usually triangular or quadrilateral shape. For each tile the solution is approximated by a continuous polynomial function between its nodes. The FEM-computations of this thesis use linear quadrilateral FEs, which are commonly denoted as Q_1 elements. Figure 2.1 shows a basis function of such a discretization in two dimensions, which is has a support that covers four Q_1 elements in total. For

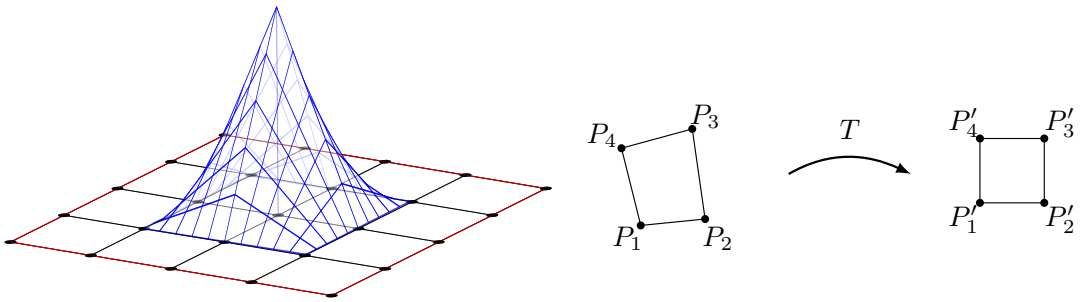

Figure 2.1: The left illustration shows a basis function of a linear quadrilateral discretization (Q_1-FE). The right sketch shows how one FE is mapped onto a rectangular reference FE in order to allow an easy numerical integration.

convenience the tiles in this figure are of rectangular shape, this is not necessarily the case. In order to calculate the inner products of pairwise basis functions, they have to be multiplied and integrated. It is convenient to transform each quadrilateral to a rectangular reference element (see figure 2.1 right) in order to enable easy integration by *Gaussian quadrature*. A comprehensive description of the finite element method can be found in many graduate textbooks, such as the books from Braess (2007), Elman et al. (2005) or Gockenbach (2006).

The partial differential equations of fluid dynamics have the special property that they belong to the *saddle point* problems. The pressure p can be seen as a Lagrangian multiplier that imposes the incompressibility (Strang, 2007). This causes numerical instabilities that might lead to a singular system of equations, especially if ∇p becomes zero for $p \neq 0$. To ensure that this is not the case the *inf-sup* condition or Ladyzhenskaya-Babuška-Breezi condition has to be satisfied. It states that for every p there has to be a velocity $\boldsymbol{u}$ such that

$$\boldsymbol{u}^T \nabla p \geq \beta \sqrt{\boldsymbol{u}^T \Delta^{-1} \boldsymbol{u}} \sqrt{p^T p} \qquad \text{for a fixed } \beta > 0\,, \tag{2.61}$$

where Δ^{-1} is the inverse operator of the Laplacian. A workaround to satisfy this condition is to use different finite elements for $\boldsymbol{u}$ and p. The so-call *Taylor-Hood* discretization uses a lower-order FE for p than for $\boldsymbol{u}$, e.g. Q_1 for pressure and Q_2 for velocity. However, mixed finite elements are inconvenient in terms of their computational design. Alternatively, stabilization methods can be used to allow equal order elements for $\boldsymbol{u}$ and p that also allow easier implementations of robust solvers. The computations of this thesis take advantage of the *local projection stabilization* (LPS) Becker and Braack (2001) in order to use Q_1-FEs for pressure and velocity. The interested reader is referred to the book of Girault and Raviart (1986) for further information about finite elements in combination with Navier-Stokes equations.

CHAPTER 3

Motion Estimation

There is an important difference between the real world motion and the optical motion. Real world motion describes the actual motion of a moving object, while image motion describes the motion after being projected onto a plane. The projection can be modeled by the so-called plenoptic function (Adelson and Bergen, 1991), and the image motion from its derivative with respect to time (Longuet-Higgins and Prazdny, 1980). Purely translational motion can appear entirely different on the images because of the perspective projection of most cameras. Figure 3.1 shows the three types of optical motion fields that originate from purely translational motion of the object with respect to the camera. If the object moves orthogonal to the line of sight, the optical motion is just scaled by the magnification factor of the lens. However, if the distance between an object and the camera changes, its projected image grows or shrinks due to the perspective projection. The corresponding optical motion fields are shown in the middle and the right of figure 3.1.

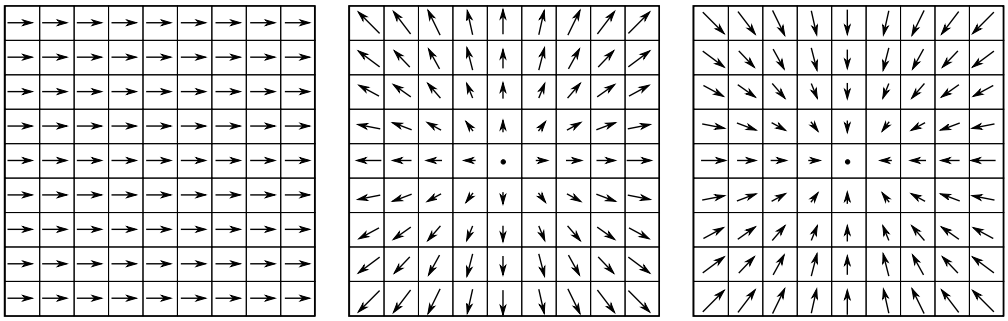

Figure 3.1: These three optical motion fields originate from a purely translational motion of the object with respect to the camera after being projected.

These three optical motions stem from completely translational motion of a rigid object. However, for non-rigid objects, like fluids, one can not distinguish anymore between optical flow that originates from motion towards the camera or because the its size changed. In order to deduce the actual motion form images, special care

has to be taken during the recording of the images. There are several methods to overcome this problem. Either one tries to record only the motion within a distinct plane (e.g. illumination sheet), uses multiple projections (e.g. tomographic reconstruction) or telecentric lenses.

3.1 Fundamentals of image motion

In order to determine motion from a sequence of images, it is necessary that consecutive images are not independent. This inherent relationship can be formulated statistically in such a way that for every pixel the joint probability of consecutive images does not factorize, they are not independent:

$$\mathrm{pdf}(\boldsymbol{x}, I_i, I_{i+1}) \neq \mathrm{pdf}(\boldsymbol{x}, I_i)\,\mathrm{pdf}(\boldsymbol{x}, I_{i+1})\,. \tag{3.1}$$

Consequently, there has to be a functional relationship that accounts for this dependency and that converts one image into the other.

It is assumed that this relationship can be described by a function f that transforms the first image into the second image. Because of random processes like camera noise, the mapping is corrupted by noise:

$$I_{i+1} = \mathrm{func}(I_i) + noise\,. \tag{3.2}$$

Apart from the noise, the function func$(\cdot)$ incorporates all processes that lead to the evolution from I_i to I_{i+1}. This includes especially motion but also all systematic phenomena that have an effect on the brightness. Such effects could be a changing illumination, occluding objects in the image or any change of physical properties that can be pictured by the camera. In the simplest case, it is assumed that all changes are due to the dislocation of pixel intensities from one image to the consecutive image. This means that func$(\cdot)$ is fully described by knowing the displacement function $\boldsymbol{d}_i$. The modeled dependency for this case can be written in the form

$$I_{i+1}(\boldsymbol{x}) = I_i(\boldsymbol{x} + \boldsymbol{d}_i) + noise\,. \tag{3.3}$$

The retrieval of the motion field $\boldsymbol{d}_i$ from the two images I_i and I_{i+1} is an inverse problem, which is not well-posed in the sense of Hadamard (1902). This means that not all of the following requirements are fulfilled:

1. a solution exists,
2. the solution is unique,
3. slightly changed data does not affect the solution very much.

The equation (3.3) is underdetermined since there are two unknowns for every pixel of the image. This can be easily demonstrated by the simple example in figure 3.2, where the motion can not be uniquely determined because there are two possible solutions.

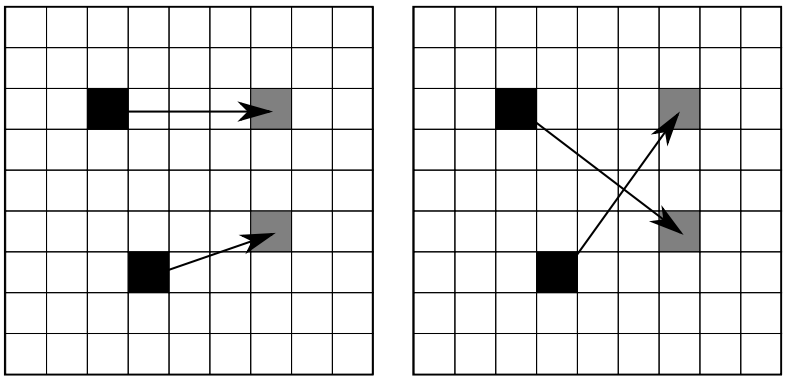

Figure 3.2: Illustration of the ill-posedness of the motion retrieval from equation (3.3). The ■ indicates pixels with non-zero intensity in the first image and ■ in the second image, respectively. The motion is not uniquely determined so that each pixel value could move to one or the other pixel position in the second image.

In order to find a solution, it is necessary to define a cost functional which measures the similarity of two images. A common measure is the *sum of squared differences* (SSD)

$$\mathrm{SSD} = \int_{\Omega} (I_{i+1}(\boldsymbol{x}) - I_i(\boldsymbol{x} + \boldsymbol{d}_i))^2 \mathrm{d}\boldsymbol{x}\,. \tag{3.4}$$

The displacement $\boldsymbol{d}_i$ is a parameter that has to be chosen in such a way that the SSD becomes as small as possible. The problem can be formulated as finding the optimal solution $\boldsymbol{d}_i^*$ that yields the smallest possible value for the SSD:

$$\boldsymbol{d}_i^* = \arg\min_{d_i} \int_{\Omega} (I_{i+1}(\boldsymbol{x}) - I_i(\boldsymbol{x} + \boldsymbol{d}_i))^2 \mathrm{d}\boldsymbol{x}\,. \tag{3.5}$$

This equation is ill-posed like the equation (3.3). Additional information has to be included in order to render the problem well-posed. There are several ways to do this. One possibility is to reduce the number of velocity estimates to less than one estimate per pixel. This decreases the number of unknowns and leaves more information for the remaining pixels. Another possibility is the *Tikhonov*-regularization (Tikhonov and Arsenin, 1977), which imposes certain properties on the solution. A reasonable assumption is the smoothness of the solution, since adjacent pixels are most likely to have similar motion estimates. The two possibilities are going to be addressed in the following paragraphs.

3.2 Image motion estimation techniques

Among all motion estimation approaches, this thesis explains the most prominent ones, that have been also applied to fluid flow images. Therefore, correlation and gradient methods are briefly introduced, while frequency or feature methods are omitted. A comprehensive review about possible motion estimation techniques can be found in Beauchemin and Barron (1995), Derpanis (2006) or in the book of Jähne (2006).

3.2.1 Correlation based

As indicated previously, the amount of data does not suffice to estimate uniquely a dense motion field. A way to overcome this deficiency is to divide the image domain Ω in smaller subdomains Ω_j, so-called interrogation windows (IW) and to estimate for each IW just one motion estimate. For reasons of convenience, the partitioning is usually done into rectangular shapes.

$$\boldsymbol{d}_i|_{\Omega_j} = \arg\min_{d_i} \int_{\Omega_j} (I_{i+1}(\boldsymbol{x}) - I_i(\boldsymbol{x}+\boldsymbol{d}_i))^2 \mathrm{d}\boldsymbol{x} \tag{3.6}$$

Expanding the squared parenthesis gives three terms, of which $\int_{\Omega_j} \mathrm{I}_{i+1}^2 \mathrm{d}\boldsymbol{x}$ is a constant and $\int_{\Omega_j} I_i^2(\boldsymbol{x}+\boldsymbol{d}_i)\mathrm{d}\boldsymbol{x}$ is assumed to be constant. This means that independent of the position of the IW, the total intensity of the pixels remains the same or more specifically $\partial/\partial d_i \|I_i(\boldsymbol{x}+\boldsymbol{d}_i)\|_{\Omega_j} = 0$. This assumption holds if the in- and outflow of intensity over the borders of Ω_j cancels out. This constraint relaxes for large interrogation windows Ω_j because the net gain of intensity is usually negligible in comparison to the intensity that remains in the domain. Since constants do not effect the minimization, they are discarded and the only leftover term can be written as scalar product $-2\langle I_{i+1}, I_i \circ D_i\rangle_{\Omega_j}$. The Cauchy-Schwarz-inequality states that for inner product spaces the relation $\langle \boldsymbol{a}, \boldsymbol{b}\rangle_{\mathcal{D}} \leq \|\boldsymbol{a}\|_{\mathcal{D}} \cdot \|\boldsymbol{b}\|_{\mathcal{D}}$ holds for all $\boldsymbol{a}, \boldsymbol{b} \in \mathcal{D}$. Therefore, it can be normalized by the appropriate image norms, which were argued to be constant previously. The factor in front of the inner product can be neglected and the minimization is turned into a maximization by changing the sign, which gives the formula for the normalized correlation

$$\boldsymbol{d}_i|_{\Omega_j} = \arg\max_{\boldsymbol{d}_i} \frac{\langle I_{i+1}, I_i \circ D_i\rangle_{\Omega_j}}{\|I_{i+1}\|_{\Omega_j}\|I_i \circ D_i\|_{\Omega_j}}\,. \tag{3.7}$$

Just a single motion estimate has to be found for the entire subdomain Ω_j, which maximizes the correlation value. Figure 3.3 shows patches of two consecutive images depicting a flow, which is seeded with particles. The pattern of the particles remains almost constant and is translated to the right. The same figure shows also the corresponding correlation function. It has a sharp peak at the displacement, which leads to the best overlap of both image patterns. The maximal value is about 0.9, which means that the pattern is not just translated but also slightly changed. The constant level of correlation (about 0.55) stems from the fact that images have usually just positive intensity values. Subtracting the mean over Ω_j corrects for this effect, so that also negative correlations are possible.

In a more general manner the correlation window can be defined as a weighting function $w : \Omega \mapsto \mathbb{R}^+$, which is centered around the position of the estimate

$$\boldsymbol{d}_i = \arg\max_{\boldsymbol{d}_i} \frac{\langle wI_{i+1}, wI_i \circ D_i\rangle}{\|wI_{i+1}\|\|wI_i \circ D_i\|}\,. \tag{3.8}$$

The correlation technique is most frequently used in fluid engineering in order to determine motion. This has historical reasons. Before the advent of digital images, *laser*

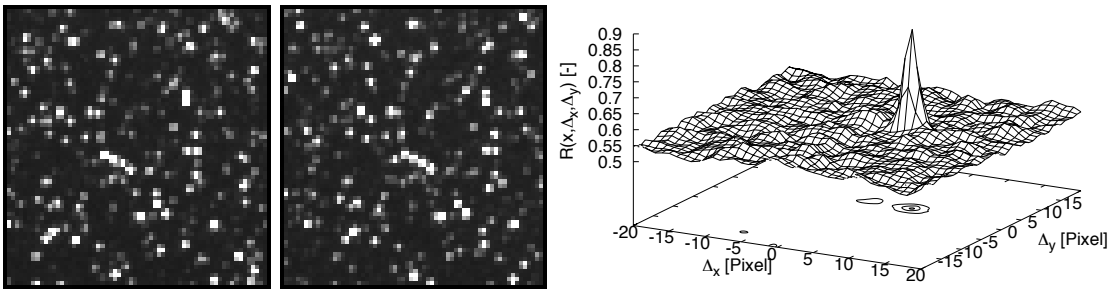

Figure 3.3: Two images of a flow that is visualized with particles. The function on the right is the corresponding cross-correlation according to equation (3.7)

speckle velocimetry and *Young's fringe method* were used to estimate motion (Keane and Adrian, 1990). These techniques used interference patterns to deduce the direction and magnitude of the motion by optical correlations.

The idea of correlation was transferred to digital images and in the fluid dynamics community this approach became known as *particle image velocimetry* (PIV) (Adrian, 1991, 2005; Raffel et al., 2007; Willert and Gharib, 1991). PIV uses particles to visualize the motion of a fluid flow. The particles are illuminated with a thin laser sheet ($< 1\,\mathrm{mm}$) and photographed by a recording system. This way the visualized motion lies within a known plan and is not superimposed by other motions or integrated over the line-of-sight.

3.2.1.1 Hierarchical approach

One drawback of these methods lies in the reduced spatial resolution, since the estimate belongs to the entire subdomain Ω_j. As a consequence it is not possible to resolve motions that are smaller than the interrogation window. Astarita (2006) showed that the resolution can be increased by knowing the modulation transfer function and applying an overlap between the subdomains $\Omega_j \bigcap \Omega_k \neq \emptyset$. A general method to increase the resolution is to decrease the size of the correlation window. However, if the correlation window is to small, there might be an insufficient amount of data left to determine reliable motion estimates. With respect to PIV, Keane and Adrian (1992) found a minimum of 4 corresponding particles should be in both images to allow a detection probability of 90%. A very high particle density is not possible either because of the loss of distinctive particle patterns, which lead to ambiguous correlation peaks. Another rule of thumb is called *Adrian's one-quarter-rule* (Keane and Adrian, 1990), which states that the size of the correlation window has to be at least four times bigger than the maximal displacement in order to allow a proper determination. These guidelines limit the choices of parameters to yield the best achievable result throughout the entire image. Especially flows with large velocity gradients suffer from this restrictions because the large displacements conceal small motions that are lost due to the averaging effect.

A solution to this vicious circle was found by using a hierarchical approach. The images are first processed with large correlation window sizes to capture the large displacements. In the following step, the correlation window size is reduced but also shifted by the previously estimated displacement. This way the overlap of mutual information remains large enough to give meaningful results. This approach was

published under the name discrete window offset (Westerweel et al., 1997) and makes up for the deficiency of a limited dynamic range. Still, the method has problems with the estimation of flows with strong velocity gradients. A shearing of the image pattern can decrease the correlation value drastically as shown in the article of Scarano (2002). Especially for particle images this becomes an issue because the particles have usually a narrow width (<3 pixels). Shearing the particle pattern leads to a broadening of the correlation peak and a reduced peak height. As a consequence, commonly used peak detectors (e.g. 3-point Gaussian fit, (Raffel et al., 2007, p.160)) have difficulties to localize the maximum accurately. Rather than pre-shifting the correlation window Scarano (2002) proposed to distort the image with respect to the previously estimates. The method is based on the research of Huang et al. (1993a,b) who applied an image distortion to make up for the disadvantageous shearing effect. The original data is altered in each hierarchical level because the image is corrected by the estimate of the previous level. Distorting the image requires a high accuracy of image interpolation schemes (Astarita and Cardone, 2005; Astarita, 2006) in order to work properly. Nevertheless, this method performs best and therefore most commercial and research PIV algorithms are based on image deformation (Stanislas et al., 2003, 2005, 2008).

3.2.1.2 Extensions of PIV

A serious disadvantage for the research of turbulent flows is the limitation of PIV to estimate just velocities in the illuminated plane. This is the reason why this method is classified as *2D2C* method, it allows to estimate two dimensions and two components of the velocity field. However, the knowledge of the entire velocity field in three dimensions and three components is necessary to allow a thorough investigation of turbulent fluid structures. A straight forward approach is to use two cameras in a stereoscopic setting in order to determine the third component of $\boldsymbol{u}$ by the parallax of the particles (Arroyo and Greated, 1991). This allows to estimate the entire velocity vector, but just within a planar domain. In order to capture also the third dimension Kähler and Kompenhans (2000) used a fast scanning planar illumination through the volume in combination with the stereoscopic PIV technique. This works quite well but not for fast flows because during the scan the flow structures are changing. However, the holy grail for fluid dynamicists is the possibility to measure all three components of $\boldsymbol{u}$ in a volume instantaneously. This allows to compare the results directly to CFD computations. One method uses holography to estimate the *3D3C* velocity field (Hinsch, 2002) but it is very inconvenient to perform the measurement and to evaluate the hologram from photographic films. The other method and current state-of-the-art technique uses a tomographic approach. Multiple cameras record a particle-laden flow from different perspectives (Elsinga et al., 2006; Elsinga, 2008). The images can be used to reconstruct the particle density for two consecutive time steps, from which the motion is estimated by means of correlation.

3.2.2 Gradient based

Although the expression optical flow refers to the apparent motion field of objects or image structures within the image, it is commonly also used to refer to image gradient based methods in order to estimation the motion. The optical flow data term can be

derived in various ways. One of them originates from the assumption that the image brightness remains constant along its trajectory

$$I(\boldsymbol{x}(t), t) = const\,. \tag{3.9}$$

This means especially that the total derivative with respect to the time is zero $\frac{d}{dt}I(\boldsymbol{x}(t), t) = 0$. The expansion into the substantial derivative gives the so-called *brightness constancy constraint equation* (BCCE), which has to be satisfied at all pixels

$$0 = \partial_t I + \boldsymbol{u}^T \nabla I\,, \tag{3.10}$$

where ∇ is the spatial gradient operator. This equation resembles the continuity equation of incompressible flows and has equivalent properties. It states that no intensity gets lost or is produced. It is the differential formulation of the conservation of intensity. The second way to derive the BCCE is by performing a Taylor expansion for small displacements $\|\boldsymbol{d}(\boldsymbol{x})\| \ll 1$ of the integrand in equation (3.4) and to disregard higher-order terms. It is assumed that I_i and I_{i+1} are very similar and the difference can be explained by a linear translation of the brightness. For a small displacement field $\boldsymbol{d}_i$ the second image can be represented sufficiently good by the Taylor approximation of the first image

$$I_i(\boldsymbol{x} + \boldsymbol{d}_i) = I_i(\boldsymbol{x}) + \boldsymbol{d}_i^T \nabla I_i(\boldsymbol{x}) + \frac{1}{2}\boldsymbol{d}_i^T \nabla I_i(\boldsymbol{x}) \nabla^T I_i(\boldsymbol{x}) \boldsymbol{d}_i + \mathcal{O}(\boldsymbol{d}_i^3)\,. \tag{3.11}$$

Dropping higher-order terms beyond the second-order yields $I_i + \boldsymbol{d}_i \nabla I_i$. Subtracting this first-order Taylor approximation from the consecutive image I_{i+1} and replacing $(I_{i+1} - I_i)$ with $\delta t \partial_t I$ and dividing by the separation time δt gives the very same BCCE as shown in equation (3.10).

The second derivation reveals more obviously the shortcoming of the gradient approach. The Taylor approximation is just accurate for small displacements, so that the trajectory can be approximated by a linear motion. For large displacements this is in general not correct. The motion estimation for all pixels can be bundled by applying a norm of the BCCE. Rather than finding the root, the constraint is relaxed and reformulated as a minimization problem of the cost functional J

$$J(\boldsymbol{u}) = \frac{1}{2}\|\partial_t I + \boldsymbol{u}^T \nabla I\|_\Omega^2 \qquad \rightarrow \qquad \min\,, \tag{3.12}$$

in order to account for noise or neglected effects that change the brightness. The factor $1/2$ is introduced for convenience and has no effect on the location of the minimum. Still, the minimization problem in equation (3.12) is underdetermined and needs a regularization to render it well-posed. This can be achieved by either grouping information from multiple pixels or regularizing the solution $\boldsymbol{u}$ (Tikhonov and Arsenin, 1977). The first approach leads to *local* optical flow methods (see p. 28) and the latter to *global* optical flow methods (see p. 30).

3.2.2.1 Aperture problem

Looking at small parts of an images might cause problems because motion might appear differently and cannot be determined correctly. This happens if the underlying brightness structures are much larger than image part in focus. Figure 3.4 illustrates this issue by showing an one-dimensional brightness structure that inheres a motion. From the point of the observer, the motion can not be determined uniquely because many different motions are imaginable. Unless there is a two-dimensional structure within the close-up, it is not possible to determine the motion confidently. This problem is referred to as the *aperture problem* (Marr and Ullman, 1981).

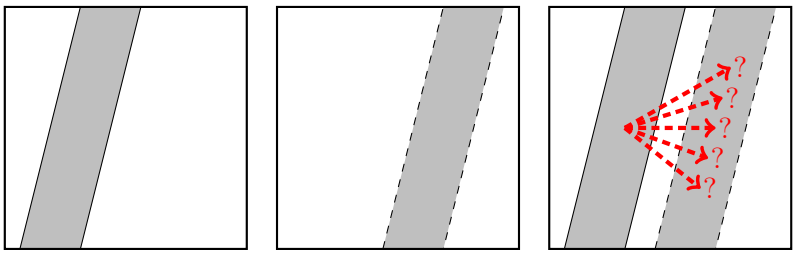

Figure 3.4: Illustration of the *aperture problem*. The image structure is too large to be seen entirely, so that the close-up shows just a one-dimensional structure. As a consequence, many different motions are possible that can explain the two images.

Especially optical flow methods suffer from this phenomenon because the motion information is estimated pixelwise and cannot contain two-dimensional structures. The best local estimate with lowest energy is the so-called *normal flow* $\boldsymbol{u}^\perp$ (Horn, 1986), which points in the direction of the image gradient and reads

$$\boldsymbol{u}^\perp = -\partial_t I \frac{\nabla I}{\|\nabla I\|^2} \,. \tag{3.13}$$

The aperture problem gets less significant if larger images parts are used to determine one motion estimate because it is more likely that it contains two-dimensional patterns.

3.2.2.2 Local methods

Lucas & Kanade

Just like correlation methods, Lucas and Kanade (1981) proposed to include the information of neighboring pixels so that the problem becomes overdetermined. Each pixel of a spatial neighborhood $\mathcal{N}$ contributes to the BCCE

$$\min_{\boldsymbol{u}} J(\boldsymbol{u}) \qquad \text{with} \qquad J(\boldsymbol{u}) = \frac{1}{2} \sum_{\mathcal{N}} (\partial_t I + \boldsymbol{u}^T \nabla I)^2 \,. \tag{3.14}$$

The minimizer has to satisfy the first-order necessary condition $J'_{\boldsymbol{u}}(\boldsymbol{u})(\delta\boldsymbol{u}) = 0$, which yields

$$0 = \sum_{\mathcal{N}} (\partial_t I + \boldsymbol{u}^T \nabla I) \nabla I \delta \boldsymbol{u} \,. \tag{3.15}$$

The equation has to be true for all variations $\delta\boldsymbol{u}$ so that it can not depend on it. This gives a system of equations that can be used to compute $\boldsymbol{u}$

$$\underbrace{\sum_{\mathcal{N}} \begin{bmatrix} I'_x I'_x & I'_x I'_y \\ I'_y I'_x & I'_y I'_y \end{bmatrix}}_{\boldsymbol{S}} \begin{pmatrix} u \\ v \end{pmatrix} = \underbrace{-\sum_{\mathcal{N}} \begin{pmatrix} I'_x I'_t \\ I'_y I'_t \end{pmatrix}}_{\boldsymbol{b}} \,. \tag{3.16}$$

The matrix $\boldsymbol{S}$ is called *structure tensor* and contains information about the predominant motion within $\mathcal{N}$ (Bigün, 2006). This linear system can be easily inverted to get an ensemble velocity estimate $\boldsymbol{u} = \boldsymbol{S}^{-1}\boldsymbol{b}$ for the entire neighborhood $\mathcal{N}$.

Bigun

A second method from Bigün et al. (1991) reformulates equation (3.14) as inner product of a three-component vector $\nabla_3 = (\partial_x, \partial_y, \partial_t)^T$ and an extended velocity vector $\boldsymbol{u}_e = (u, v, 1)^T$, which yields

$$\min_{\boldsymbol{u}_e} \sum_{\mathcal{N}} (\boldsymbol{u}_e^T \nabla_3 I)^2 \,. \tag{3.17}$$

The squared parenthesis can be expanded and reordered such that it resembles a quadratic form $\boldsymbol{u}^T\boldsymbol{S}\boldsymbol{u}$ with $[\boldsymbol{S}_{ij}] = \sum_{\mathcal{N}} I'_i I'_j$ for $i, j = \{x, y, t\}$ being the positive definite structure tensor, which contains the integrated correlations of all pairwise gradients. If $\mathcal{N}$ includes at least two pixels then $\boldsymbol{S}$ has full rank and can be diagonalized by an orthogonal matrix $\boldsymbol{Q}$

$$\min_{\|\boldsymbol{u}_e\|=1} \; \boldsymbol{u}_e^T \underbrace{\boldsymbol{Q}^{-1}\Lambda\boldsymbol{Q}}_{S} \boldsymbol{u}_e \,. \tag{3.18}$$

A vector $\boldsymbol{u}_e$ with length one has to be found such that the cost are minimized. This happens when $\boldsymbol{u}_e$ equals the eigenvector $\boldsymbol{e}_{min}$ that corresponds to the smallest eigenvalue of Λ. The velocity can be estimated from $\boldsymbol{e}_{min} = (e_1, e_2, e_3)^T$ by dividing the spatial components by the temporal component,

$$\boldsymbol{u} = \frac{(e_1, e_2)^T}{e_3} \,. \tag{3.19}$$

From a statistical point of view, this method can be seen as principle component analysis in the phase space of the gradients $\nabla_3 I$. Figure 3.5 illustrates this issue by showing the ellipsoid of gradients $(\partial_x I, \partial_y I, \partial_t I)$ whose orientation encodes the velocity (Jähne, 2006). The inclination of the principle axis is related to the magnitude, while its azimuthal orientation is connected to the direction of the motion. Since the motion has to be orthogonal to the principle axis of the image gradient ellipsoid, it is chosen such that the smallest energy λ_3 is necessary (*normal flow*).

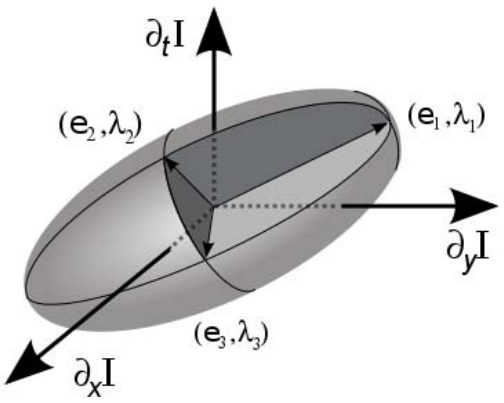

Figure 3.5: This figure shows the ellipsoid of image gradients whose orientation contains information of the inherent motion.

3.2.2.3 Global methods

Horn & Schunck

The methods presented before used spatial averaging of the data term in order to render the problem well-posed. The other possibility is to demand a certain regularity of the solution $\boldsymbol{u}$, the so-called *Tikhonov regularization* (Tikhonov and Arsenin, 1977). Horn and Schunck (1981) added a penalizing term that adds the gradients of the solution to the cost functional in order to enforce smooth results. The minimization problem of the *Horn & Schunck* optical flow reads

$$\min_{\boldsymbol{u}} J(\boldsymbol{u}) \quad \text{with} \qquad J(\boldsymbol{u}) = \|\boldsymbol{u}^T \nabla I + \partial_t I\|_\Omega^2 + \frac{\alpha^2}{2} \|\nabla \boldsymbol{u}^T\|_\Omega^2 \,, \tag{3.20}$$

where $\nabla \boldsymbol{u}^T$ is a matrix containing the derivatives of the velocity components with respect to the coordinates. The parameter $\alpha \in \mathbb{R}$ controls the degree of regularity and is a user-defined parameter. The general idea is that nearby motion estimates are not supposed to be very different. This assumption is especially true for fluid flows images because their motion field is usually not discontinuous. For any regularization parameter $\alpha > 0$ the problem gets well-posed (see Appendix A.10) and has to be chosen in such a way that the solution has the desired smoothness but still depends mostly on the image data. The effect of the regularization parameter onto the neighbors can be illustrated by estimating its correlation length. For this reason an one-dimensional image was used where just **one** pixel has a non-zero motion. The motion from this pixel would propagate over the entire image until there is a uniform velocity, if there would be no brightness information at the other pixels. However, if ∇I is non-zero and $\partial_t I$ is set to zero, it is possible to show the spreading of a single motion information over the nearby pixels (see figure 3.6). This shows that such a regularization can corrupt significantly correct local estimates if the regularization parameter α is chosen to large. Unfortunately, a reasonable choice depends on the distribution of the image gradients and cannot be determinable beforehand.

This example shows the global behavior of this method. Large gradients in one location affect all other estimates in the domain.

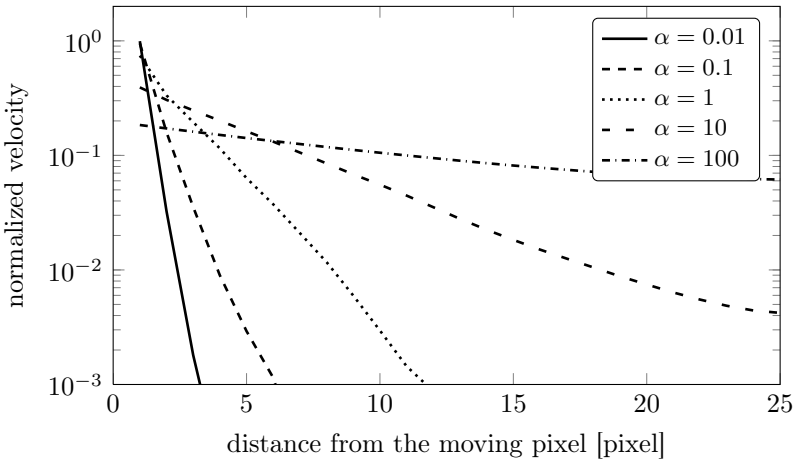

Figure 3.6: This graph shows the effect of increasing regularization parameter α and its influence to the propagation of motion information. The larger α gets, the wider the information is spread over the nearby estimates. This is accompanied by a decreased magnitude of the actual estimate.

In order to find the solution $\boldsymbol{u}$, one uses the first-order necessary condition $J'_{\boldsymbol{u}}(\boldsymbol{u})(\delta\boldsymbol{u}) = 0$, which leads to

$$J'_{\boldsymbol{u}}(\boldsymbol{u})(\delta\boldsymbol{u}) = \| \left(\boldsymbol{u}^T \nabla I + \partial_t I\right) \nabla I \delta\boldsymbol{u} + \alpha^2 \nabla\boldsymbol{u} \nabla\delta\boldsymbol{u} \|_\Omega = 0\,. \tag{3.21}$$

Due to the rule of *summation by parts*, the derivative operator in front of the variation can be swapped to the velocity and turns it into a Laplacian operator Δ. The equation gets linearly dependent of the variation $\delta\boldsymbol{u}$. Since the variation is arbitrary the equation can not depend on it, which yields the second-order partial differential equation

$$0 = \left(\boldsymbol{u}^T \nabla I + I_t\right) \nabla I - \alpha^2 \Delta\boldsymbol{u}\,. \tag{3.22}$$

Horn and Schunck (1981) replaced the Laplacian with a finite difference representation $\Delta\boldsymbol{u} \approx \bar{\boldsymbol{u}} - \boldsymbol{u}$, where $\bar{\boldsymbol{u}}$ is a weighted average of the estimates in the neighborhood. Without the Laplacian, the solution $\boldsymbol{u}$ can be computed with

$$\boldsymbol{u} = \left[\nabla I \nabla I^T + \alpha^2 \mathbb{1}\right]^{-1} \left(\alpha^2 \bar{\boldsymbol{u}} - \partial_t I \nabla I\right). \tag{3.23}$$

The gain of this first-order approximation of the data term is that the cost functional becomes strictly convex (Schnörr, 1991), which allows to proof the existence of global minimizers and to use efficient linear solvers to find them. Horn and Schunck (1981) proposed the *Gauss-Seidel* method to solve the linear system because the matrix doesn't have to be assembled and can be solved iteratively.

3.2.2.4 Extensions of optical flow

One of the foremost advantages of optical flow is that the cost functional can be adapted easily to model all kinds of different experimental situations. Where correlation methods need to perform multiple individual steps to account for different effects (e.g. motion, decay,...), optical flow allows an all-in-one formulation that needs to be solved. As a consequence there are many publications where the method is adapted to fit a certain situation.

Similar to correlation techniques, gradient based techniques use hierarchical methods to overcome the limitations of the first-order Taylor approximation. The images are usually scaled in a pyramidal manner (Burt and Adelson, 1983) so that the last level contains just velocities that are below $1\,{}^{\text{pixel}}/_{\delta t}$. The motion field from this level is transferred to the next larger level and used as an offset until the final resolution is reached. Alternatively, *scale-space* methods can be used, which apply a smoothing to the image, so that the autocorrelation length of large displacements is increased and can be estimated by optical flow. The smoothing is gradually reduced and the motion estimates corrected until the original image is restored Alvarez et al. (1999).

The adequate modeling of illumination changes is crucial for optical flow, since it is based on gradients. Comparable to the continuity equation of fluid dynamics Wildes et al. (1997) extended the BCCE to $\partial_t I = -\nabla^T(\boldsymbol{u}I)$, which allows sinks and sources of the brightness. This is especially useful for emerging brightness structures (e.g. clouds). A generalized model for illumination changes has been presented by Haußecker and Fleet (2001), who introduced a function that depends on the initial image, the time and some brightness change model parameters.

Physical modeling has been first applied by Corpetti et al. (2002), who imposed the smoothness of physical characteristics. Rather than regularizing the motion field $\boldsymbol{u}$, he enforced the smoothness constraint on the divergence and the vorticity of $\boldsymbol{u}$ by adding

$$\|\nabla \operatorname{div} \boldsymbol{u}\|^2 \qquad \text{and} \qquad \|\nabla \operatorname{curl} \boldsymbol{u}\|^2 \tag{3.24}$$

to the cost functional. For highly viscous flows it would make sense to penalize the divergence and vorticity. Penalizing the gradients has the advantage that physical relations (e.g. zero divergence) might be violated in a two-dimensional projection.

3.2.3 PDE modeled optical flow

Up to this point, the presented methods used localized features that are smoothly linked to each other rather than global motion models. The huge benefit of fluid flow is that it satisfies certain motion equations, which for instance are used for simulations. The connection of computer simulation and motion estimation was first done by Nakajima et al. (2003), who included the Navier-Stokes equations as weighted penalizing terms (α_1, α_2) into the cost functional

$$J(\boldsymbol{u}) = \alpha_1 \|\partial_t I + \boldsymbol{u}^T \nabla I\|_\Omega^2 + \|\nabla^T \boldsymbol{u}\|_\Omega^2 + \alpha_2 \|\frac{\mathrm{D}\boldsymbol{u}}{\mathrm{D}t} + \frac{1}{\rho}\nabla p - \nu\Delta\boldsymbol{u} - \boldsymbol{f}\|_\Omega^2 . \tag{3.25}$$

The corresponding non-linear Euler-Lagrange-equations were solved in order to obtain the motion field. Other researchers tried to denoise the estimated motion field by using physical PDEs (Vlasenko and Schnörr, 2008; Doshi and Bors, 2010). The work of Ruhnau (2006) extended the combination of simulation and measurement to the field of optimal control. The previous method required the knowledge of the precise boundary conditions. With optimal control Ruhnau and Schnörr (2006) were able to estimate the boundary in such a way that the cost functional

$$J(\boldsymbol{u}, \boldsymbol{f}, \boldsymbol{g}) = \|\partial_t I + \boldsymbol{u}^T \nabla I\|_\Omega^2 + \frac{\alpha_1}{2}\|\boldsymbol{f}\|_\Omega^2 + \frac{\alpha_2}{2}\|\boldsymbol{n}^T \nabla \boldsymbol{g}\|_{\partial\Omega}^2 \tag{3.26}$$

becomes minimal under the constraints (Stokes equations)

$$\left\{ \begin{array}{rcl} -\mu\Delta\boldsymbol{u} + \nabla p &=& \boldsymbol{f} \quad \text{, in } \Omega \\ \nabla^T \boldsymbol{u} &=& 0 \quad \text{, in } \Omega \\ \boldsymbol{u} &=& \boldsymbol{g} \quad \text{, on } \partial\Omega \end{array} \right. . \tag{3.27}$$

This approach allowed to relax the governing equations by the introduction of parameters, that are determined in such a way that the cost functional becomes minimal. Since the motion equations act as constraints the result will satisfy them in contrast to the method of Nakajima et al. (2003), which balances between accurate PDE solution and data term. However, the disadvantage remains that regularization parameters α_1, α_2 have to be chosen manually in order to balance the individual terms.

3.3 Comparison of the motion methods

The presented method can be compared by their behavior with respect to data. Figure 3.7 shows an analogue representation of PIV, optical flow and PDE constrained motion estimation. A parabola is sampled at discrete locations and corrupted with noise. PIV estimation can be compared to a convolution and estimates a linearly interpolated function. Optical flow behaves like a spline-fit that minimizes the distances to the points but has also restrictions on the gradient of the function. In this analogy the PDE constrained model corresponds to knowing the correct model function and using it in order to fit the data. This gives of course the best result. A drawback of all presented methods are, that certain user-defined parameters have to be chosen. These dependent on the actual ground truth motion and the images and are usually set intuitively. Commonly used values ($\alpha = 0.01$) might lead to inaccurate results if the underlying motion field or brightness pattern is very inhomogeneous.

Local motion methods have the advantage that errors can not propagate to other estimates. The spatial averaging of the data allows to compute confidence measures in order to rate the trustworthiness of such estimates. In case of local optical flow methods these measures originate from the analysis of the matrix $\boldsymbol{S}$. For correlation methods it is common to use the ratio of the two highest peaks. These confidence measures are used to accept or reject estimates locally and to replace inappropriate ones by suitable values, e.g. (Westerweel and Scarano, 2005).

On the other hand, global methods connect all estimates to each other, which leads to an error propagation that is difficult to predict because it depends strongly on the

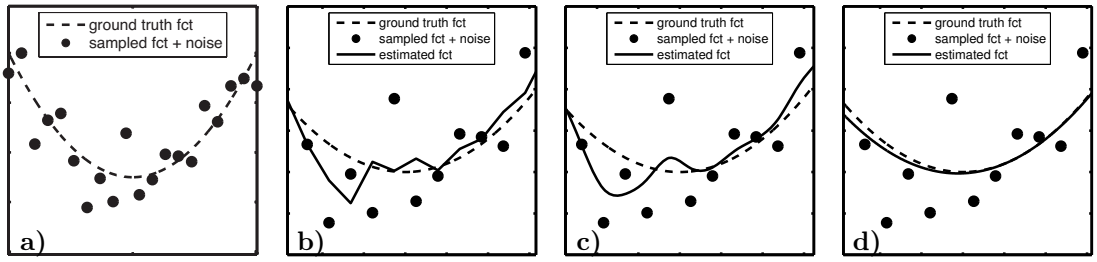

Figure 3.7: These four graphs illustrate the different approaches in order to recover the noise corrupted signal in **a)**. PIV compares to a convolution of the data points with a boxcar function as shown in **b)**. Optical flow in **c)** has constraints that connect neighboring estimates by the regularization parameter. The best method uses of course the correct model to fit the data points, see **d)**. This compares to the PDE constraint motion estimation.

images. Large erroneous estimates contaminate all other estimates and lead to a slower convergence of the iterative solvers. However, they allow to incorporate models that account for physical properties of the measured fluid motion. Global optical flow is sensitive to outliers due to its least-squares character. In order to reduce this influence scientist experimented with other norms that are less prone to outliers (Black and Anandan, 1993; Bab-Hadiashar and Suter, 1996). Local measures of reliability are not at hand because of the propagation of motion information that can corrupt the estimates globally. The usual measure of quality is the value of the BCCE, $\|\partial_t I + \boldsymbol{u}^T \nabla I\|_\Omega^2$, which is assumed to be very low for good quality results. For instance, other confidence measures depend on the magnitude of the image gradient (Bruhn and Weickert, 2006).

The approach of combining PDEs and optical flow gives the major advantage of providing global motion models. The motion estimates are linked by a rigid law that restricts the solution. If included as a constraint, the estimated motion satisfies perfectly the PDEs. There are no local outliers because the equations do not permit such deviations. Localized wrong image data alters the solution globally and not locally. This makes it difficult to quantify the confidence if the ground truth solution is unknown. All results from this technique seem physically sound, so that confidence measures need to be found. Since PDEs have to be solved for this technique, the usual approach uses FEM, which entails a high computation effort for images that contain millions of pixels. However, combining optimal control of PDEs with motion estimation allows a flexible modeling of the physical motion equation.

CHAPTER 4

Microfluidic Flows

Within the past decade, the development of microfluidic devices gained more and more attention. The evidence can be found in the many published textbooks that deal with nano- and microfluidics (Liou and Fang, 2006; Bruus, 2007; Karniadakis et al., 2005; Kirby, 2010; Fritzsche, 2012). The miniaturization of devices down to the smallest achievable scales brings several benefits. Especially in biology (Beebe et al., 2002; Verpoorte, 2002) and medicine (Yager et al., 2006; Squires and Quake, 2005), where large quantities of substances are usually not at disposal, it is of tremendous value to develop instruments, which can operate with tiny amounts of material. Along with the miniaturization comes, of course, the possibility to create portable devices but also energy efficiency is an important issue. Applications of nano- and micro-flows occur in many different scientific and engineering areas, such as inkjet printers (Meinhart and Zhang, 2000), blood analysis (Chang et al., 2000) or patient diagnosis devices (Nguyen and Wereley, 2002, chap. 4+5). As for the miniaturization of electrical circuits, there is also a change of regime for miniature fluid flows. While entering the small-scale regime of flows, common tasks can become inefficient or even impossible. Mixing is an example for such tasks. In moderate size flows it is common to mix two liquids by pouring one into the other or by stirring them. In the low Reynolds number regime ($\mathrm{Re} < 1$) this is a difficult endeavor because efficient mixing is just possible with turbulence. The Péclet number Pe is a nondimensional number that puts the advective transport in relation to the diffusive transport. It is defined as $\mathrm{Pe} = {}^{U\ell}/_{\kappa}$, a typical length scale ℓ, a velocity scale U and the mass diffusion coefficient κ of the fluid. For most miniature flows the product of the length and velocity scale is still some orders larger than the molecular diffusion κ ($\mathrm{Pe} = 10^2 \ldots 10^4$) (Hardt and Schönfeld, 2007, p. 122) and consequently the transport is mostly driven by advection than by diffusion. An example of the slow mixing effect due to diffusion was given in Bau et al. (2001): At room temperature myosin proteins have a diffusion coefficient of $\kappa \approx 10^{-11}\,\mathrm{m}^2/\mathrm{s}$. In order to travel across a $100\,\mu$m channel requires circa 1000 sec, which is to long for most engineering applications. Several attempts have been made to improve mixing in an active or passive manner. Passive methods involve micro-structuring the walls, geometrical obstacles in the duct while active methods utilize temperature, electrical, magnetic or acoustical stimulations. An extensive overview about mixing in microscopic scales can be found in the book of (Hardt and Schönfeld, 2007, p. 117–155).

4.1 Governing equations of fluid motion

The general motion equations of continuous fluids can be derived from Newton's law of momentum conservation (Batchelor, 2000, pp. 137) and are commonly known as *Navier-Stokes equations*. Under the assumption of a uniform viscosity μ throughout the fluid and an incompressible fluid, the equations simplify to

$$\rho\frac{D\boldsymbol{u}}{Dt} = -\boldsymbol{\nabla}p + \mu\Delta\boldsymbol{u} + \rho\boldsymbol{f} \qquad \text{(momentum equation)} \tag{4.1}$$

$$0 = \boldsymbol{\nabla}^T\boldsymbol{u} \qquad \text{(continuity equation)}\,, \tag{4.2}$$

where $\boldsymbol{u} : \Omega_3 \to \mathbb{R}^3$ is the velocity, $p : \Omega_3 \to \mathbb{R}$ is the pressure and $\boldsymbol{f} : \Omega_3 \to \mathbb{R}^3$ are external forces that act on the fluid. The equations can be rewritten in a nondimensional form by introducing a reference length ℓ and velocity U (see Appendix A.1)

$$\begin{aligned}\frac{D\boldsymbol{u}^*}{Dt^*} = \frac{\partial\boldsymbol{u}^*}{\partial t^*} + (\boldsymbol{u}^{*T}\boldsymbol{\nabla}^*)\boldsymbol{u}^* &= -\boldsymbol{\nabla}^* p^* + \frac{1}{\mathrm{Re}}\Delta^*\boldsymbol{u}^* + \frac{\ell}{U^2}\boldsymbol{f}^* \\ 0 &= \boldsymbol{\nabla}^{*T}\boldsymbol{u}^*\,.\end{aligned} \tag{4.3}$$

In absence of external forces ($\boldsymbol{f} = 0$), all dimensional scales are combined in the Reynolds number $\mathrm{Re} = \frac{\rho U\ell}{\mu}$, which is nondimensional. The Reynolds number weighs the importance of the viscosity forces with respect to the inertia forces and therefore controls its dominance in the equation. In order to keep the notation as easy as possible, the superscript "*" will be omitted in the following. For most microfluidic applications the Reynolds number is very low ($\mathrm{Re} \ll 1$). A typical fluid for micro devices is water ($\mu \approx 0.001\,\mathrm{Pa{\cdot}s}$, $\rho \approx 1000\,\mathrm{kg/m^3}$), common length scales ranging from $1\,\mu\mathrm{m}$ to $1\,\mathrm{mm}$ and velocities from $1\,\mu\mathrm{m/s}$ to $1\,\mathrm{cm/s}$ (Squires and Quake, 2005). This results in a wide range of possible Reynolds number starting from 10^{-6} to 10^{1}. In these cases the viscosity term $\Delta\boldsymbol{u}$ is much more dominant than the inertia term $(\boldsymbol{u}^T\nabla)\boldsymbol{u}$. This argument allows to neglect the latter term and $\partial_t\boldsymbol{u}$ can also be neglected by considering just stationary flows. Consequently, the Navier-Stokes equations simplify to

$$\begin{aligned}\mathbf{0} &= -\boldsymbol{\nabla}p + \frac{1}{\mathrm{Re}}\Delta\boldsymbol{u} \\ 0 &= \boldsymbol{\nabla}^T\boldsymbol{u}\,.\end{aligned} \tag{4.4}$$

The remaining equations are called *Stokes equations* and the corresponding flows *Stokes flows*, respectively. In mathematics these equations belong to the class of elliptic boundary value problems. This means that the problem is well-posed and has a unique solution $(\boldsymbol{u}, p)$ that fulfills equation (4.4), if the solution is given at the boundaries of the domain. The proofs of existence and uniqueness of a solution can be found in various textbooks (Temam, 1979, chap 1, §2 ; Ladyzhenskaya, 1969) along with an extensive discussion about the mathematical properties of the more general Navier-Stokes equation.

It has to be remarked that in some flow cases the description with the Navier-Stokes equation could be inappropriate. This happens if the flow cannot be modeled as a continuous medium any more. It has to be treated as a particle flow that includes

particle convection and particle collisions. In this case the flow has to be described by the Boltzmann equation from statistical mechanics. A typical example is a rarefied gas, where the molecules are separated far away from each other (e.g. like expelling gas into a vacuum), which renders the definition of gradients, viscosity, etc. meaningless. This applies also to nano-flows because the dimension of the flow ℓ is of the order of the molecular mean free path λ, $\mathcal{O}(\ell) = \mathcal{O}(\lambda)$. The Knudsen number $\mathrm{Kn} = \lambda/\ell$ defines the ratio between the free path length λ and this characteristic length ℓ. In general it can be said that the larger Kn, the less valid is the continuity assumption. The commonly accepted range for the validity of the continuum assumption and consequently the Navier-Stokes model is bounded by $\mathrm{Kn} < 0.01$ (Karniadakis et al., 2005, p. 16). The Navier-Stokes equations can be derived from the Boltzmann equations by using the *Chapman-Enskog expansion* of the first-order in Kn (see Liou and Fang, 2006, p. 62). Higher-order expansions yield the *Burnett* equations (Burnett, 1936) and can be used to describe flows with Kn up to unity. The assumption of a continuum gets easily violated for nano-scale gas flows but also for micro-flows that contain large molecules like polymers or DNA. For these examples Kn can reach the limit of the Navier-Stokes equations so that other models have to be considered.

4.2 Boundary Conditions

The *no-slip* boundary condition has been controversially discussed over the past 200 years, see (Goldstein, 1938, pp. 676–680) and Day (1990). Some experiments revealed for micro- and nano-scale flows that there were unexpected discrepancies between measurements and the predictions, which included the *no-slip* boundary condition (Joseph and Tabeling, 2005; Cheng and Giordano, 2002). A general boundary condition can be derived from the Boltzmann equation and has the form (Karniadakis et al., 2005, p. 69)

$$\boldsymbol{u}_{slip} - \boldsymbol{u}_{wall} = \frac{2 - \sigma_v}{\sigma_v} \left(\lambda \frac{\partial \boldsymbol{u}}{\partial \boldsymbol{n}} + \frac{\lambda^2}{2} \frac{\partial^2 \boldsymbol{u}}{\partial \boldsymbol{n}^2} + \mathcal{O}(\lambda^3) \right) , \tag{4.5}$$

where the wall-slip $\boldsymbol{u}_{slip}$ is expanded in a power series of λ, $\boldsymbol{n}$ is the boundary normal and $\boldsymbol{u}_{wall}$ the velocity of the wall. The first factor contains the tangential momentum accommodation coefficient σ_v, which describes the interaction of the gas with the walls. More precisely, it is the ratio of elastic molecule rebounds from the wall to the inelastic molecules rebounds. The equation (4.5) can be nondimensionalized, which yields a slip velocity that is a power series of the Knudsen number Kn. It can be seen that for very small Knudsen numbers the slip velocity tends to zero and the commonly applied *no-slip* condition is justifiable. Already Maxwell (1878) introduced a first-order slip boundary condition, which models a slipping effect by introducing the slip length β that is still used nowadays

$$\boldsymbol{u} - \boldsymbol{u}_{wall} = \beta \frac{\partial \boldsymbol{u}}{\partial \boldsymbol{n}} . \tag{4.6}$$

The first-order slip velocity is sufficiently accurate for Navier-Stokes flows, since they are both first-order models. If the Navier-Stokes equations fail to describe the flow

precisely, higher-order slip models have to be considered. Examples of such cases are given in Leger et al. (1997) and Mhetar and Archer (1998), where polymers produce a non-linear dependency for the slip velocity. Moreover, the slip length depends strongly on the fluid-solid interaction. Wetting fluids are more likely to reduce the slip while hydrophobic surfaces lead to a reduced drag and larger slip (Priezjev, 2007; Tretheway and Meinhart, 2002). The roughness of the solid walls has a major influence on the wettability and therefore also on the magnitude of slip. By texturizing the walls it is possible to enforce hydrophobicity, which is accompanied by an increase of the slip length β and this leads to a larger mass flow (Quéré, 2008). This is especially favorable for miniature devices that need to transport fluid with the least amount of energy. A general overview about the description and the influential parameters of the boundary condition is given in (Tropea et al., 2007, chap. 19). The commonly accepted range of Kn for the slip regime is $\mathrm{Kn} = 10^{-3} \ldots 10^{1}$ (Xu and Li, 2004; Karniadakis et al., 2005), where at least the additional linear terms of equation (4.5) have to be used. However, the *no-slip* boundary condition is sufficiently accurate for small $\mathrm{Kn} < 10^{-3}$.

The measurement of slip-velocities is a challenging task because of its small magnitudes. Especially, PIV has the disadvantage of estimating just average velocities that make the detection of large velocity gradients difficult.

4.3 Microchannel flow

The flow through a miniature rectangular channel is used as a test case of microfluidics. The advantage of this setup lies in the fact that there is an analytical solution for pressure-driven flows (*Poiseuille flows*). The laminar solution can be derived (see Appendix A.3) under the assumption of the *no-slip* boundary condition at the wall ($\boldsymbol{u} = \mathbf{0}$) and a given pressure drop $\delta p = p_{out} - p_{in}$ between the inlet and the outlet of the channel

$$u(y,z) = \frac{16}{\pi^4} \frac{(p_{out} - p_{in})}{\mu L} \sum_{odd\ n,m}^{\infty} \frac{1}{\left(\frac{n^2}{W^2} + \frac{m^2}{H^2}\right) nm} \sin\left(n\frac{\pi}{W}y\right) \sin\left(m\frac{\pi}{H}z\right) . \tag{4.7}$$

The parameter L, W and H represent the length, width and height of the channel while μ is the dynamic viscosity. The lateral velocity components v and w are normal to the pressure gradient are consequently zero. The sum stems from a Fourier series and takes account for the rectangular shape of the channel. In case of a duct with a round cross-section, the equation (4.7) simplifies to the *Hagen–Poiseuille* equation.

4.3.1 Experimental data

The accurate measurement of microfluidic flows is more difficult compared to flow measurements of moderate dimensions ($\ell \sim 1\,m$). This is due to the fact that probing the flow requires an intrusion into the flow. The probing has to be less intrusive as usual because the fluid quantity is so small. There are several means available how to measure the velocity (Nguyen and Wereley, 2002, pp. 138; Sinton, 2004). Most often micron particles are used to visualize the motion. For micro-flows one runs the risk of altering the viscosity coefficient due to a high percentage of particles (Einstein, 1906,

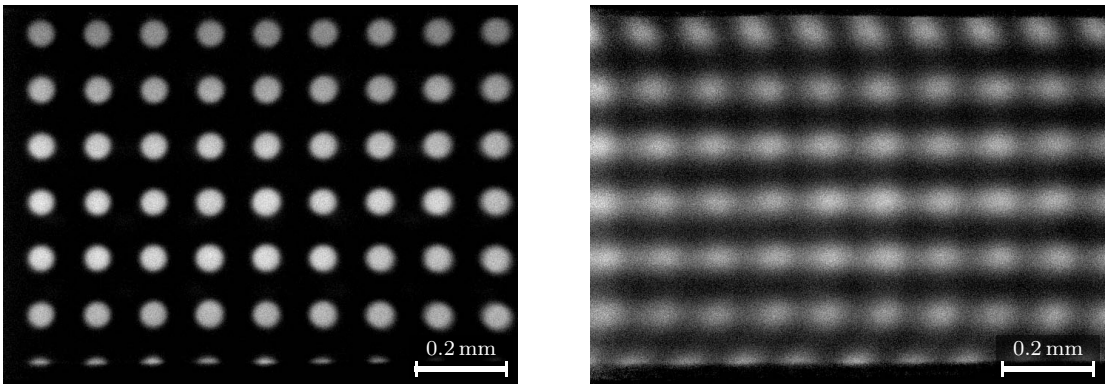

Figure 4.1: The left image shows the MTV pattern at the time when it was written into the channel. The right image shows the distorted and diffused pattern after nearly 3.5 sec.

1911; Taylor, 1932). Nevertheless, this flow visualization method is used to estimate the velocity in micro-flows by common techniques, such as *Laser Doppler Anemometry* (Durst et al., 1981) and *μPIV* (Santiago et al., 1998; Nguyen and Wereley, 2002; Kirby, 2010). The molecular counterpart of these visualization techniques uses fluorescent dye molecules as tracers and is called *Laser Induced Fluorescence* (LIF). The molecules are introduced in the flow and excited with a laser of the appropriate wavelength in order to excite fluorescence light that can be recorded by photographic systems. The advantage is a minimal intrusion into the dynamics of the flow. However, it is nearly possible to obtain accurate motion estimates from LIF images because the velocity can only be estimated at the interface of the fluorescent to the non-fluorescent liquid. In addition, the aperture problem (see section 3.2.2.1) causes ambiguities at prevent the determination of accurate velocities at such one-dimensional interfaces. A way to circumvent this problem emerged with utilizing *caged fluorescent dyes* for the visualization of the flow (Paul et al., 1998). In its normal state the dye is non-fluorescent because a functional group within the molecule is avoiding its fluorescence property. The excitation of the molecules with light of a certain wavelength allows to disable the functional group and to render the molecules fluorescent. Shadow masks are used to control, which molecules shall become fluorescent and which shall remain non-fluorescent. This way it is possible to produce highly structured fluorescent patterns in the fluid which can be tracked. This technique is commonly known as *Molecular Tagging Velocimetry* (MTV) and further information can be found in general reviews (Koochesfahani and Nocera, 2007) or in the research articles of Gendrich and Koochesfahani (1996) and Koochesfahani (1999).

Figure 4.1 shows two frames of a MTV experiment in a straight micro-channel, which was conducted by Roetmann (2008). Roetmann (2008) kindly provided the whole dataset of MTV micro-channel and micro-mixer images that provided the basis of this work. The experimental setup is well-explained in Roetmann (2008) and the corresponding journal publications (Garbe et al., 2008; Roetmann et al., 2008). However, the important characteristics of the experiment will be mentioned in the following. The channel has a width of 1 mm and depth of 0.2 mm, which produces a velocity profile that differs significantly from the two-dimensional profile (see Appendix A.3). Water was used as

flow medium and enriched with 0.5 g/l of *caged Q-rhodamine dextran* (Gee et al., 2001), which was partially rendered fluorescent by using a dot pattern mask. A given pressure drop causes a motion of $\mathcal{O}(100^{\mu m}/_{sec})$, which advects the fluorescence pattern as it can be seen in the second image of Figure 4.1. The experimental settings lead to Reynolds numbers that range between 0.5 to 5 and the camera was operated at a recording frame rate of 10 Hz. The blurriness of the image pattern increases with elapsed time and is caused by two effects. The first contribution is due to molecular diffusion of the dye molecules and the second is caused by Taylor dispersion (see section 4.3.2).

Concerning the experimental images the boundary conditions of the fluid flow can be assumed to be of *no-slip* type because the Knudsen number is sufficiently small, $\mathrm{Kn} = \mathcal{O}(10^{-4})$. The channel geometry defines the length scale $\ell = \mathcal{O}(10^{-4}m)$ and the free mean path length can be estimated by the average distance between two dye molecules ($\lambda = \mathcal{O}(10^{-8}m)$). The latter value was calculated using the concentration and assuming a homogeneous distribution in the volume. The diameter of the molecules (≈ 10000 Daltons (Gee et al., 2001)) can be neglected, since they are at least one order smaller than the free path length (Haller, 1977).

4.3.2 Taylor dispersion

The dispersion of a molecular species in a fluid is caused by molecular diffusion and velocity gradients that drive molecules apart by locally varying advection velocities. The latter phenomenon was first described and modeled for flows in a tube by Taylor (1953) and Aris (1955). The effect is called *Taylor dispersion* and is illustrated in Figure 4.2. Considering a two-dimensional channel where a solute is compactly located within a solvent at time t_0. The entire fluid is moving laminarly with a steady velocity profile, which distorts the interface between the solute and the fluid. Velocity gradients drive neighboring solute parcels further apart, which can be interpreted as a diffusive process. Therefore, a new diffusion coefficient κ_{tay} was introduced, which accounts of the additional diffusive effect Taylor (1953). The effective diffusion or dispersivity K can be described by

$$K = \kappa + \kappa_{Tay}\,. \tag{4.8}$$

For circular tubes κ_{Tay} depends just on the Péclet number. However, for rectangular shapes, the geometry of the cross section has to be taken into account. Doshi et al. (1978) found that K depends significantly on the ratio of the channel height H and its width W. They found that for $H/W \ll 1$ the dispersivity K is about 8 times larger than the molecular diffusion coefficient κ. A general description for ducts was presented by Chatwin and Sullivan (1982), who found that the longitudinal dispersivity can be expressed as

$$K = \kappa + \frac{1}{210}\frac{(\overline{u}H)^2}{\kappa}\,\mathrm{func}\left(\frac{H}{W}\right)\,, \tag{4.9}$$

where $\overline{u}$ is the mean streamwise velocity in the cross section. The function $\mathrm{func}(\cdot)$ accounts for the specific geometry of the cross section and depends just on the aspect

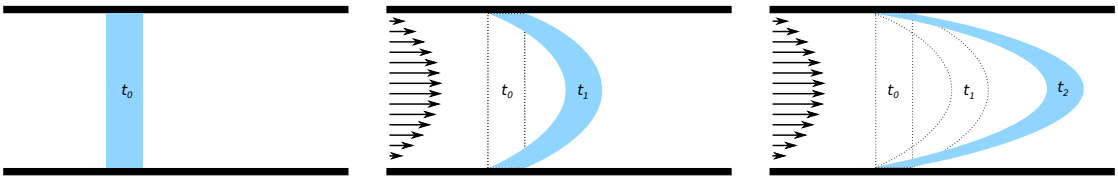

Figure 4.2: This figure illustrates the Taylor dispersion in a two-dimensional channel, which leads to a mixing effect due to locally different advection velocities.

ratio of H and W. The explicit solution for rectangular cross sections can be found in the appendix of Chatwin and Sullivan (1982) and reads

$$K = \frac{1}{4\kappa}\left[2\sum_{\substack{p\ even\\ \geq 2}}\left(\frac{W}{\pi p}\right)^2 W_p^2 + 2\sum_{\substack{q\ even\\ \geq 2}}\left(\frac{H}{\pi q}\right)^2 W_q^2 + \sum_{\substack{p,q\ even\\ \geq 2}}\left\{\frac{W_{pq}^2}{(p\pi/W)^2+(q\pi/H)^2}\right\}\right]$$

$$\text{with}\begin{cases} W_p &= -\frac{32(p_{out}-p_{in})WH^3}{\mu\pi^5}\sum_{n\ odd}\frac{\tanh(n\pi W/2H)}{n^3(n^2W^2+p^2H^2)} \\ W_q &= -\frac{2(p_{out}-p_{in})H^2}{\mu\pi^2q^2}\left\{1+\frac{8}{\pi^2}\sum_{n\ odd}\frac{q^2}{n^2(n^2+q^2)}\frac{\tanh(n\pi W/2H)}{n\pi W/2H}\right\} \\ W_{pq} &= -\frac{32(p_{out}-p_{in})WH^3}{\mu\pi^5}\sum_{n\ odd}\frac{\tanh(n\pi W/2H)}{n(n^2-q^2)}\frac{1}{n^2W^2+p^2H^2} \end{cases} . \tag{4.10}$$

For $H \ll W$ the equations can be simplified by neglecting higher-order terms of Taylor expansions. This yields a linear dependency of the aspect ratio: $K = \kappa(1+A)(1-\mathcal{O}(H/W))$ with $A \approx 6.9512$ being the limit of a series. This approximation is sufficiently accurate for $H/W \leq 0.3$ and therefore can be used for the presented micro-channel experiment. Consequently, an effective dispersion with $K \approx 5.69\kappa$ can be expected.

4.3.3 Modeling the experiment

There are four physical effects that have to be included in the model in order to describe the image sequence properly:

1. Motion model for the duct
2. Fluorescence pattern model
3. Dispersion model
4. Imaging model .

The first part accounts for the solution of the motion equations of the channel flow with a given pressure drop and *no-slip* boundary conditions. For a channel flow the analytical solution was already presented in equation (4.7). The second model deals with the generation of the fluorescent pattern. Because the pattern was generated by a projection of parallel light, it can be assumed that each layer of the volumetric fluorescent pattern looks like the pattern of the mask. The "writing" of the pattern can be modeled as a projection operator $\hat{P}^{\uparrow} : \Omega \to \Omega_3$ that maps the mask pattern into the volume

$$\rho_0 = \hat{P}^{\uparrow} I_0 \,. \tag{4.11}$$

Furthermore, it is assumed that there is sufficient light that the molecules do not occlude the laser light and prevent other molecules to be rendered fluorescent. Another assumption is that the fluorescent molecules are homogeneously distributed along the path and the integral over the height sums up to give the pixels brightness. The third effect is the dispersion of the fluorescent dye molecules. It can be assumed that the dye is homogeneously dissolved in water and making them fluorescent does not effect the molecular diffusion coefficient κ. Therefore, the entire process of dispersion can be described by an advection-diffusion equation of the fluorescent dye density $\rho : \Omega_3 \times T \to \mathbb{R}^+$ with a diffusion constant κ

$$\frac{\partial \rho}{\partial t} + \boldsymbol{u}^T \nabla \rho = \kappa \Delta \rho \,. \tag{4.12}$$

The velocity field is stationary and not coupled to the concentration field. This way it can be treated as a constant motion field. The temporal development of ρ depends on an advective term $\boldsymbol{u}^T \nabla c$ and a diffusive term $\kappa \Delta \rho$. The first term describes implicitly the *Taylor dispersion* and the second term the molecular diffusion. The last step of the modeling deals with the recording of images by projection through an optical system with a telecentric lens. The projection operator $\hat{P}^{\downarrow} : \Omega_3 \to \Omega$ is defined as

$$\hat{P}^{\downarrow} \rho = \int_0^H \rho(\boldsymbol{x}, t) \mathrm{d}z \,. \tag{4.13}$$

Putting all components together the image sequence I_i can be modeled as system of partial differential equations with corresponding boundary conditions and initial state I_0, where the fluorescent pattern was written.

$$I(\boldsymbol{x}, t) = \hat{P}^{\downarrow} \rho + noise \qquad \text{s.t. } \mathcal{C} := \begin{cases} \frac{\partial \rho}{\partial t} &= -\boldsymbol{u}^T \nabla \rho + \kappa \Delta \rho & , \text{in } \Omega_3 \\ \rho &= \hat{P}^{\uparrow} I_0 & , \text{for } t = 0 \\ \rho &= 0 & , \text{on } \Gamma_{wall} \\ \mathbf{0} &= -\boldsymbol{\nabla} p + \frac{1}{\mathrm{Re}} \Delta \boldsymbol{u} & , \text{in } \Omega_3 \\ 0 &= \boldsymbol{\nabla}^T \boldsymbol{u} & , \text{in } \Omega_3 \\ \boldsymbol{u} &= \mathbf{0} & , \text{on } \Gamma_{wall} \\ p &= p_{in} & , \text{on } \Gamma_{in} \\ p &= p_{out} & , \text{on } \Gamma_{out} \end{cases} \tag{4.14}$$

Because the flow is pressure-driven, the boundary conditions at the in- and outlet of $\mathcal{C}$ can be set to the average pressure p_{in} and p_{out} rather than prescribing a velocity profile. This modeling can be justified by the assumption that the channel extends beyond the imaged section to both sides, so that boundary effects of orifices are negligible.

4.3.4 Projected motion equation

Some theoretical considerations of the relationship between real flows and image flows were made by Liu and Shen (2008) for a variety of flow visualization techniques. The advection-diffusion-equation from (4.12) is integrated along the z direction to get the

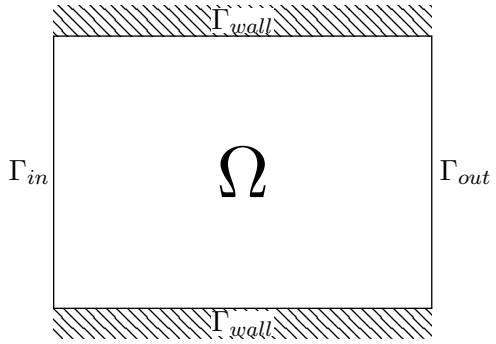

Figure 4.3: Scheme of the computational domain Ω for the micro-channel flow with the corresponding boundary labels.

intensity, which is recorded by the camera (up to a scaling factor). They defined a new velocity variable

$$\langle \boldsymbol{u}_{12} \rangle_\rho = \frac{\int_0^H \rho \boldsymbol{u}_{12} dz}{\int_0^H \rho dz}\,, \tag{4.15}$$

which consists of the first two components of the original velocity field $\boldsymbol{u}$ and are ρ-weighted and z-averaged. It turns out that this new 2D velocity field satisfies a partial differential equation that resembles the original PDE except of some additional boundary integrals that can be neglected because the flow is bounded in z direction by parallel surfaces and the velocity is close to zero at the boundary (*no-slip*). The projected motion equation for the micro-channel reads

$$\partial_t I + \nabla_{12} \cdot (I \langle \boldsymbol{u}_{12} \rangle_\rho) = \kappa \nabla_{12}^2 I\,. \tag{4.16}$$

This equation looks like the extended brightness constancy constraint (see equation (3.10) as it is used for optical flow calculations with an extra diffusive term. In order to estimate the discrepancy between $\langle \boldsymbol{u}_{12} \rangle_\rho$ and the optical flow $\boldsymbol{u}$ it can be assumed that the dye concentration ρ is constant along z. This is certainly true for the very first time steps, where the smallest scale of the intensity pattern is larger than the maximal displacement. Furthermore the z-velocity profile can be assumed nearly parabolic in the center of the channel ($\boldsymbol{u}_{12} = u_{max} \cdot 4z(H-z)H^{-2}$) because of the aspect ratio of the channel. Introducing this into the equation (4.15) yields

$$\langle \boldsymbol{u}_{12} \rangle_\rho = \frac{4u_{max}}{H^3} \int_0^H z(H-z)dz = \frac{2}{3} u_{max}\,. \tag{4.17}$$

This shows that under these circumstances the motion estimates from projections are two thirds of the actual magnitude, if $\rho = const$ along the line of sight. If the displacement of the image pattern exceeds the image structure size, it can happen that just very small z-ranges contribute to the integral. In this case the estimated velocity is the average velocity of the corresponding z-range.

4.3.5 Generation of two-dimensional data

For the purpose of estimating the accuracy of optimal controlled motion estimation using PDE constraints, a set of synthetic images with known characteristics was produced. It is sufficient to use images of two-dimensional flows because the objective is to analyze the effects of image structures onto the motion estimation. The 2D flow is the solution of the Stokes equations and has the form of a parabola in the spanwise direction (Bruus, 2007, p.45)

$$u(\boldsymbol{x}) = \frac{(p_{out} - p_{in})}{2\mu} \left(y^2 - Hy\right) . \tag{4.18}$$

This flow field was used to advect pixel brightness of a given image. The pressure difference controls the magnitude of the parabola and therefore it was set in such a way that the maximal velocity ranged between 0 and 5 pixels. The initial image was generated so that it imitates the real measurement images by image size and image pattern. For this purpose a 10 by 10 dot pattern was produced using an indicator function with an additional Gaussian smoothing step ($G_{3\,\mathrm{px}}$) to remove steep gray value discontinuities. The latter step can be interpreted as modeling the optical blur of lens that is not exactly in focus, which is reasonable due to the imperfection of optical systems.

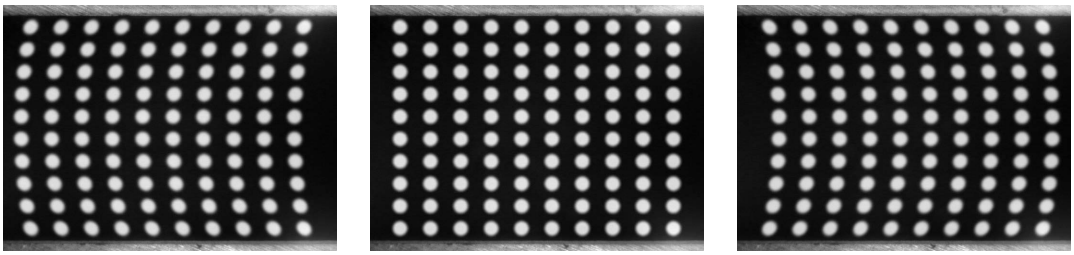

Figure 4.4: This figure shows a pair of synthetic images with a parabolic displacement of maximal 50 pixels (left and right) and the original image from which both images are computed.

An examples image pair is shown in Figure 4.4 where the advection of the initial pattern (center) was applied for $-u/2$ and $+u/2$ to yield the first and second image (left and right image). The usage of symmetric advection is reasoned by the fact that the coordinate transformation requires a brightness value interpolation. Apart from integer displacements all interpolation schemes suffer from slight alterations of the brightness at the individual pixels. To illustrate this circumstance a measurement image was taken and displaced linearly by δx followed by a displacement of $-\delta x$ in order to obtain the original image. Figure 4.5 shows the relative variation of the brightness and its derivative with respect to the displacement. For the generation of the synthetic images there is just one interpolation step necessary, hence the graphs are scaled by $1/2$ assuming a symmetric error. It shows that the average change of a pixel's brightness varies up to 3 %. The alteration is even higher for the gradient of the image with up to 7 % for spline interpolation. Since image gradients are essential for optical flow algorithms, the interpolation error was kept small by applying the half displacement to each image but

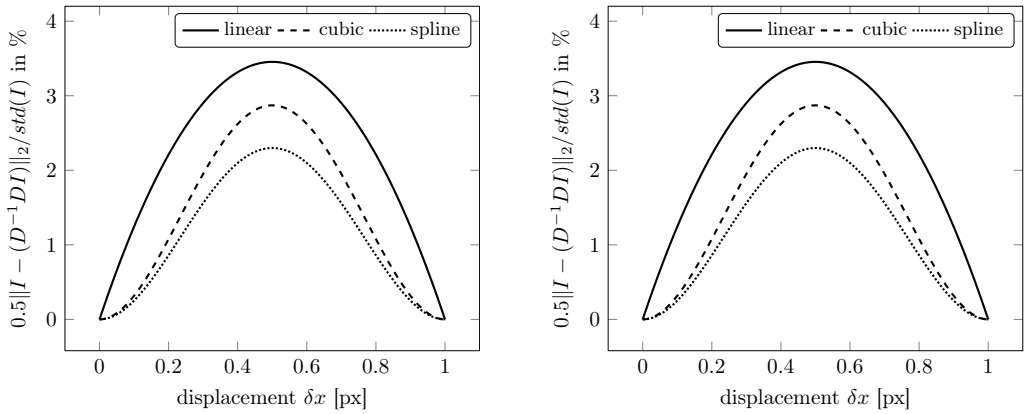

Figure 4.5: These two figures illustrate the induced error for linear, cubic and spline interpolation of an image depending on the displacement δx. The left graph shows the standard deviation of the relative change of the image intensity, while the right graph shows the same for the its x-derivative.

in opposite directions. This way both images are experience the same smoothing effect of the interpolation.

A second set of synthetic images was produced where the background noise of the authentic images was added to mimic real measurement images. Here, the signal-to-noise ratio (SNR) is defined as the magnitude of the indicator function divided by the standard deviation of the background noise. This parameter was set to values ranging from 1 to 300, which yields images with rugged brightness profiles up to very smooth profiles. Figure 4.6 shows a profile of one individual dot of the pattern for a varying SNR value. The last profile was taken from an authentic measurement image and is included for reasons of comparison. However, it reveals that the noise rate is dependent on the intensity. The background noise has a standard deviation of 2.6 brightness units while the fluorescent pattern (assuming top-hat shape) has a standard deviation of around 12 brightness units that is almost 5 times larger. The two noise levels are weighted with their occurrence (area) in order to determine a single value of 4.1 brightness units. This yields to a SNR of about 70, given the average magnitude of 300 brightness units for the top-hat pattern.

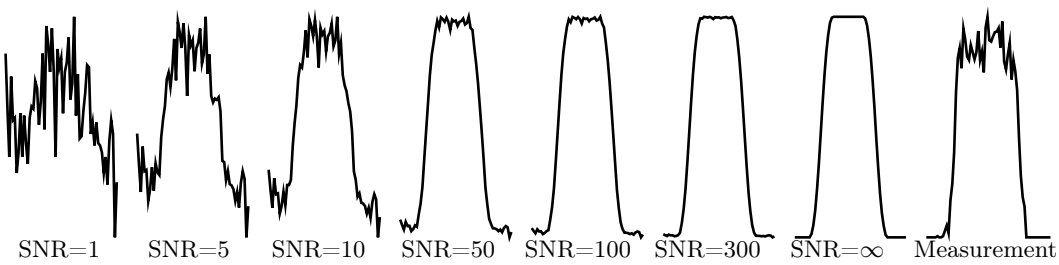

Figure 4.6: These profiles illustrate the cross sections of the pattern for different SNR. A measurement profile is show for comparison at the very right.

4.3.6 Deficiencies of methods without global motion model

In this section the standard motion estimation algorithms are applied to the microchannel images that compare to the images in figure 4.1. The lack of global motion models will turn out to be a serious disadvantage for the evaluation of data that has just sparsely distributed information which is spread over the entire image. Local motion models are not capable to overcome image regions that contain no processable information because the motion model is to flexible so that actual motion information from other parts has too little influence. In order to point out the deficiencies of local motion models, a synthetic image pair ($u_{max} = 1\,\mathrm{px}/\delta t$) is taken and processed by a state-of-the-atr correlation method[1] and optical flow method[2].

4.3.6.1 Correlation approach

Patch matching techniques have intrinsically the drawback that they estimate an average velocity for an entire image part. As a consequence, the spatial resolution is reduced and depends on the size of the interrogation window. By using a special weighting function w and overlapping patches it is possible to achieve higher resolutions (Astarita, 2006). Nevertheless, pixel resolution can just be obtained by a very expensive computation, since for each pixel all the neighboring pixels have to be taken into accounted. This can increase the number of pixels to be processed by a factor of 100 to 1000. Usually this computational effort is too large, so that the velocity field is not estimated densely but with a spacing of 4 pixels in each dimension. Another disadvantage of the spatial averaging is that complex motions below the size of the interrogation window cannot be estimated. The user has to make a trade-off between spatial resolution of the solution and the accuracy.

With respect to the evaluation of MTV images like the ones shown in figure 4.1 the choice of adequate user parameters is not too straight forward. The initial interrogation window has to be set in such a way that the velocity gradients can be resolved sufficiently accurate but also it has to be large enough to contain information. The symmetry of this experiment allows to use interrogation windows that extend further into the streamwise direction than to the spanwise direction. The following multilevel interrogation scheme was used: $96 \times 64\,\mathrm{px} \rightarrow 64 \times 48\,\mathrm{px} \rightarrow 32 \times 32\,\mathrm{px}$. A quadratic interrogation window was chosen to avoid numerical artifacts for the final evaluation step of this hierarchical scheme.

The results are shown in figure 4.7 for four different choices of final interrogation windows. Since the velocity estimates are computed at the nodes of a uniform grid, it occurs that some of the images patches contain just noise, especially if the IW is very small. This is clearly visible for a 8×8 pixels IW. There are many wrong estimates that corrupt the general shape of the velocity profile. If the size of the final IW is set to larger values, this effect is reduced and the motion field becomes smoother. However, the motion field shows ripples that appear for the largest IW sizes. This effect is caused by aliasing since the spatial frequency of the image pattern does not combine with the IW size. Since the images contain just the pattern and no background, the motion field

[1] PIV software Widim that uses a multiple scales and a image deformation approach (Scarano and Riethmuller, 1999).

[2] Optical flow code by Liu (2009), which based on the publications of Brox et al. (2004) and Bruhn et al. (2005)

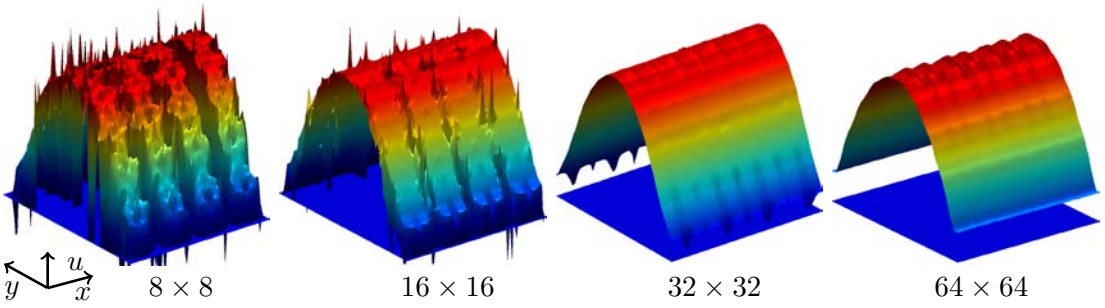

Figure 4.7: This figure shows the results of correlation based techniques when applied to microfluid MTV images. The interrogation window size is gradually increased from 8×8 px to 64×64 px in order to show the averaging effect.

extends up the image borders since the channel borders are not visible. A velocity of zero at the channel border can not be estimated because motion information propagates from the inner channel to the borders. However, the larger the IW gets, the more information is averaged and consequently the profile gets flattened. The largest IW with a size of 64×64 pixels corresponds to almost one seventh of the entire channel width.

4.3.6.2 Optical flow approach

The very same images were process with optical flow for three different regularization parameters α. Figure 4.8 shows the results that reveal a significant influence of the image pattern. Motion information is only provided at the dots of the pattern and at the positions in between the motion is smoothly interpolated. The steepest image gradients have a largest impact on the estimated motion field and cause the circular velocity patterns. For small regularization parameters ($\alpha = 0.01$) the motion is too close to the image data and consequently not smooth at all. With increasing α the extreme motion peaks become regularized and adapt to the magnitude of the surrounding estimates.

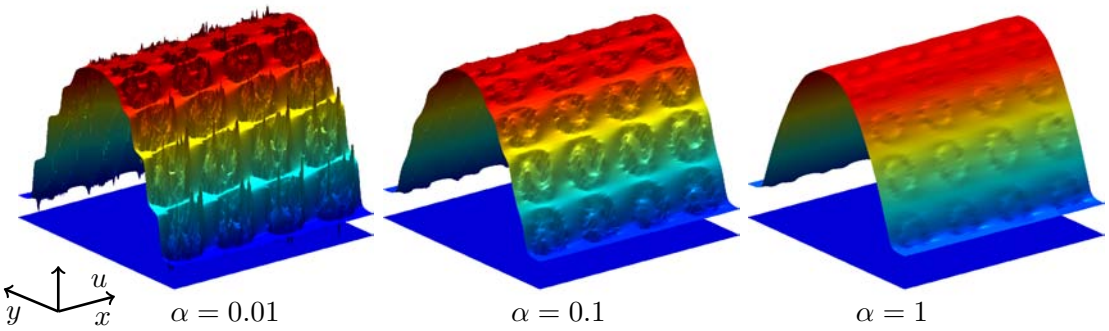

Figure 4.8: This figure shows the results of Horn & Schunck optical flow if applied to microfluid MTV images. The outcome was tested for several regularization parameters α. Shown are the results for $\alpha = 0.01$, $\alpha = 0.1$ and $\alpha = 1$.

4.3.7 PDE constrained approach

This section will demonstrate the advantages of global motion models that allow to overcome the difficulties of the methods without global motion model. The Stokes equations will be included as constraints into the solution finding process. Two types of controls will be used: a distributed control of the boundary condition and a parameter control of the average pressure at the flow inlet. Both types can be computed by the optimal control framework RoDoBo in combination with Gascoigne. Both approaches are compared to each other by evaluating the synthetic two-dimensional image sequence, which allows to assess the accuracy.

4.3.7.1 Velocity control

In order to maintain the generality of this approach the solution $(\boldsymbol{u}^*, p^*)$ is assumed to be unknown and has to be determined in such a way that it minimizes a given cost functional J. The cost functional consists of the usual brightness constancy constraint from equation (3.10) and some costs of the control q that are weighted by the parameter $\alpha > 0$. The constraint equations are the Stokes equations with *no-slip* boundary condition at the walls $\boldsymbol{u}\big|_{\Gamma_{wall}} = \mathbf{0}$ and controls q_{in} and q_{out} as streamwise component of $\boldsymbol{u}$ at the inlet Γ_{in} and outlet Γ_{out}, respectively. The spanwise component is set to be zero. Without loss of generality the average pressure in Ω is set to zero since just the derivatives of the pressure enter the state equation. The constrained minimization problem reads

$$
\begin{aligned}
J(u,q) &= \frac{1}{2}\|\partial_t I + \boldsymbol{u}^T \nabla I\|_\Omega^2 + \frac{\alpha}{2}\|q_{in}\|_{\Gamma_{in}}^2 + \frac{\alpha}{2}\|q_{out}\|_{\Gamma_{out}}^2 \\
\min_q J(\boldsymbol{u},q) \qquad \text{s.t.} &\begin{cases} 0 = \frac{1}{\mathrm{Re}}\Delta\boldsymbol{u} - \nabla p & ,\text{in } \Omega \\ 0 = \nabla^T \boldsymbol{u} & ,\text{in } \Omega \\ \boldsymbol{u} = 0 & ,\text{on } \Gamma_{wall} \\ \boldsymbol{u} = (q_{in}, 0)^T & ,\text{on } \Gamma_{in} \\ \boldsymbol{u} = (q_{out}, 0)^T & ,\text{on } \Gamma_{out} \end{cases} .
\end{aligned} \tag{4.19}
$$

With the notation $H := H_0^1(\Omega, \partial\Omega)$ and $L = L_0^2(\Omega) := \{q \in L^2(\Omega), \int_\Omega q \mathrm{d}x = 0\}$ the variational formulation for (4.19) can be reformulated as finding $\boldsymbol{u} \in (q_{in}, 0)^T\big|_{\Gamma_{in}} + (q_{out}, 0)^T\big|_{\Gamma_{out}} + H$ and $p \in L$ that minimizes

$$
J(\boldsymbol{u},q) = \frac{1}{2}\|\partial_t I + \boldsymbol{u}^T \nabla I\|_\Omega^2 + \frac{\alpha}{2}\|q_{in}\|_{\Gamma_{in}}^2 + \frac{\alpha}{2}\|q_{out}\|_{\Gamma_{out}}^2 \tag{4.20}
$$

and satisfies

$$
0 = \frac{1}{\mathrm{Re}}\left(\nabla\boldsymbol{u}, \nabla\phi\right) - \left(p, \operatorname{div}\phi\right) + \left(\operatorname{div}\boldsymbol{u}, \chi\right) \quad ,\forall(\phi,\chi) \in H \times L\,. \tag{4.21}
$$

The optimal solution $(\boldsymbol{u}^*, p^*, q_{in}^*, q_{out}^*)$ can be found by using the optimal control method, which was introduced in section 2.5 in combination with finite elements to solve the system of PDEs. In agreement with the experimental settings, the Reynolds number was chosen to be one.

Choosing the regularization parameter α

Similar to optical flow, the regularization affects not just the solution of the state equation but also the value of the cost functional. The parameter α has to be chosen in such a way that the control becomes not too irregular (non-smooth) and does not contribute too much to the total cost J. A L^2-penalization was chosen, that tries to limit the magnitude of the control. In order to test the effect of α, a noise-free synthetic image pair with a maximal displacement of $u_{max} = 1$ px at the center of the parabola was taken and evaluated for a range of α parameters. In order to illustrate the influence onto the solution figure (4.9) shows the results of six different α parameters. For small α's the control is not smooth and oscillates around its true profile. The oscillations stem from the intensity pattern in the images (see Appendix A.7). By virtue of the BCCE all image gradients generate motion (see equation (3.10)). However, the vertical gradients do not originate form a motion but from the shearing that is caused by different velocities in the streamwise direction. This issue was already introduced and discussed as *aperture problem* on page 28 and leads to the definition of *normal* flow. Between the dot pattern there is no image information that prevents vertical motion. Hence, the velocity controls at the openings are free to adapt until the vertical gradients lead to a vertical motion or the induced control costs contribute significantly to the total costs J.

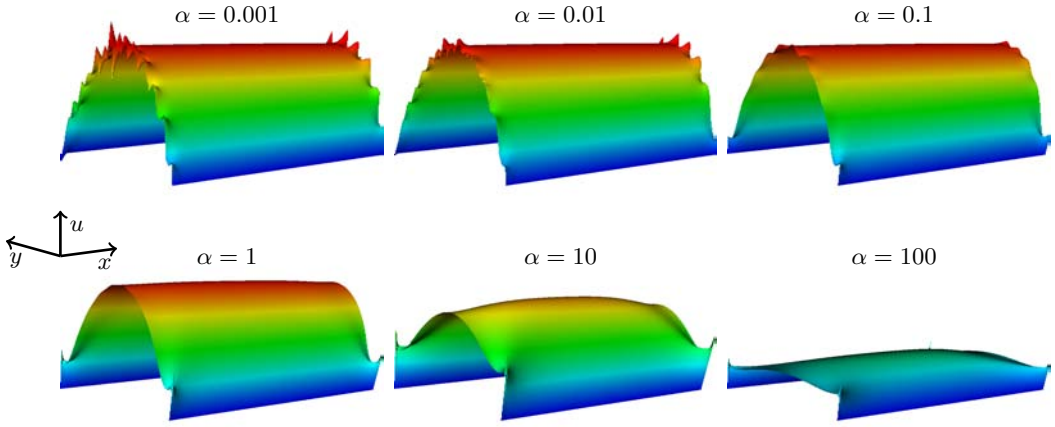

Figure 4.9: This figure shows the parabolic u-profiles for differently weighted $L^2(\Gamma_{in})$-costs of the control $\boldsymbol{q}$.

However, towards the center of the channel the oscillations level off quickly due to the rigid nature of the Stokes equations and because motion information from all directions contribute. At the openings of the channel there is just information towards the two inward directions of the channel. Consequently, a perfect parabolic profile is computed at the center of the channel where border effects are negligible.

The oscillations of the controls can be reduced by increasing α and consequently the costs of the controls. With larger α the swinging of the profile lessens and it becomes smoother. The parameter α balances the costs of the data term and the control. The larger α is, the less significant becomes the image data and the result can deviate very much from the expected result (e.g. $\alpha = 100$). Penalizing the magnitude of the control improves the result just to a certain value of α where large oscillations corrupt the result.

Beyond that value the cost of the ground truth velocity parabola is of the same order as the data costs. Further increase of α leads to a reduced magnitude of the velocity profile at the openings. Another effect of the L^2-penalization becomes apparent for $\alpha \geq 0.1$. For a constant mass flow through a channel, the lowest control costs can be achieved by a constant inflow velocity and not a parabola. This can be seen for $\alpha = 100$, where the inlet velocity resembles a boxcar function. For αs around unity this effect is less obvious but still present. The magnitude of the profiles is reduced and the additional mass flow is injected through two side lobes close to the border. With respect to the control costs this bypass is "cheaper" because the spatial image gradients close to the wall are very small and do not contribute significantly to J.

It has to be mentioned that the controls q_{in} and q_{out} are not exactly equal. The reason is the distinct motion direction from the left to the right and the fact that image pattern is closer to Γ_{out} than to Γ_{in}. As a result the influence of the gradients is not the same for both openings. Especially for very small α's both controls are distinguishable but still they have the same magnitude. For larger α's the data becomes less important and so the controls become almost identical.

In order to find the "best" α, the difference of the estimated solution $\boldsymbol{u}$ and the reference solution $\boldsymbol{u}_{ref}$ is measured with the $L^1(\Omega)$ and $L^2(\Omega)$-norms and normalized by $u_{max} = \|\boldsymbol{u}_{ref}\|_\infty$. Using the L^1-norm becomes reasonable because large errors occur mostly at the near region of the inlet where the control is set. The L^2-norm treats these errors quadratically and is dominated by them although the solution $\boldsymbol{u}$ in the remaining part of Ω has a small error. This will become more obvious when applying the inflow control approach to noisy images (see A.3 for comparison).

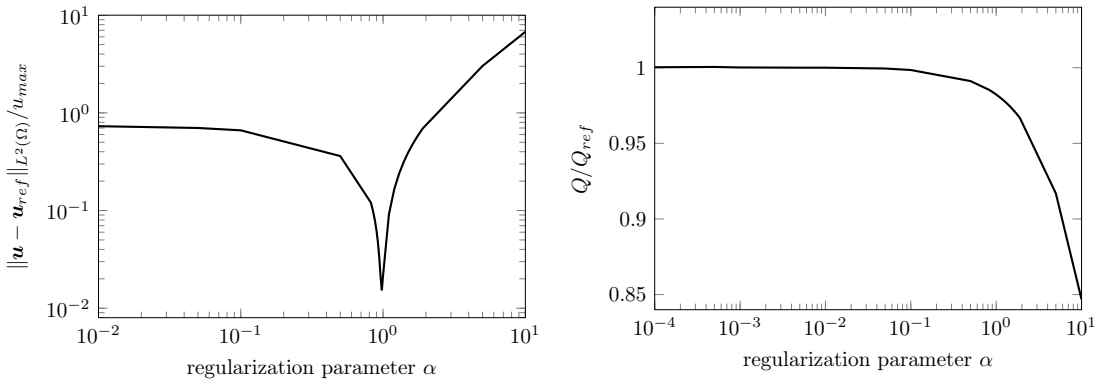

Figure 4.10: The left plot shows the α dependency of the L^2-error with respect to the reference solution of two images with a dot pattern and a maximal displacement of 1 pixel in the center of the parabola. The right plot shows the ratio of the estimated flow rate Q to the reference flow rate Q_{ref} on the basis of two images with a dot pattern and a maximal displacement of 1 pixel.

Figure 4.10 shows the α dependency on the accuracy of the entire solution in Ω. The optimal value that gives the lowest error is close to unity. For $\alpha < 1$ the error increases due to the irregular inflow profile, which is caused by the lack of image information while on the other hand the general profile resembles closely the reference parabola. For $\alpha > 1$ the error increases drastically because the control costs make up a significant portion of

the entire cost. The control becomes more important than the actual solution and the error raises.

In order to illustrate that the irregular effects at the openings are caused by a shortage of data, figure 4.10 shows the flow rate $Q = \int_{\Gamma_{out}} \boldsymbol{u} \mathrm{d}\boldsymbol{x} / \int_{\Gamma_{out}} \mathrm{d}\boldsymbol{x}$ through a cross section normalized by the reference flow rate Q_{ref}. It reveals that the estimated flux is quite accurate for a wide range of small αs, where the estimated value is just 0.3 % larger. The slightly higher estimated value is due to the fact that also the vertical image gradients contribute to the motion, e.g. *normal flow*. The additionally estimated motion leads to the small overestimation of the flow rate Q. Similar to the L^2-error the flow rate error increases rapidly for $\alpha > 1$. For the following investigations concerning the inflow control, the apparently "best" choice of $\alpha = 1$ is used, which gave very low errors for $\boldsymbol{u}$ and still good results for Q.

Dependency on the displacement

Using the *brightness constancy constraint equation* (BCCE) involves a Taylor approximation of first-order. For this reason the proposed approach is very likely to fail for large displacements $u_{max} \gg 1\,\mathrm{px}$. This shortcoming of the BCCE is already well-known and usually circumvented by hierarchical or scaling schemes. However, the accuracy of the solution depends on the smoothness of the image pattern but also on the used motion model. Global motion models can compensate for missing or erroneous local estimates if they occur not to often. At first the approach was applied to noiseless images with maximal displacements that range between $0.1\,\mathrm{px}/\delta t$ and $5\,\mathrm{px}/\delta t$.

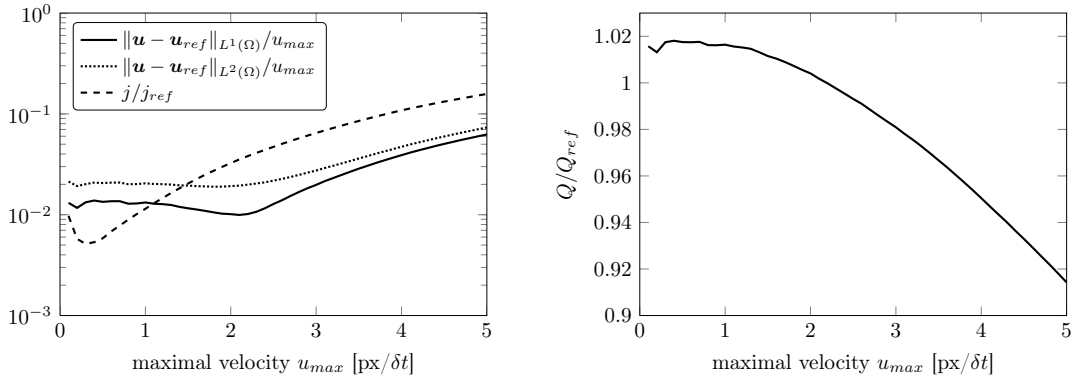

Figure 4.11: These figures show the normalized L^1- and L^2-errors of the estimated velocity $\boldsymbol{u}$, the corresponding normalized cost functional value j and the ratio between the estimated flow rate Q and the reference flow rate Q_{ref} for $\alpha = 1$.

Figure 4.11 illustrates the evolution of the error with increasing u_{max}. Not surprisingly, both errors are very low for small displacements and grow with increasing u_{max}. The two norms differ by a factor of up to two for $u_{max} < 2.5\,\mathrm{px}/\delta t$. This comes from the oscillations at the in- and outlet. The L^2-norm is optimal for Gaussian noise (see A.4) and therefore not the best choice for estimating the quality of the result that contains non-Gaussian outliers. The L^1-norm is much more appropriate to deal with the few "outliers" that are located near the boundaries Γ_{in} and Γ_{out}. Moreover, the normalized costs for

the estimated $\boldsymbol{u}$ are displayed in the left graph of figure 4.11. They are normalized with the reference cost j_{ref}, which is computed for zero velocity $\boldsymbol{u} = 0\,\mathrm{px}/\delta t$. It reveals that for $u_{max} \approx 0.4\,\mathrm{px}/\delta t$ the relative costs are the lowest, about 0.4 % of the initial costs. The reference flow rate j_{ref} decreases gradually while approaching $u_{max} = 0\,\mathrm{px}/\delta t$, hence the relative cost increase in the vicinity of zero because of the small overestimation of j that is associated with the *normal flow*. This effect cannot be seen in the velocity graph because the oscillations are much more significant for the velocity as for the flow rate. The costs increase to the right of the minimum because of a growing costs of the controls and larger errors due to the insufficient representation of the data by the first-order Taylor approximation.

The second graph in figure 4.11 shows the ratio between the estimated flow rate Q and the reference flow rate Q_{ref}. It is overestimated by 2.5 % for small displacements and decreases with growing u_{max}. The overestimation originates from the highly adapted motion towards the data, where any image gradient ∇I contributes equally to the motion (especially $\partial_y I$). The continuity equation requires additional inflow to compensate these gradients, which leads to the overestimation (see Appendix A.8). Larger displacements cause additional cost on the control and lead also to a decreased flow rate.

In order to investigate the dependency on the noise level, the noise corrupted images were processed for the same displacement range as before. Figure 4.12 shows contour lines indicating the accuracy levels with varying noise and maximal velocity. It draws a similar picture as the noise-free dependency in figure 4.11. There is a minimum near $\boldsymbol{u}_{max} = 3\,\mathrm{px}/\delta t$, which appears to be rather independent of the noise level. Of course, for far too much noise the accuracy drops rapidly (noise level < 25). The flow rate graph on the right of the very same figure reveals that the mass flow is overestimated for $u_{max} < 3\,\mathrm{px}/\delta t$ and underestimated beyond it. The value of the exact estimation of the flow rate shifts from around $2\,\mathrm{px}/\delta t$ in the noise-free images to circa $3\,\mathrm{px}/\delta t$ for noisy images. The flow rate graph allows to understand the velocity graph and explains why the error is also large for small u_{max}. It is originated in the overestimation of the velocity, which cannot be seen by plotting the norm of the residual.

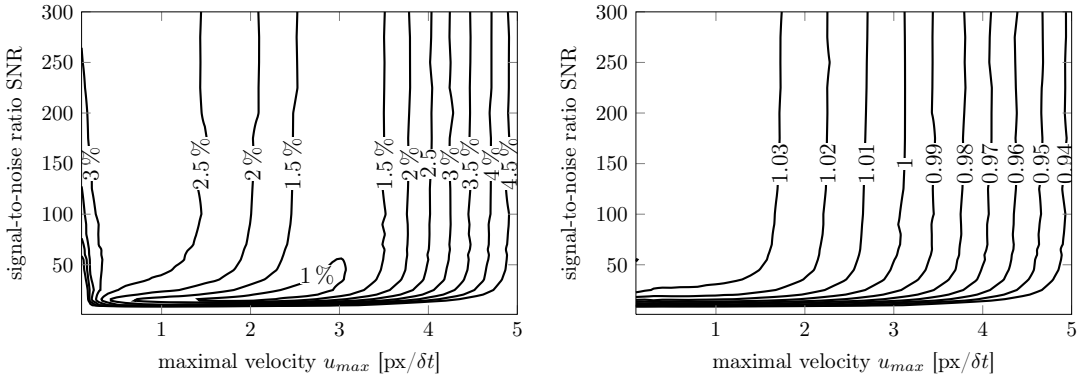

Figure 4.12: These graphs show the contour lines of the normalized error $\|\boldsymbol{u} - \boldsymbol{u}_{ref}\|_1/u_{max}$ error (left) and the ratio of the estimated to the reference flow rate Q/Q_{ref} (right), respectively.

Estimating wall-slip

In section 4.2 it was pointed out that the assumption of a *no-slip* boundary condition might not be appropriate for all microfluidic applications. The reason is the failure of the continuity assumption. Another reason for allowing a finite wall-slip is the inaccurate knowledge domain Ω. If the boundary $\partial\Omega$ of the fluid domain is **not** known precisely then the *no-slip* condition would be ill-suited and induce additional errors (Silva et al., 2009). These two cases motivate to extend the optimal control $\boldsymbol{q}$ and to include also the wall-boundaries of the domain. For such a case the problem reads

$$J(u,q) = \frac{1}{2}\|\partial_t I + \boldsymbol{u}^T\nabla I\|_\Omega^2 + \frac{\alpha}{2}\|q\|_{\partial\Omega}^2$$
$$\min_q J(\boldsymbol{u},q) \quad \text{s.t.} \begin{cases} 0 = \frac{1}{\mathrm{Re}}\Delta\boldsymbol{u} - \nabla p & ,\text{in } \Omega \\ 0 = \nabla^T\boldsymbol{u} & ,\text{in } \Omega \\ \boldsymbol{u} = (q,0)^T & ,\text{on } \partial\Omega \end{cases} . \tag{4.22}$$

Here, it is assumed that v is zero and just the streamwise velocity is estimated. This approach was tested with two synthetic images containing a regular grid pattern (see Appendix A.7) with $u_{max} = 1$ and $\alpha = 1$. The u-solution is shown in figure 4.13 with the emphasis on the wall-slip velocity. Using this boundary control approach shows that the wall velocity u_{wall} is constantly underestimated by nearly 2 %. This corresponds exactly to the error of the overestimated flow rate. The variations of the wall velocity stem from the subscribed image pattern. This becomes more obvious during the next investigation, where a constant wall velocity is prescribed and has to be recovered by this approach. A constant offset velocity ranging from 0 px to 1 px was added to the reference velocity

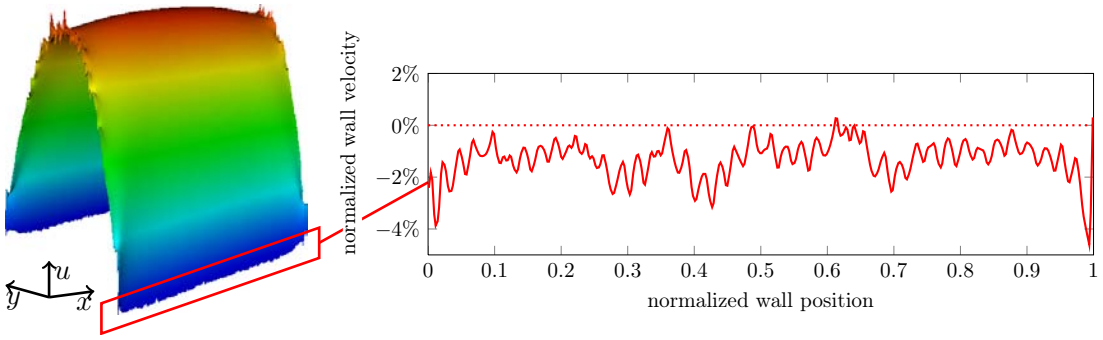

Figure 4.13: This figure shows the result of the u-component of the boundary control problem from equation (4.22). The graph reveals the fine structure that can not be seen in the color plot.

field ($u_{max} = 1\,\mathrm{px}/\delta t$), which was then used to produce the synthetic images with a regular grid pattern. Exactly this grid pattern of 40 grid lines can be seen in all 20 normalized wall velocity profiles $(u/u_{wall})\big|_{\Gamma_{wall}}$ in figure 4.14. They match so closely, that just a single line is observable. The immense drop to both ends of the profile is caused by a reduced influence of the regularization because the image provides only information from 2 directions in the image corner. The shear induced spanwise gradients contribute significantly to the motion and lower the streamwise velocity estimate considerably. The

averaged wall velocity was computed with respect to the data in the range $x \in [0.1, 0.9]$ in order to leave out the edge disturbances. The right graph of figure 4.13 reveals that u_{wall} gets slightly overestimated. For $u_{wall} = 1\,\mathrm{px}/\delta t$ this happens to be up to 10 %, which tends to zero for $u_{wall} \to 0$. However, it can be clearly seen that the overestimation is systematic because the dependency of the estimates is linear with a slightly larger slope. Considering the large error of wall-slip estimates of up to 45 % from other image processing approaches (Joseph and Tabeling, 2005), the estimation by the presented approach seems quite good, especially for small u_{wall}.

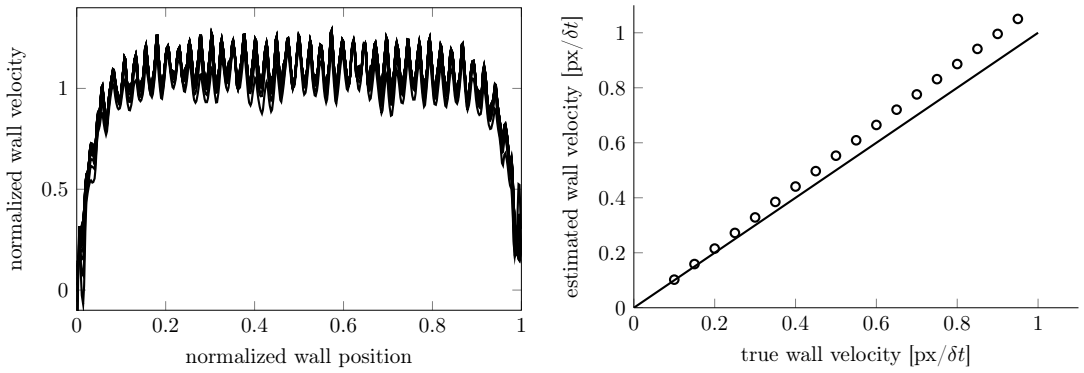

Figure 4.14: This left figure shows the normalized wall velocities profiles for wall velocities ranging from 0 to 1 pixel. The right figure depicts the average wall velocity u_{wall} along the boundary disregarding the data close to the openings. The correct dependency is shown as a solid line for comparison.

In order to investigate the influence of the image data, this method has to be applied to many different images that share the same global characteristics and containing exactly the same image motion. This allows to compute statistical moments of the boundary functions in order to cancel out the effects of the individual image pattern. For this purpose, a set of randomly structured images were produced (Fieguth, 2010, Example 8.3) that are independent samples but have the same spatial correlation length. A set of 100 image samples was produced to calculate the mean and the variance of a flow with zero wall-velocity and $u_{max} = 0.5\,\mathrm{px}/\delta t$. Figure 4.15 shows one of these images. The plot to the right shows the estimated average wall-slip profile together with the standard deviation. It reveals that it is constantly underestimated by (1 ± 1) % of the maximal velocity u_{max}. The deviation reduces towards the domain borders and yields even overestimated wall-velocities. The reason is the L^2-penalization of the inlet boundary function, which produces side lobes at the inlet profile to reduce the costs. This leads to a propagation of the overestimated inlet velocity towards the edges of the domain. Since the flow rate is overestimated by 2 %-3 % (see figure 4.12), the boundary control function compensates the overestimation by 1 %. The image data limits the underestimation of u_{wall} by increasing costs of the data term. Some other quantities could be determined from this set of images. The average deviation of the flow rate is 0.3 %, while the cost functional j varies up to 2.75 %.

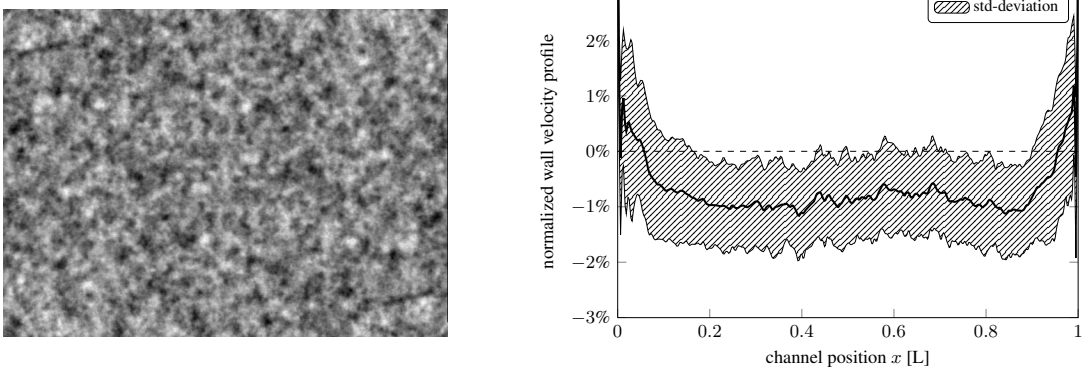

Figure 4.15: The left image shows a sample image which contains a random sample. The right graph depicts the estimated average normalized wall-velocity with its standard deviation.

4.3.7.2 Pressure control

The previously discussed velocity control has the drawback that it adapts to much to the data which causes the oscillations of the boundary control. The micro-channel flow is a purely pressure-driven flow, which means that it is fully determined by the just knowing the pressure difference between the inlet and outlet (assuming *no-slip* wall condition). Instead of estimating the entire velocity profiles at the openings, the degrees of freedom can be reduced to estimate just one parameter, the pressure drop $\delta p = p_{out} - p_{in}$. This is possible because the flow in the experiment was driven by hydrostatic pressure difference and not by the injection of fluid stream. Consequently, the velocity profile in two dimensions has to be parabolic throughout the entire domain, in particular at the openings too. The optimal control problem can be converted to a parameter estimation problem with PDE constraints

$$\min_q \frac{1}{2}\|\partial_t I + \boldsymbol{u}^T \nabla I\|_\Omega^2 \qquad \text{s.t.} \begin{cases} \mathbf{0} &= \frac{1}{\mathrm{Re}}\Delta \boldsymbol{u} - \nabla p & ,\text{in } \Omega \\ 0 &= \nabla^T \boldsymbol{u} & ,\text{in } \Omega \\ \boldsymbol{u} &= \mathbf{0} & ,\text{on } \Gamma_{wall} \\ p &= 0 & ,\text{on } \Gamma_{in} \\ \boldsymbol{n}q &= \frac{1}{\mathrm{Re}}\partial_n \boldsymbol{u} - \boldsymbol{n}p & ,\text{on } \Gamma_{out} \end{cases} . \tag{4.23}$$

Without the loss of generality the pressure at the inlet boundary can be set to zero. The constraint $\frac{1}{\mathrm{Re}}\partial_n \boldsymbol{u} - \boldsymbol{n}p = 0$ is known as natural boundary condition or "do-nothing" condition because it appears naturally in the variational formulation if no boundary condition is prescribed (Heywood et al., 1996; Rannacher, 2000). The parameter q represents the average pressure over the boundary of the opening $\langle p \rangle_{\Gamma_{out}}$. The variational formulation of this problem reads

$$\min_q \frac{1}{2}\|\partial_t I + \boldsymbol{u}^T \nabla I\|_\Omega^2$$
$$\text{s.t.} \quad \begin{cases} 0 &= \frac{1}{\mathrm{Re}}(\nabla \boldsymbol{u}, \nabla \phi) - (p, \operatorname{div} \phi) - (q, \phi)_{\Gamma_{in}} &, \forall \phi \in H_0^1(\Omega, \Gamma_{wall}) \\ 0 &= (\operatorname{div} \boldsymbol{u}, \chi) &, \forall \chi L^2(\Omega) \end{cases} . \tag{4.24}$$

The control parameter does not need any additional penalization with the cost functional J since it is just one value. Consequently, there is no regularization parameter α necessary. Figure 4.16 shows the three components of the estimated solution (u^*, v^*, p^*). The streamwise component u is of perfect parabola shape while the spanwise component v is zero and the pressure shows a linear trend between the openings.

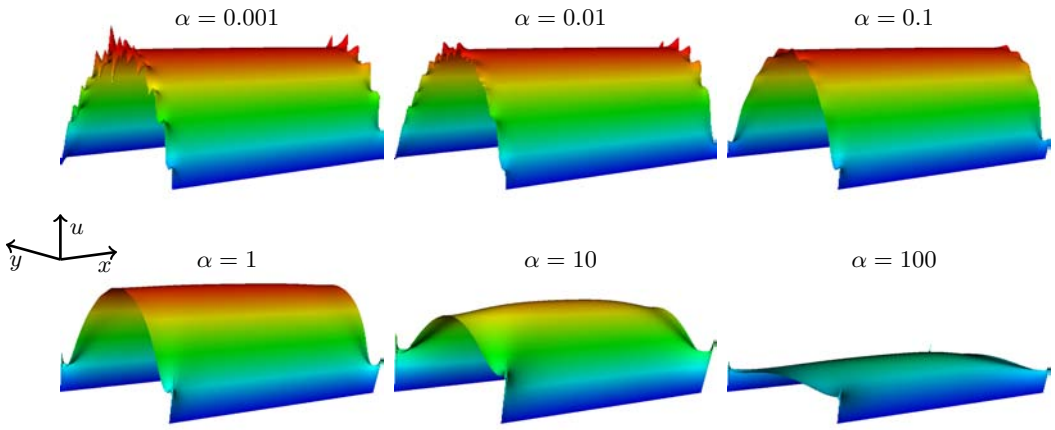

Figure 4.16: This graph shows qualitatively the representative results of (u, v, p) in case of the pressure control method. The streamwise component has the ideal parabola shape, the spanwise component is zero and the pressure grows linearly.

In order to assess the accuracy, the same images were analyzed as it was done for the velocity controlled approach. An important benefit of this approach is the lack of user defined parameters, such as the regularizing parameter α. Pressure control estimation does not need any special regularization of parameters as distributed controls, just the images and the constraint equations with boundary conditions. Figure 4.17 shows the normalized residuals of the velocity estimate $\boldsymbol{u}$ with respect to the reference solution $\boldsymbol{u}_{ref}$, the normalized cost functional and the normalized flow rate. The first aspect that becomes apparent is the remarkable similarity of the estimated flow rate to the flow rate from the velocity control approach, just with a constant offset of about 1 % (see Figure 4.11). The offset comes from the side lobes of the estimated velocity control, that lowers the flow rate. The overestimation is also caused by the aperture problem and the normal flow that contributes to the estimates.

The relative errors are shown at the left plot of Figure 4.17 and reveal a similar trend compared to the velocity control results, but have an almost one order smaller magnitude. This confirms the previous assumption, that the velocity error at small u_{max} for the in- and outlet boundary control is mainly caused by the oscillations at the borders. For the average pressure control the velocity error for noiseless images is below

0.5 % for $u_{max} < 1.5\,\mathrm{px}/\delta t$. The L^2-error reaches its lowest value for the displacement of at $1.2\,\mathrm{px}/\delta t$ where the overestimation of the flux cancels out with the error due to the Taylor approximation in the brightness constancy constraint (see 3.10). The small kink at $0.2\,\mathrm{px}/\delta t$ is probably due to disadvantageous combination of image-grid interpolation, since the grid and the pixel locations do not coincide accurately.

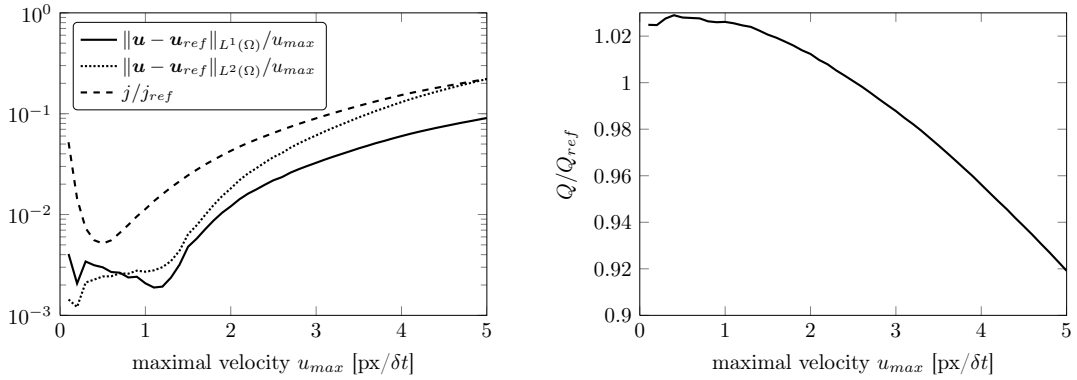

Figure 4.17: The left graph shows the normalized L^1 and L^2-errors of the velocity field together with the normalized cost functional j/j_{ref} for noisefree images. The right graph displays the corresponding estimated momentum flux.

The dependency of the error with respect to the noise level and the displacement is shown in Figure 4.18. It can be seen that this approach yields errors below 1 % for a wide range of velocities ($u_{max} = 0\,\mathrm{pixels}/\delta t \ldots 1.5\,\mathrm{pixels}/\delta t$) and noise levels (60 to ∞). Noise becomes significant for noise levels below 50. From this point on, the signal looses its dominance and the error increases rapidly. At a given noise level the error grows rather slowly for increasing u_{max}. This effect cannot be assessed accurately because the velocity profile is a parabola with the whole range of displacements between zero and u_{max}. The lowest error occurs for displacements close to unity. The small bubble-like area in the top left corner of the graph is caused by the image interpolation error of the synthetic images, that has been already addressed to on page 44. The interpolation error is the largest for displacements of $1/2$ pixels and has obviously also effects on the motion estimation. For increasing noise, this effect levels off. The right graph of figure 4.18 shows the ratio between the reference Q_{ref} and the estimated momentum flux Q. The trend of the error with respect to the displacement and the SNR equals the graph from the velocity error. It can be seen, that the image interpolation error leads to slightly larger motion estimates. This comes from the different interpolation errors of the brightness and the its gradients (see figure 4.5). The temporal gradient $\partial_t I$ is based on the brightness and ∇I is based on the gradient of the brightness.

Stability of the estimates

Reasonable estimates of physical quantities should hardly change if the data is slightly altered in order to be meaningful. Besides the robustness and speed of the parameter estimation, it is feasible to calculate the second-order derivatives j''_{qq} explicitly. The Hessian can be used to tell whether the parameter q^* is a "deep" or "shallow" minimum,

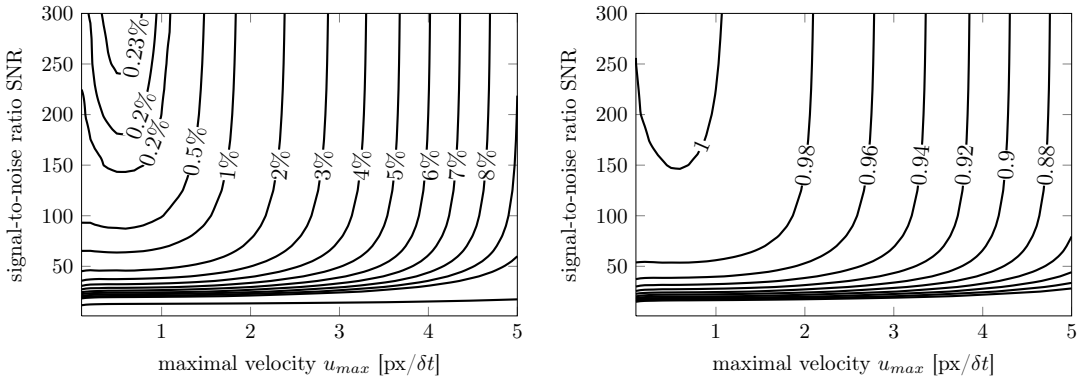

Figure 4.18: These graphs show the contour lines of the normalized error $\|\boldsymbol{u} - \boldsymbol{u}_{ref}\|_1/u_{max}$ error (left) and the ratio of the estimated to the reference flux Q/Q_{ref} (right), respectively.

whether it is stable or close to indifferent. At the minimum the reduced cost function can be approximated by

$$j(q) \approx j(q^*) + \frac{1}{2}(q - q^*)^T \boldsymbol{H}(q - q^*)\,, \tag{4.25}$$

where $\boldsymbol{H}$ is the hessian of j at the optimal control q^*. The confidence interval of the estimate q^* depends on the amount of noise in the data. The idea is to find the confidence range of q^* in such a way that the increase of the cost functional j is of the order of the image noise with standard deviation σ. The relation

$$\frac{1}{2}(q - q^*)^T \boldsymbol{H}(q - q^*) \leq \sigma^2 \tag{4.26}$$

can be reordered to give confidence bounds for the control parameter q^*, which is equivalent to the pressure drop. With the image noise already determined in section 4.3.5 it is possible to calculate the asymptotic standard parameter error (Press et al., 2002) of q by

$$\sigma_{q_i} = \sigma\sqrt{2\boldsymbol{H}^{-1}_{ii}}\,. \tag{4.27}$$

For this case the index i is redundant, because the Hessian is a one-by-one matrix. For multiple parameters it is possible to estimate the individual asymptotic standard errors with the corresponding matrix entries at the diagonal. The inverse of the Hessian is known as data covariance matrix and can be interpreted as confidence ellipsoid. For this one-parameter estimation problem the inversion of the Hessian is trivial because it is a scalar. Figure 4.19 shows the estimated asymptotic standard errors for the pressure control.

Obviously, the asymptotic standard error depends only on the noise and is hardly effected by the motion. For a maximal velocity of $1\,^{\text{pixel}}/_{\delta t}$ with no noise, the relative

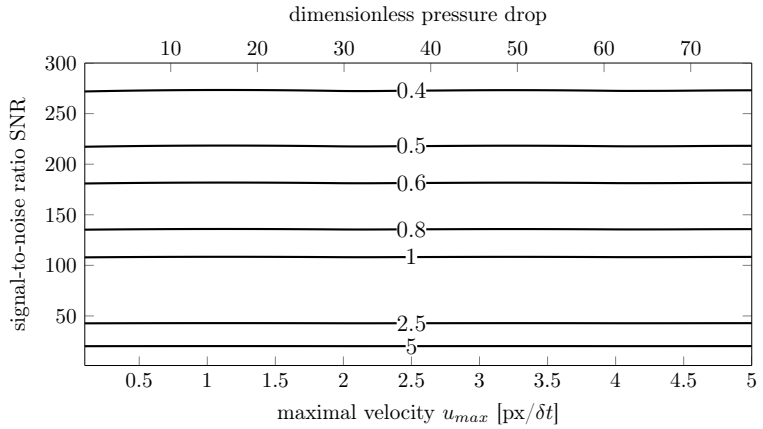

Figure 4.19: This plot shows the estimated asymptotic error of the pressure drop. It depends just on the noise level and is independent of u_{max}. The absolute standard error is normalized and corrsponds to pressure value of the upper horizontal axis.

standard error is about 2 %. Larger velocities yield a lower relative error because of the constant error with larger pressure drop. Since the velocity depends linearly on the pressure, it has the same relative error. It seems unfortunate that the motion has no effect on the shape of the minimum. Consequently, the stability of the optimal control estimate can not be used as a measure for the accuracy because it depends basically just on the image and not on the motion.

4.3.8 Generation of three-dimensional data

The previous section assessed the errors of the combination of PDE constrained motion estimation with images by means of two-dimensional data. From this point on the focus lies on the error, which is induced by the physical models. For this purpose, three-dimensional reference data was produce by solving the time-dependent advection-diffusion equation in equation (4.12). The forward simulation was solved for 100 steps within one time unit using a second-order Crank-Nicolson scheme in order to keep the numerical dissipation small (Thomas, 1995) and three preceding Euler steps to accelerate the solution finding procedure. The dimensions of the domain were set in such a way that they compare to the measurement channel: length : width : height $= 1 : 1 : 0.25$. The domain was discretized by LPS-Q_1 finite elements and had about half a million nodes ($129 \times 129 \times 31$) in order to yield projected images of a reasonable size 129×129 pixels. Since the velocity field $\boldsymbol{u}$ is time-independent and the solution can be calculated analytically, see equation (4.7), it was not necessary compute it beforehand. The maximal velocity of $\boldsymbol{u}$ was set in such way that within one time unit the structures are convected by 1/3 of the channel length. For each time step this produces a maximal displacement of 0.42 pixel or 0.42 nodes, respectively. The normalized kinematic viscosity κ^* was set to values ranging from 10^{-1} to 10^{-5}. In order to imitate the measurements, an initial 4×4 dot pattern were chosen that was equally distributed over the height of the channel. The small number of dots in the pattern was chosen so that each dot is represented by a sufficient number of nodes in order keep discretization artifacts small. Figure 4.20

shows the iso-surfaces of the fluorescent density ρ for three time steps and three diffusion coefficients.

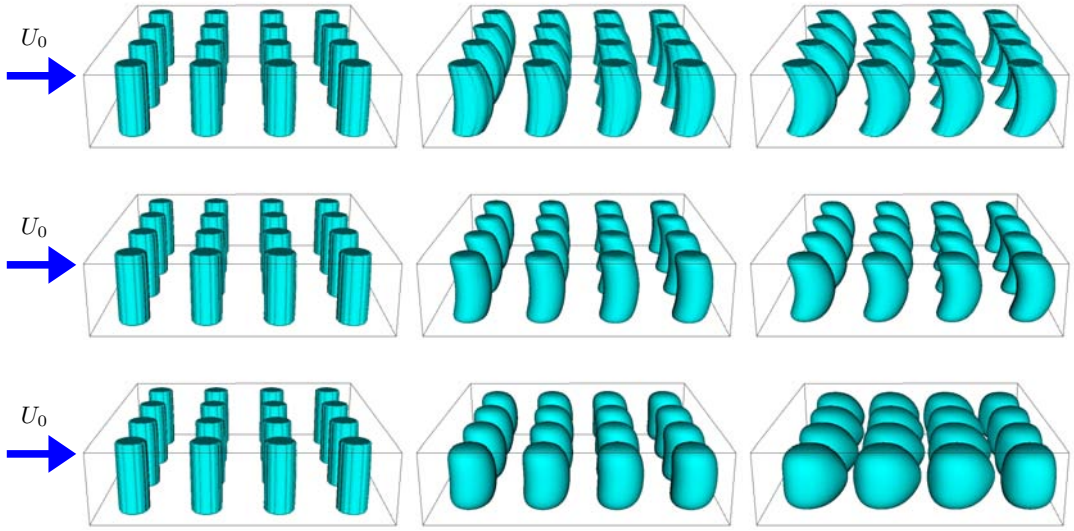

Figure 4.20: This figure shows in each row three forward simulated time steps ($t^* = 0, 0.15, 0.3$) of the advection-diffusion equation (4.12) in a rectangular channel with different diffusion coefficients. Top row: $\kappa^* = 10^{-5}$, Middle row $\kappa^* = 10^{-3}$, Bottom row $\kappa^* = 5 \cdot 10^{-3}$.

The density ρ was integrated along the height to yield 8bit reference images that were used to assess the accuracy (see figure 4.21). For the smallest diffusion coefficient, the image structures remain rather sharp in the vertical direction and get fuzzy in the horizontal direction due to the advection and the projection. For larger κ^* this effect is blurred by the diffusion. Although a second-order numerical scheme was used to calculate the forward simulation there is a measurable dissipation of about 0.4 % of the intensity between two time steps. This accumulates over 100 time steps so that just 2/3 of the initial intensity remains at the final calculation. In particular, this issue is visible for the three images of $\kappa^* = 0.001$ in Figure 4.21.

4.3.9 Parameter estimation approach with 3D motion model

The focus lies on the estimation of characteristic model variables, like the velocity field $\boldsymbol{u}$ and the diffusion coefficient κ. The estimation of diffusion coefficients is especially important for biological and medical flows that involve macro-molecules of several thousand atoms (Gregor et al., 2005; Thiagarajah et al., 2001). A specific example is the research of DNA diffusion coefficients in micro devices (Curtin et al., 2006). Rather than finding the velocity field $\boldsymbol{u}$ it is also possible to estimate the pressure drop along the duct and calculate the corresponding velocity field from it. This is possible because the given flow is purely pressure-driven (Poiseuille flow). The problem in equation (4.14) simplifies to finding a pressure drop such that the modeled image is the closest to the measured image. Without the loss of generality p_{in} is set to zero, which leaves p_{out} and κ to be estimated. The squared L^2-norm is chosen as the measure of similarity, which is the

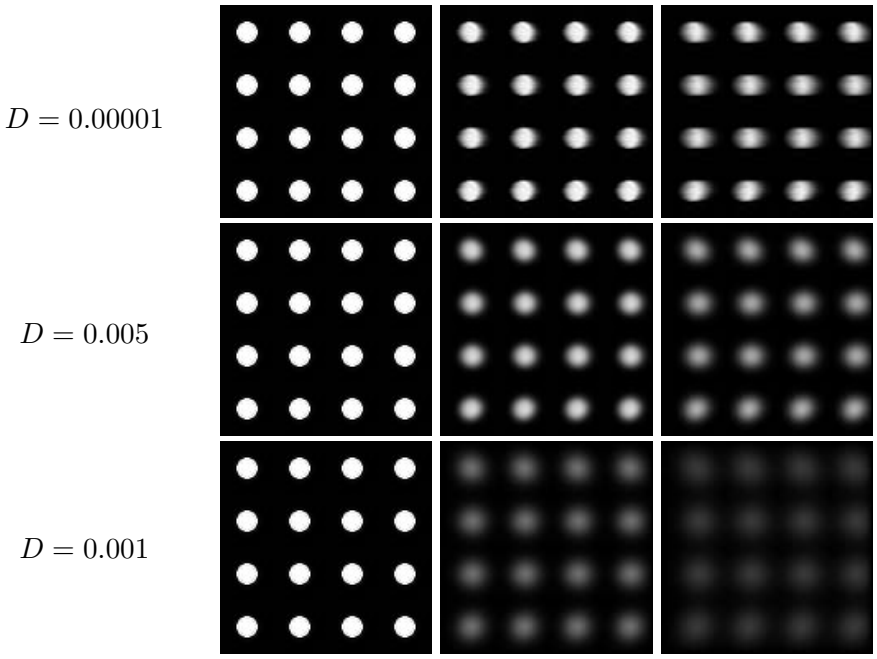

Figure 4.21: This figure shows the synthetic images that correspond to the fluorescence densities ρ shown in Figure 4.20

correct norm if Gaussian noise can be assumed (see A.4). In this case the minimization problem reads

$$\min_{\{p_{out},\kappa\}} \|I_i - \hat{P}^{\downarrow}\rho\|_{\Omega}^2 \qquad \text{s.t. } \mathcal{C}\,, \tag{4.28}$$

where $\mathcal{C}$ are the constraints from equation (4.14). Because the velocity in a straight rectangular duct can be calculated analytically, it is convenient to replace the Stokes equations and boundary conditions in $\mathcal{C}$ by the explicit solution from equation (4.7).

Neglecting for now the diffusive effects and focusing on the advection effect allows to simplify the model, such that the density is just transported and projected by $\hat{P}^{\downarrow}\hat{D}\rho$. In order to account for diffusive effects that play a major role for large κ, it is modeled by a convolution with Gaussian bell function G_κ that has a time-dependent variance. The justification of this procedure originates from the fact that the solution of the diffusion equation can be written as a convolution with a Gaussian bell function (see Appendix A.5). This applies also to the projected density because the diffusive effects along the integration path cancel each other. Consequently, the projected diffusion can be described by the same diffusion coefficient κ as the diffusion in three dimensions (see Appendix A.6).

Since all constraints can be expressed in an explicit manner, the problem from equation (4.28) can be written without constraints as

$$\min_{\{p_{out},\kappa,s\}} \|I_i - s \cdot G_\kappa * \hat{P}^{\downarrow}\hat{D}\hat{P}^{\uparrow}I_0\|_{\Omega}^2\,. \tag{4.29}$$

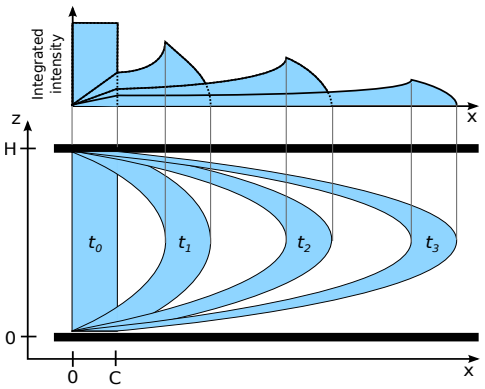

Figure 4.22: This illustration shows the Taylor dispersion of a density structure and the corresponding projected brightness if integrated along z.

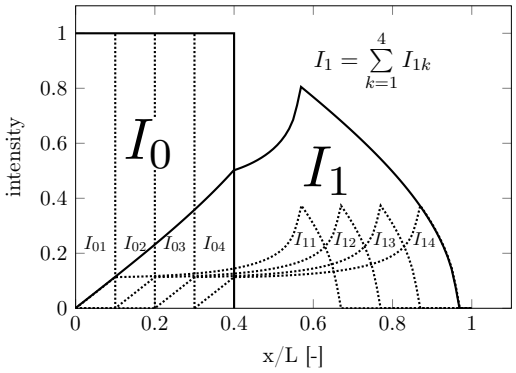

Figure 4.23: This plot illustrates the linearity of the filter described in equation (4.29). An image can be partitioned arbitrarily and the sum of all filtered image partitions adds up to equal the result of the filtered image.

This model includes an additional parameter s, which accounts for the decreased intensity due to numerical diffusion. The value of every pixel corresponds to the integrated density along the line of sight of that pixel. With progressing time the pixel intensity appears to be smeared over several pixels in the direction of the motion due to the velocity dependency in z-direction. This effect is illustrated in figure 4.22. The change of each pixel's brightness depends just on the pixel value itself, the velocity, the diffusion and the brightness contributions of the upstream pixels. Since the contribution from the other pixels is additive, all pixels can be treated independently and their results accumulate. Figure 4.23 illustrates this linear relation. The intensity I_0 is split into four smaller parts I_{0i}. Each part experiences the Taylor dispersion I_{1i}. The partial results are added up and equal the result from the Taylor dispersion of the entire intensity I_0. This behavior is characteristic for linear filters. It turns out that the operator $\hat{P}^{\downarrow}\hat{D}P^{\uparrow}$ can be expressed as a convolution with a position dependent function. The function depends on the velocity profile in y- and z-direction and in two dimensions it depends only on the y position. Under the assumption of a homogeneously distributed dye and a known velocity profile in z-direction the projection depends just in the length of the line of sight within the fluorescent dye:

$$\hat{P}^{\downarrow}\rho(\boldsymbol{x}-\boldsymbol{d}) = \int_0^H \rho(\boldsymbol{x}-\boldsymbol{d})\mathrm{d}z = \rho \int_{\rho(\boldsymbol{x}-\boldsymbol{d})>0} \mathrm{d}z\,. \tag{4.30}$$

With the prior knowledge of the z velocity profile, it is possible to replace the last integral by the length of integration path that is within the fluorescent dye. This length can be calculated by solving equation (4.7) for z. The calculation is analogue to the one in Garbe et al. (2008) with an additional dimension. Unlike the parabolic velocity profile in two dimensions, there is no explicit equation for z in three dimensions. Therefore, velocity profile is approximated by neglecting all terms with $m > 1$, which induces an error that is of the order $\mathcal{O}(1/(n^3 m))$ and has a standard deviation of 3.8 % of the magnitude. The error is the largest at the borders ($y \approx 0$ or $y \approx W$), where the profile deviates the most

from a parabola. Using this approximation, an equation for the integration length can be derived and reads

$$\begin{aligned} F_{c,p_{out}}(x,y,t) &= \frac{2H}{\pi}\left[\arcsin\left(\frac{x}{k}\right) - \arcsin\left(\frac{x-c}{k}\right)\right] \\ \text{with} \quad k &= \frac{16}{\pi^4}\frac{p_{out}t}{\mu L}\sum_{n \text{ odd}} \frac{\sin(\pi\frac{n}{W}y)}{n(\frac{n^2}{W^2}+\frac{1}{H^2})}\,, \end{aligned} \tag{4.31}$$

where the variable c contains the width of the pattern structure and t denotes the time. An important fact is the linearity of this equation. An intensity pattern can be divided in smaller parts and the time evolved pattern can be calculated by the summation of the time evolved parts (see Figure 4.23). This allows to break down the intensity patterns to pixel size, to calculate the time developed results and to sum them up. Because of the geometrical symmetry, this operation can be done by an one-dimensional convolution along the streamlines with the function $F_{1\,px,p_{out}}$. Because $F_{1\,px,p_{out}}$ is different for every y, the line convolution is denoted with "$\star$" so that the minimization problem reads

$$\min_{\{p_{out},\kappa,s\}} \|I_i - s \cdot G_\kappa * F_{1\,px,p_{out}} \star I_0\|_\Omega^2\,. \tag{4.32}$$

4.3.9.1 Assessment of the accuracy

The 3D simulated images are shown in figure 4.21 and were used to test the approach before applying it to the real measurement data. Figure 4.24 shows the estimated parameters in relation to the ground truth parameters. Since the image intensities for each κ level off at a different speed, each image sequence could be evaluated just up to a certain image. Therefore, the graphs do not cover the entire displacement range. The first graph shows the estimated pressure drop for different diffusion coefficients κ. It becomes apparent that this method yields better results for large displacements where the estimated pressure approaches the ground truth value with a deviation of less than 3 %. This statement holds for all diffusion coefficients except for the largest. Here, the molecular and numerical diffusion becomes extremely large, so that hardly any brightness is left beyond 15 time steps. The oscillations in the beginning stem from the fact that for small displacement the modeling is inaccurate due to its discretized nature of the filter. For small displacements the diffusion coefficient is also not accurate. In this situation the Gaussian function is not an appropriate representation of a continuous Gaussian function becaues it has a width of less than 3 px, which is to small.

The diffusion coefficient is estimate nearly 10 % lower than the reference value. One of the reasons is the boundary effect that is not included in the model and the other the reason is the dependency of the two parameters κ and s. Both parameters cause a decrease of the initial intensity so that the diffusive brightness loss is partially captured by the scaling parameter s. However, the estimated diffusion coefficient stabilizes with larger displacement. The scaling parameter is about to capture the loss of intensity by numerical diffusion. The largest intensity loss happens in the first time step where the initial intensity pattern is displaced for the first time. For every additional time step the intensity decreases gradually until the density is about to leave the domain.

The results are quite good considering the initial error of nearly 4 % that originate from the first-order approximation of the 3D velocity profile in z direction. Among the parameters the pressure can be estimated best because it depends mainly on the center part of $u(y)$ where the approximation is good. The image parts close to the border with larger approximation errors contribute less because of the smaller number of involved pixels.

4.3.10 Application to MTV measurements

The parameter estimation approach is applied to MTV measurements taken from the PhD work of Roetmann (2008) with courtesy of the Laser Laboratorium Göttingen e.V. Figure 4.25 shows image examples of two of the eight datasets that were provided. For illustrative purposes the upper half of each image shows the initial fluorescence pattern and the bottom half its time-evolved counterpart. Roetmann experimented with different initial patterns in the datasets, e.g. dot size and distance between the dots.

The minimization problem from equation (4.32) was used to estimate the diffusion coefficient κ and the pressure drop δp along with the scaling factor s. The latter parameter accounts for the excitation delay of the molecules but also for the photo bleaching effects that alter the intensity of the recorded fluorescence light (Roetmann, 2008, see Figure 3.4 and 3.5). Although Roetmann applied a static pressure differences in the first place to drive the flow, the only recorded parameter is the volume flow rate Q_{ref}. The flow rate Q can be calculated by knowing the velocity u or pressure drop, respectively. It is calculated via the relation

$$Q = \int_0^W \int_0^H u(y, z) \mathrm{d}y \mathrm{d}z \tag{4.33}$$

and with the analytic expression for u that is given in equation (4.7). The trigonometric functions can be integrated to yield the conversion formula

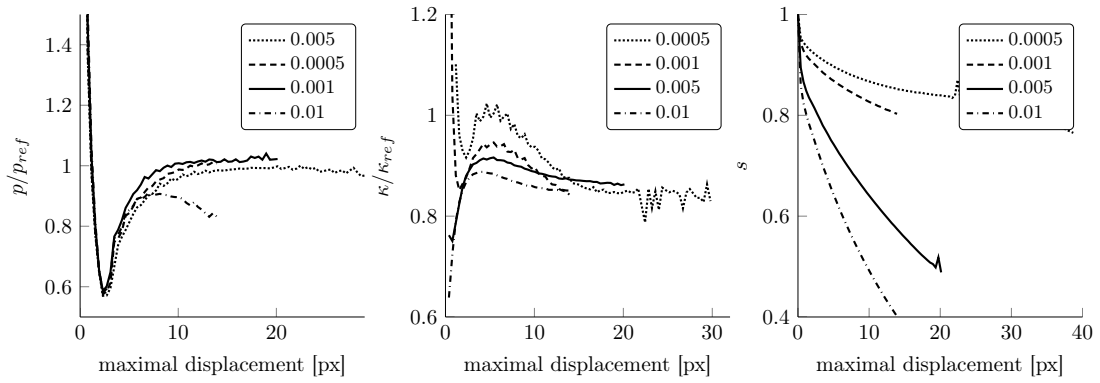

Figure 4.24: These graphs show the estimated parameters using equation (4.32) after normalization with the corresponding reference value for simulations with $\kappa = \{0.0005, , 0.001, 0.005, 0.01\}$. From left to right the graphs show the pressure p, the molecular diffusion coefficient κ and the scaling parameter s.

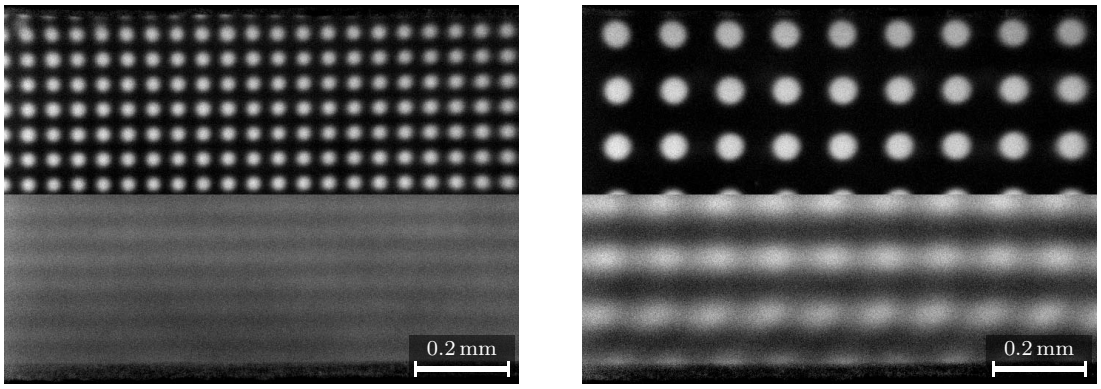

Figure 4.25: These two images show a split view from the initial (top) and time evolved (bottom) images of two MTV measurements with different patterns and pressure drops (data sets: G025D200, G375D300 with frame {4, 88} and {4, 90} of the sequences)
.

$$Q = \frac{64}{\pi^6} \frac{p_{out} W H}{\mu L} \sum_{odd\ n,m}^{\infty} \frac{1}{\left(\frac{n^2}{W^2} + \frac{m^2}{H^2}\right) n^2 m^2} \,. \tag{4.34}$$

Another conversion has to be done in order to determine the diffusion coefficient. The diffusion coefficient κ connects to the mean squared Brownian motion distance σ by the relation

$$\sigma = \sqrt{2n\kappa t}\,, \tag{4.35}$$

where n is the number of spatial dimensions (Einstein, 1905). The value for σ corresponds to the standard deviation of the Gaussian for the convolution and gives the possibility to estimate κ. Figure 4.26 shows the maximal velocity u_{max}, flow rate Q, diffusion coefficient κ and scaling parameter s for six reference flow rates of the dataset G375D300. The top left graph reveals that u_{max} is determined quite constant over the entire sequence besides the large displacements of more than 16 px and the overlapping intensity structures (see figure 4.25 right). For the first few frames, the graphs have larger deviations, which are caused by the unsaturated fluorescence light and the fact that this approach performs unstable if the displacement is too small. The maximal velocity is directly connected to the flow rate Q, which can be normalized by the reference value. Considering the first-order approximation of u, the flow rate Q can be approximated quite good. The normalized values come close to unity $(0.94 \pm 5)\,\%$ for the this dataset. Large fluctuations around the mean occur for the estimation of the diffusion coefficient κ. There are several reasons for this instability, e.g. the degree of noise in the images, which is more significant in the initial phase and the dependency on the quality of the other parameter, especially with respect to the scaling parameter. The latter is illustrated in the last plot of figure 4.26, where the scaling parameter s shows the increase of intensity up to 35 % within 30 frames. This is caused by the continuous excitation with the laser light that renders more and more molecules fluorescent. An equivalent graph can be produced by

plotting the integrated intensity of the images over time (see Appendix A.12). Therefore, the parameter s is proportional to the amount of excited fluorescent dye molecules.

The evaluation was done for all eight datasets that were provided by Roetmann and the results are plotted with the corresponding one-σ-errorbar in figure 4.27. It becomes apparent, that the errorbars of the flow rate are notably larger for datasets ending with D150 or D200. The number of the name corresponds to the distance between the dots. The smaller the number is, the closer are the dots and as a consequence the individual dots structures overlap earlier in time. However, the flow rate could be estimated for all datasets within a range of (90-100) % of the reference flow rate. In order to calculate the overall estimate of Q/Q_{ref}, the individual results were weighted with their reciprocal variance, which yields the value $Q/Q_{ref} = 0.95 \pm 0.06$. One reason for the lower estimate is the unknown position of the walls. The experimental images had not been produced with an exact parallel projection, so that the sides of the wall are visible. This led to a smaller estimated domain and consequently a lower flow rate was estimated. The evolved dot pattern does not have a perfect mirror symmetry with respect to the center of the channel which indicates that the top and bottom plate are not exactly parallel or have artifact from the production process. The same procedure was done to calculate the diffusion coefficient κ. Since the images for the datasets had been taken in an alternating manner throughout two days, an average temperature shift can be excluded that would have altered the diffusivity. Figure 4.26 shows the κ estimates of one dataset. Usually κ oscillates for small times $t < 1\,\text{sec}$, which is damped quickly with progressing time. Therefore, the first few estimates of all datasets are not included for the averaging ($t < 1.5\,\text{sec}$). The overall diffusion coefficient of *caged Q-rhodamine dextran* in water at 20° C could be estimated[3] to $\kappa = (55 \pm 16)\,\mu\text{m}^2/\text{sec}$. This value can not be compared to literature values because there are no publications that are related to this substance. However, since dextran makes up the largest part of this molecule, it is reasonable to compare the estimated κ to the dextran diffusion coefficients of similar molecules size ($\approx 10\,000$ Dalton). According to Laurent et al. (1976) κ values range between $30\,\mu\text{m}^2/\text{sec}$ and $79\,\mu\text{m}^2/\text{sec}$. Other publications report diffusion coefficients of $(78 \pm 47)\,\mu\text{m}^2/\text{sec}$ for dextran in oral biofilms (Takenaka et al., 2009), $29.1\,\mu\text{m}^2/\text{sec}$ (Gregor et al., 2005) or $91\,\mu\text{m}^2/\text{sec}$ Thiagarajah et al. (2001). Considering the large range of published results between (30–91) $\mu\text{m}^2/\text{sec}$, it can be remarked that the estimated diffusion coefficients of all datasets lie within these limits.

4.4 Micro-mixer

The previous straight channel experiment was used as a test case with known analytic solution for the study of the accuracy and the limitations of the proposed methods. A more interesting and challenging application is now presented that shows the large potential of PDE constrained motion estimation: a fluid micro-mixer with multiple in- and outlets (Roetmann, 2008). Two images of the device are shown in figure 4.28 and the computational domain and boundaries are shown in figure 4.29. Such devices are primarily used for mixing multiple fluids, which is a key task for chemical, pharmaceutical, medical or biological diagnostics. The presented micro-device has six openings and is

[3]The mean and standard deviation were computed using a mixture of gaussian distributions Trailović and Pao (2005).

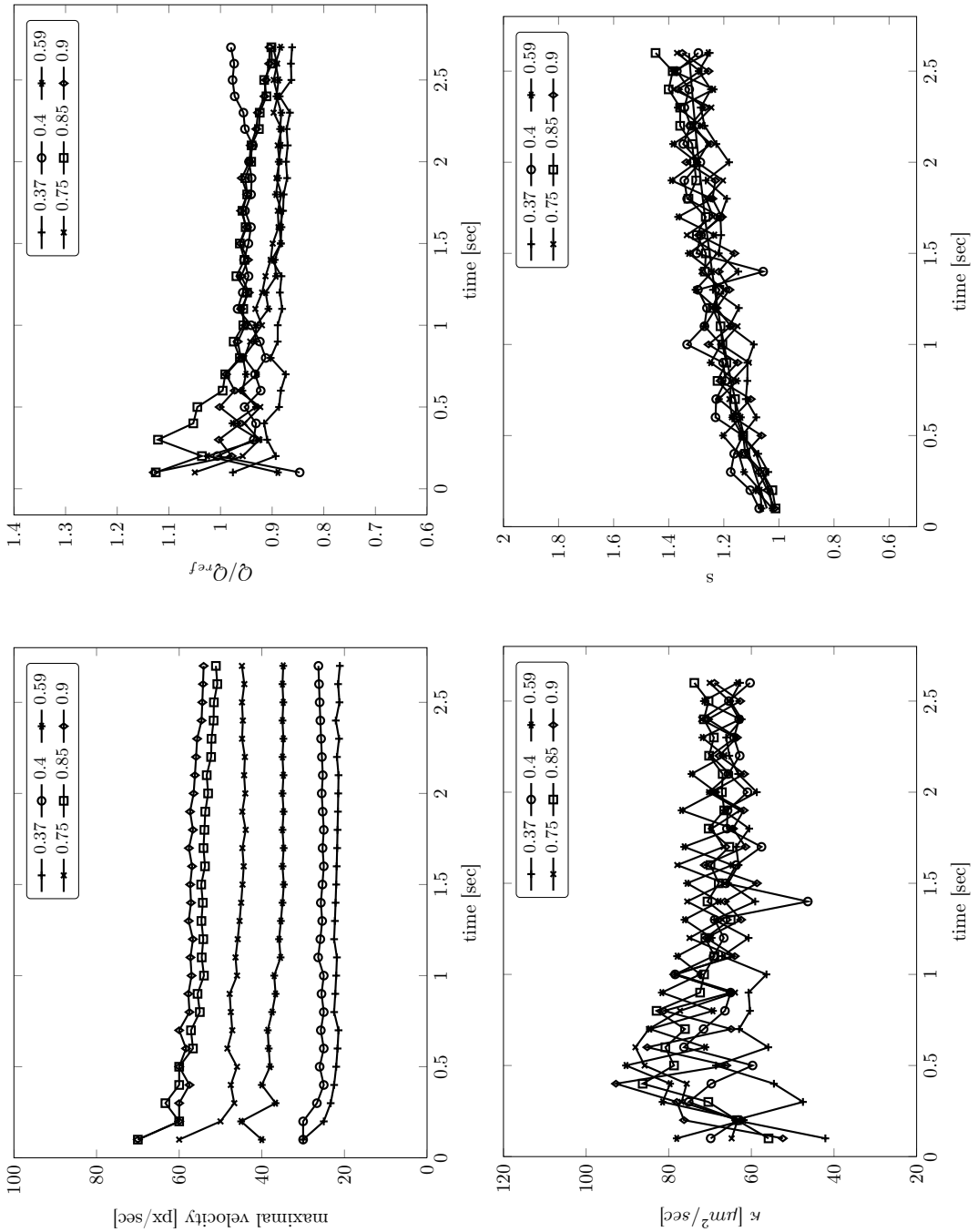

Figure 4.26: Each of these figures shows the graphs for six flow rates (in ml/min) of the image dataset G375D300. The maximal velocity u_{max}, normalized flow rate Q/Q_{ref}, diffusion coefficient κ and scaling parameter s are displayed over the time axis which corresponds to 27 image frames (frame rate: 10 Hz).

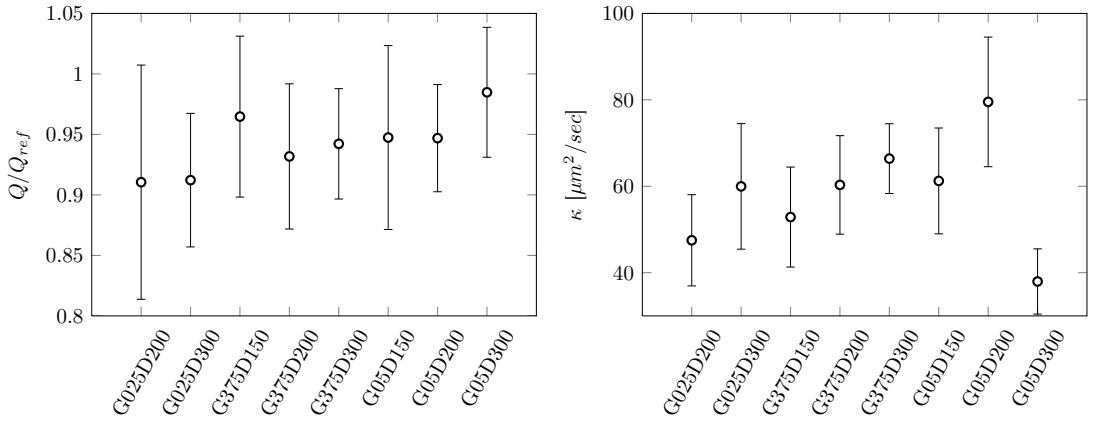

Figure 4.27: These graphs show the estimated flow rates Q and diffusion coefficients κ for the all measurement configurations. The error bars show the deviation of the estimate within the individual image sequence.

operated with a hydrostatic pressure difference, like the micro-channel. Consequently, the flow is also a *Poiseuille flow* and fully described by the average pressure values at the openings. The area of the mixing chamber has a size of $1 \times 1 \times 0.2\,\mathrm{mm}^3$ and is comparable to the geometrical characteristics of the micro-channel. Several experimental settings have been done with partially opened or closed in- and outlets. However, the experiments had been conducted to show the feasibility of performing MTV measurements in complex micro-devices. Therefore, the measurement settings had not been adjusted accurately and as a consequence had not been recorded.

4.4.1 Average pressure control

This example is ideal to be analyzed by the parameter estimation of the average pressure values at the openings because is fully described by these quantities. Therefore, the

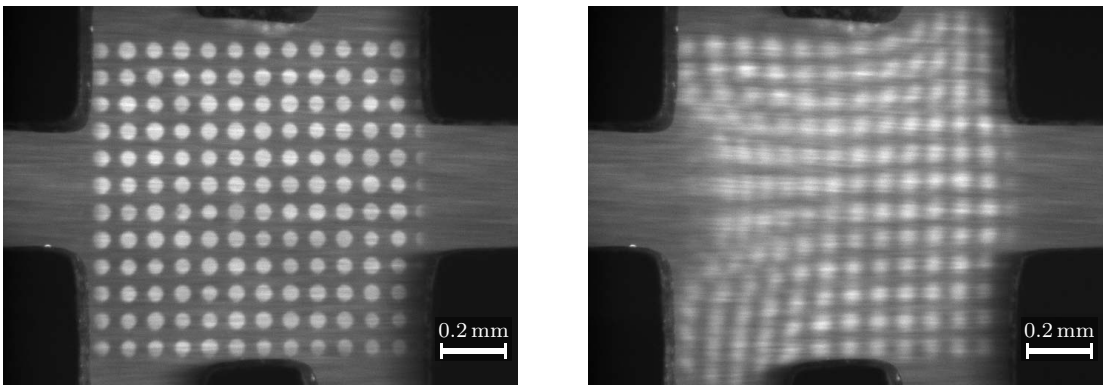

Figure 4.28: These images show a micro-mixer with six openings and the initial dot pattern that was marked into the fluid. The left image represents the first frame picturing the prescribed pattern, the right image 5.5 sec later after the pattern is convected.

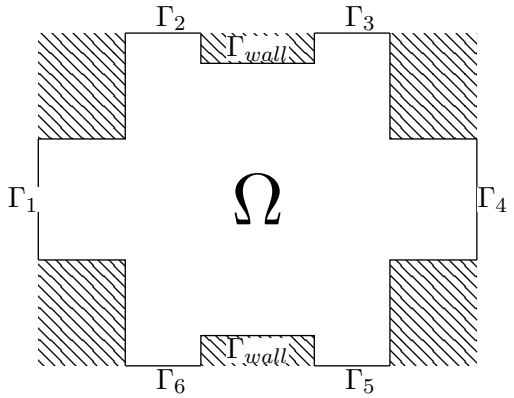

Figure 4.29: The scheme illustrates the flow domain and its boundaries that is used to evaluate the micro-mixer images.

parameter estimation problem from equation (4.23) is extended to include six openings instead of just two. The problem for this setup has five parameters $q_1, ..q_5$ and reads

$$\min_{q_1,...q_5} \frac{1}{2}\|\partial_t I + \boldsymbol{u}^T \nabla I\|_\Omega^2 \quad \text{s.t.} \begin{cases} \mathbf{0} &= \frac{1}{\mathrm{Re}}\Delta \boldsymbol{u} - \nabla p & ,\text{in } \Omega \\ 0 &= \nabla^T \boldsymbol{u} & ,\text{in } \Omega \\ \boldsymbol{u} &= \mathbf{0} & ,\text{on } \Gamma_{wall} \\ p &= 0 & ,\text{on } \Gamma_6 \\ \boldsymbol{n} q_i &= \frac{1}{\mathrm{Re}}\partial_n \boldsymbol{u} - \boldsymbol{n} p & ,\text{on } \Gamma_i,\ \forall i = 1,..,5 \end{cases} . \tag{4.36}$$

As for the straight channel, the average pressure value for one opening (Γ_6) can be set to zero without the loss of generality. The computational framework RoDoBo handles this problem in the same manner as the straight channel example. Therefore, there are just minor adaptations that have to be made in order to make it work. One notable problem is the generation of the computational mesh, which is described in the following.

4.4.2 Mesh generation

The PDE control solver RoDoBo computes the solutions starting from a coarse mesh, which is refined automatically in an iterative manner until the final resolution is achieved. The geometry of the micro-mixer domain is far more complex than the domain of the straight micro-channel. Curved boundaries require to set up the initial mesh accurately, so that the mesh boundaries coincide with the pictured boundaries in the images. The general refinement approach of RoDoBo adds a new node in the center of all edges and at the middle of each finite element. In order to allow curved boundaries in RoDoBo, the position of the edge nodes can be corrected by an analytic function. However, a mathematical description of the boundary, which is shown in figure 4.28 is difficult to find. It would be most convenient to use image processing methods to detect the boundaries and use this information to generate the mesh accordingly. In order to realize this procedure, a *Canny-edge*-filter (Canny, 1986) was used to mark the visualized edges. After some post-processing steps (e.g. smoothing, binarization, skeletonizing) for the removal of wrong edges and other artifacts, the edges are nicely emphasized as illustrated in figure 4.30 on the left. The idea is to shift the border nodes of the mesh to the closest

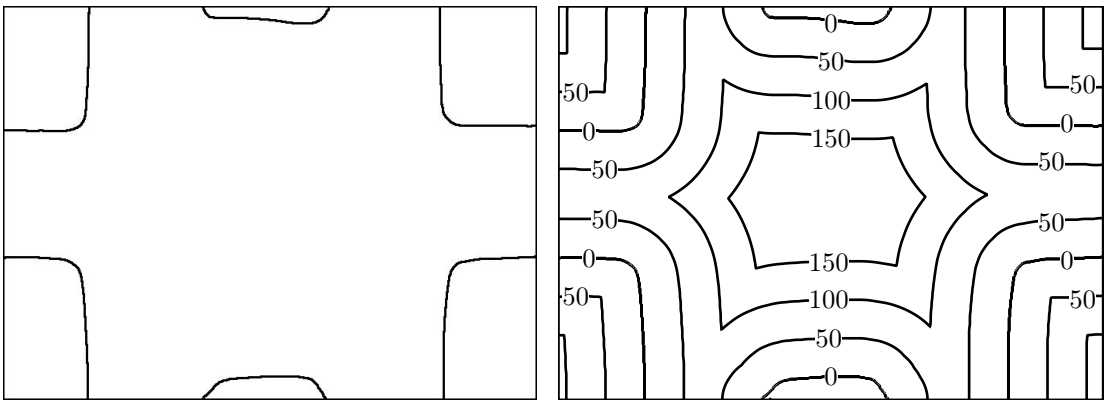

Figure 4.30: The left figure shows the emphasized walls of the micro-mixer in the images. From this edge-image it is possible to compute a distance function for every pixel position (right figure). The contour lines show the minimal distance to the closest wall in pixel units.

segment of the wall. This allows to begin with an initial mesh that corresponds roughly to the actual borders and which is corrected automatically in each refinement step. The correction of the node positions can be done with computing a potential function, which returns the shortest distance for every pixel in the image to the next border pixel. The calculation of this potential function (see figure 4.30 right) is done with a *fast-marching method* (Sethian, 1999) that has a computational complexity of $\mathcal{O}(n \log n)$, with n being the number of pixels. Having this function allows to use minimizing algorithms to find the closest wall segment. The only requirement of this approach is that the initial positions of the nodes should be close to the corresponding border segment. However, with this method the laborious work of generating accurate meshes can be reduced, which makes it more convenient and easy to adapt for other experiments and other geometries.

An accurate representation of the domain can be achieved by this method as it is shown in figure 4.31. The initial mesh grid consists of nearly equilateral Q_1 finite elements. Additional nodes are added in each refinement step and shifted to the closest image border, thus allowing the mesh to cling to the image borders. It has to be remarked that the mesh refinement has to be limited by the resolution of the pixel grid. The reason is that the potential function is just accurate up to the pixel resolution. A refined mesh beyond this resolution can lead to degenerated finite elements that have nodes with identical positions or overlapping areas. Under these circumstances the solver diverges because the requirements of a valid FEM discretization are not fulfilled anymore. In order to prevent this, the FEM mesh refinement is stopped at the image resolution and the initial mesh was chosen according to the mentioned restrictions.

4.4.3 Micro-mixer flow

The first two consecutive images of the sequence were chosen to be evaluated with the average pressure control approach, which was outlined before. The very same images are evaluated with optical flow and PIV. In order to allow a convenient comparison, all results are shown in figure 4.32 with equal scalings. Since PIV and optical flow can

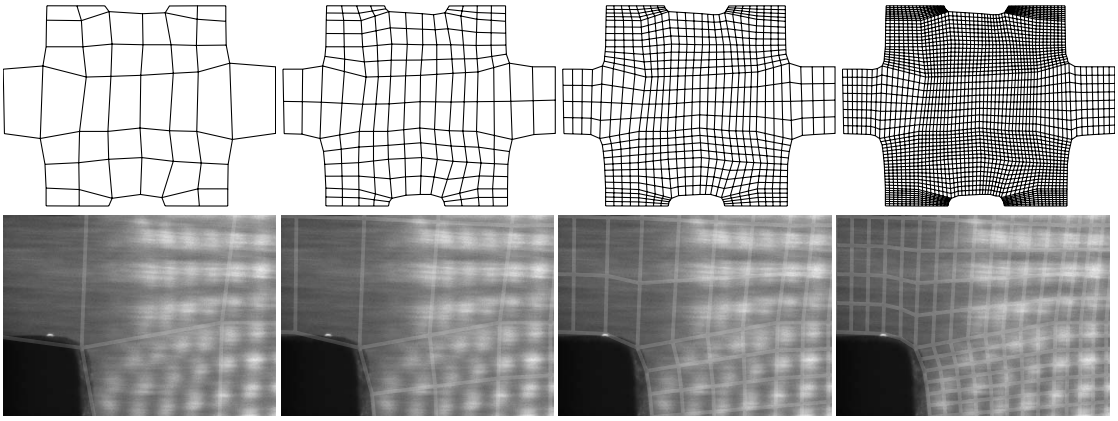

Figure 4.31: This figure shows in the top row the first four meshes for the micro-mixer experiment. The bottom row images focus onto a closeup region of the above meshes with the underlying micro-mixer images to see the working principle.

not estimate pressure, the corresponding places are left blank and marked with a cross. The PIV results were obtained by using a hierarchical interrogation window sequence of $96 \times 96\,\mathrm{px} \rightarrow 64 \times 64\,\mathrm{px} \rightarrow 32 \times 32\,\mathrm{px}$ on every fourth pixel in vertical and horizontal direction. The optical flow algorithm was applied with a image pyramid scheme that scales the images in 85 % steps down to one third of the initial width. The regularization parameter α was set to unity as for the micro-channel.

Although there is no image information in the left opening, PDE constrained motion allows a physically sound extrapolation because of the global motion model. The two other local motion model approaches are not capable to estimate any reasonable velocity because of their simple motion model. By virtue, they are just able to estimate the motion where the brightness is significantly structured.

The drawback of the local model is clearly visible in the plots of the u- and v-component. The regular image pattern produces a velocity beating, which can be seen nicely in u-component of the optical result and is also present in the PIV results. On the other side, the rigid PDE constraint produces numerical results that appear feasible since they come from the solution of the PDEs. However, the v-component appears to be a smoothed version of the corresponding PIV and OF results. Especially the contour lines of the PIV results resemble closely to the ones of the PDE result, qualitatively and quantitatively. Only for large velocities ($|u| > 8\,\mathrm{px}/\delta t$) the magnitude and shape differ notably. It has to be mentioned, that the two-dimensional Stokes equations are used to yield this result. This explains why the velocity towards the openings turns into a parabolic profile. As a consequence, the estimated inflow velocity is higher than the velocity that is predicted by the other methods because it flow rate has to be conserved. On the other hand, the magnitude of the v-component at the lower left outlet is underestimated because the two-dimensional PDE solution does not satisfy any other profile.

The lower dimensional model shows in some parts significant deviations from the actual motion. Especially in areas close to the border and the inlets, the additional dimension alters significantly the profile and cannot be estimated properly by the two-

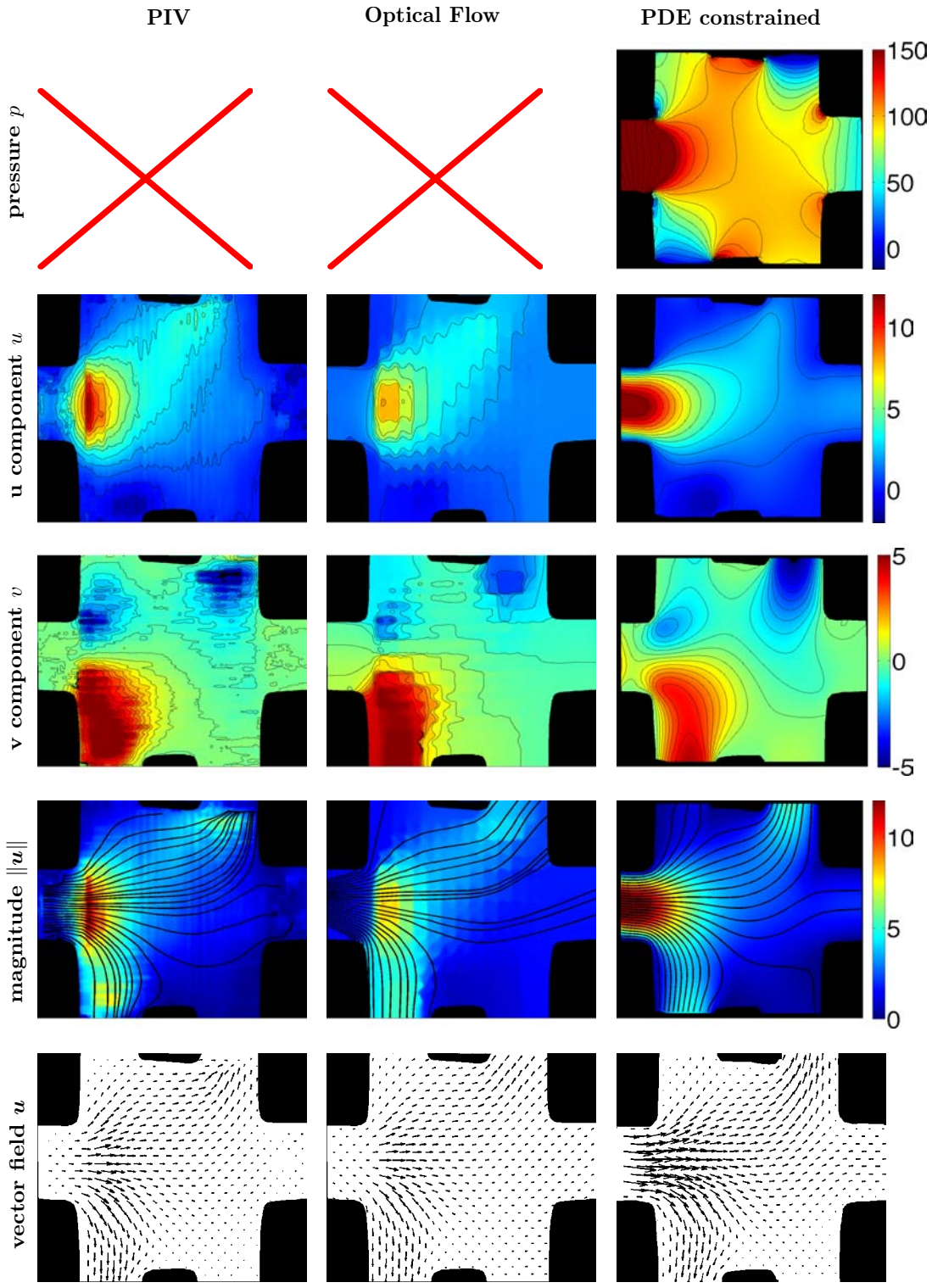

Figure 4.32: This figure shows the results of PIV, optical flow and PDE constrained motion estimation using pressure controls. The scale of all plots is in units of $^{\text{px}}/_{\delta t}$ except the pressure plot, which is in nondimensional units and can easily be converted by multiplying with ρU^2 ($\mathcal{O}(100\,\text{nN})$).

dimensional flow model. In image parts far away from the borders and with low velocities this effect is much smaller, so that PDE constrained modeling yield comparable results.

4.4.3.1 Stability of the parameters

In order to investigate the influence of the Taylor dispersion, this method was applied to different consecutive image pairs from the image sequence. So far, the first image, which contains the undistorted pattern, was used together with the proceeding image of the sequence. Since this flow is stationary, the exact same motion distorts the second to the third image, the third to the fourth image, and so on. Ideally, the estimated motion should be identical for all these image pairs. The Taylor dispersion could be neglected for the first pair of images because the fluorescence density corresponds to the prescribed pattern and the influence of the Taylor dispersion gains importance with increasing time and distortion of the initial pattern. Figure 4.33 shows the five parameters for 6 images pairs. The curved shape is recovered by all image pairs but they differ severely in magnitude. With every additional time step, the estimated magnitude of the pressure becomes smaller and consequently also the velocity estimates. However, it shows that the determined parameters of the first three image pairs have a similar magnitude (up to 10 %), which suggests that the influence of the Taylor dispersion is not yet sufficiently large to seriously corrupt the motion estimate.

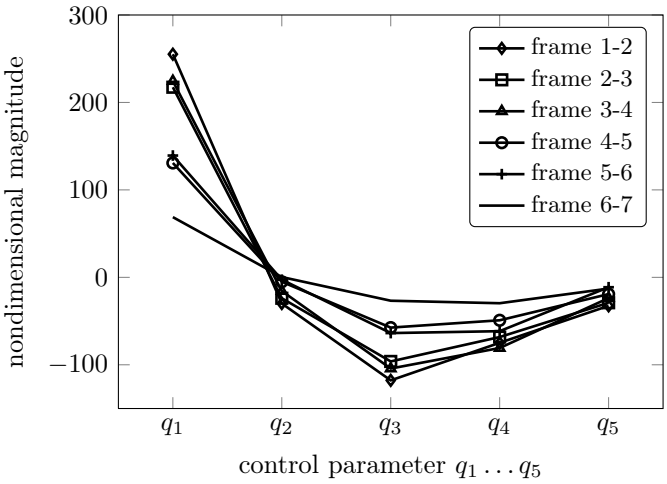

Figure 4.33: This graph shows the estimated average pressure values $q_1, \dots, q_5$ for different consecutive images.

4.4.3.2 Strength of global motion models

The real strength of using global motion models is demonstrated in the following example, where the MTV images contain much less dots and therefore sparsely distributed motion information (see figure 4.34) These images were processed in the same manner as the previous example of the micro-mixer but with lower pressure drop and a different dot mask. The motion information is sparsely localized with large distances in between. The results of this image pair are shown in figure 4.35. The standard methods PIV and OF

have extreme difficulties to estimate even the main flow direction. The few information of the dots does not suffice to allow a reliable estimation or interpolation between the dots. The only reasonable motion estimates occur at the locations of the dots, which also experience a corruption by the smoothing effect of the hierarchical schemes or the regularization. In contrast to these local motion methods, the PDE constrained motion estimation yields fairly the same results as the previous example with much more dots. The few motion information is sufficient to drive the global solution to a physically sound motion and pressure field. The image parts that do not contain any information, contribute hardly to the entire global solution.

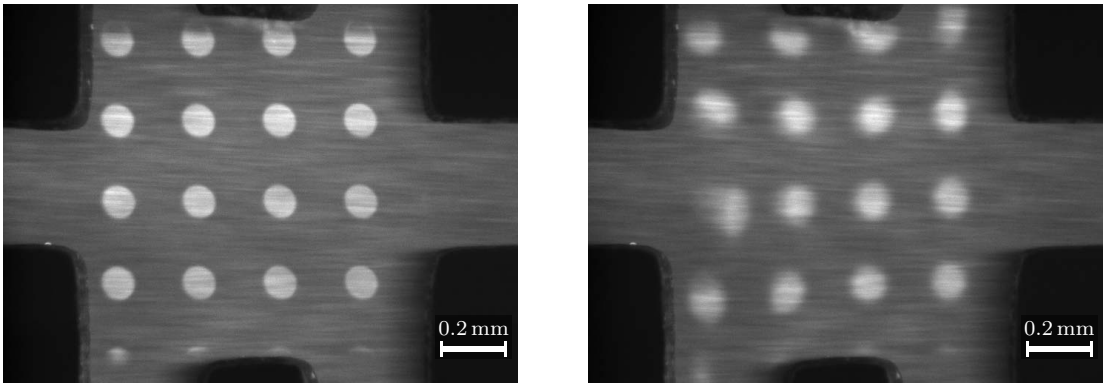

Figure 4.34: These images show a micro-mixer with six openings and the initial dot pattern that was marked into the fluid. The left image represents the first frame when the pattern is marked, the right image 5.5 sec later after the pattern is convected.

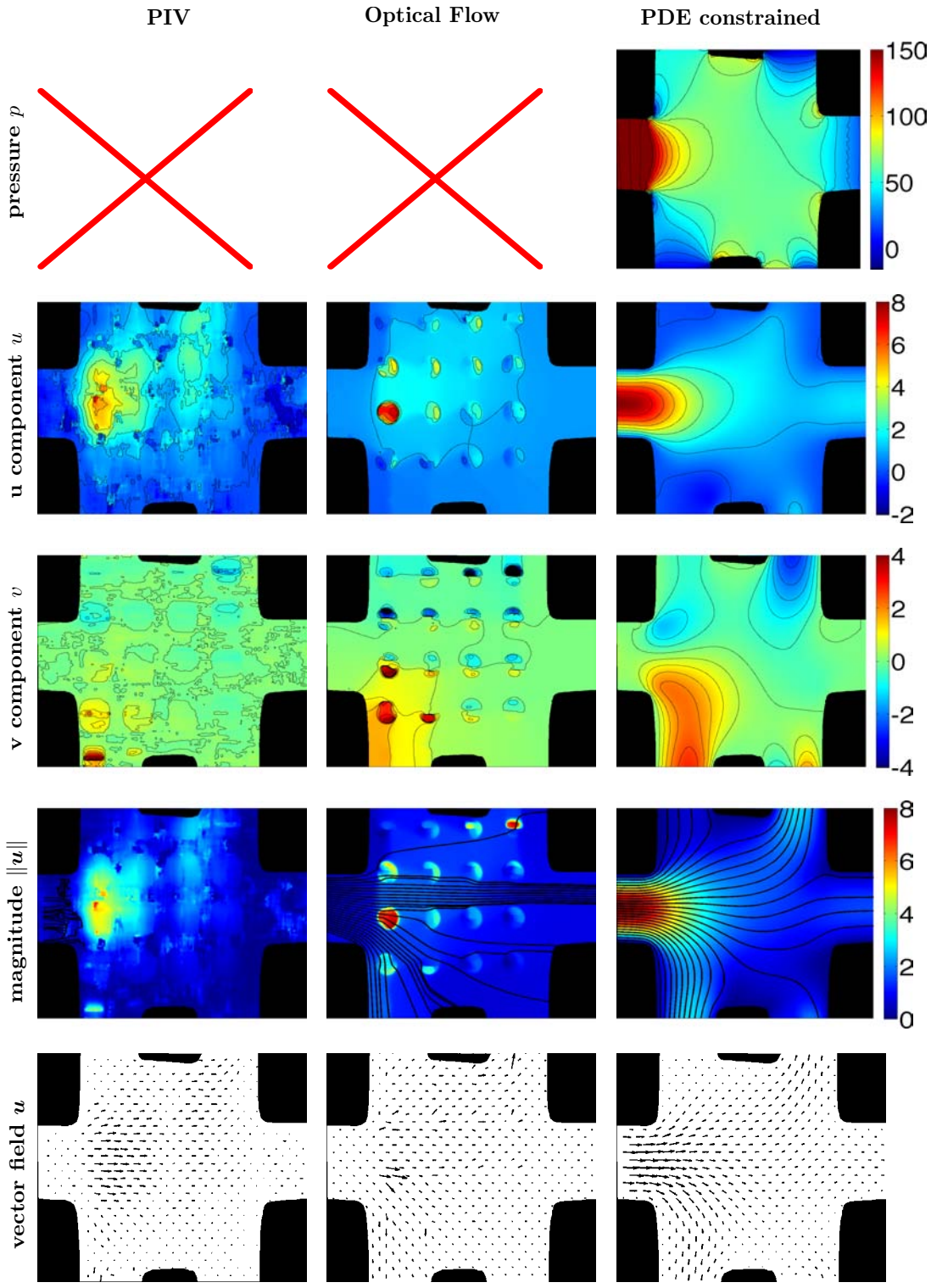

Figure 4.35: This figure shows the results of PIV, optical flow and PDE constrained motion estimation using pressure controls for a micro-mixer with a sparsely distributed image pattern. All units are in $^{\text{px}}/_{\delta t}$ except the pressure plot, which are nondimensional and can be easily converted by multiplying with ρU^2 ($\mathcal{O}(100\,\text{nN})$).

CHAPTER 5

Conclusion

The main objective of this thesis has been the application of global motion models for the evaluation of microfluidic flows. This was accomplished by combining fluid simulations with motion estimation methods for measurement data in an optimal control framework. The FEM-solver GASCOIGNE (Becker and Braack, 2005) and the optimization toolbox RODOBO (Becker et al., 2005) were used to parametrize the governing equations in order to find solutions that describe the measurement images. The solution space of the motion problem is reduced by considering only the subset that contains the solutions, which that satisfy the motion equations. This makes this method accurate and robust in comparison to other motion estimation methods. Furthermore, it is possible to impose boundary conditions that are a priori known for many experimental setups. This concept was tested and applied to *molecular tagging velocimetry* images that show integrated fluorescence light. In the following the main investigations and results of this thesis are summarized.

5.1 Summary

Local and global motion models

In this thesis it was demonstrated that global models provide the potential to analyze data which can hardly be evaluated by local methods. The MTV images do not contain densely distributed image information, which causes extreme difficulties for local motion frameworks. The results of local and global approaches can be compared qualitatively by examining the figures 4.7 and 4.8 for the local model and the figures 4.9 and 4.16 for global models. In this context, a comparison of the average errors with respect to the reference solution of the synthetic images does not make sense, because local methods yield many outliers that corrupt the solution. Global motion models are more robust and allow a physically sound interpolation between sparsely distributed image data. The example of the micro-mixing device from section 4.4.3 demonstrates impressively the usefulness of global motion models, where local models are not able to retrieve reliable estimates. However, the advantage of a global motion model is accompanied with the disadvantage of uncontrollable error propagation. Since all estimates are rigidly connected by the

equations, localized errors affect the global solution. On the other hand, local models restrain the error propagation by a larger solution space that allows a more flexible adaption or by dividing the problem into smaller non-connected parts. This limits the propagation length of the erroneous estimates as it is shown in correlation length in figure 3.6.

Optimal control of PDEs

The governing equations of viscous flow can be solved if the boundary conditions are known. With respect to optimization this means that the boundary conditions or the equations have to be changed in order to serve as an adjustable model. In this context, the general concept of optimal control was introduced in section 2.5 and the finite element method to solve PDEs was briefly outlined in section 2.7.
This approach was applied to synthetic data with a known reference motion that imitates MTV images as shown in figure 4.1. Two types of control variables were investigated: distributed control variables (section 4.3.7.1) and parameter control variables (section 4.3.7.2). Both were applied to the very same images, which had been generated with different noise levels and flow rates. The errors with respect to the reference solution are shown in figure 4.12 and figure 4.18 and reveal that the pressure as control parameter is much more robust than controlling the inflow profile. This distributed boundary control depends very much on the pixel data close to the border (see section A.7). However, this mainly effects the solution near the border because the equation damps this influence quickly. While looking at the estimated flow rate, it can be seen that both methods perform equally good. Besides the better accuracy of parameter controlled PDEs (compare figure 4.12 and figure 4.18), the deviations at the border are one of the reasons why parameter controlled PDEs are preferred over boundary controlled PDE approach. Another reason is the lower computational effort, that allows to compute gradients and Hessians explicitly, which makes it notably faster. And finally, it does not need any regularization parameters that have to be set by the user. Boundary controls have the benefit that they allow to relax the modeled settings. This was used to weaken the zero-wall-slip assumption as presented in equation 4.22. For a range of prescribed wall velocities the method was able to estimate fractional displacements with a maximal error of 10% at $1\,\mathrm{px}/\delta t$. In comparison with other wall-slip investigations from images (Joseph and Tabeling, 2005), this error seems to be more than acceptable. This study shows once more the large impact of the image data onto the estimated boundary control variables. Therefore, random images were generated to get rid of the image structure dependency (see figure 4.15). This revealed another issue, that counteracts against the accuracy and is discussed in the next paragraph.

The general problem of the optical flow constraint

The brightness constancy constraint equation in equation (3.10) is ill-posed and the only computable motion is in direction of the gradient (see *normal flow* in section 3.2.2.1). This causes the global models to overestimate the motion, which is due to the fact that shear induced image gradients contribute to the overall motion. This is illustrated in the figures 4.11 and 4.17 and in presence of noise in figure 4.12 and figure 4.18. Apparently, controlling the pressure preforms better than controlling the inflow motion. With respect

to the boundary control approach, the oscillating variations of the estimated boundary can be reduced by scaling $\partial_y I$ (see section A.8), which confirms the strong influence of the image structure. Another problem involving the BCCE is the Taylor approximation that prevents an accurate estimation beyond 1 px displacement between two images. Since there are no pyramidal schemes involved, the method is likely to become inaccurate for large displacements. However, image data from a micro-mixing device (section 4.4.3) was used to demonstrate the strength of global motion models. Velocities up to $12\,\mathrm{px}/\delta t$ are determined, which is not caused by the local image information but because of the global model that interpolates with respect to the governing equations. This leads to a physically sound interpolation of the motion, where image data does not provide sufficient information.

Confidence of the solution

Since PDE constrained estimates appear alway physically sound, it is difficult to tell, how trustworthy the results are. Optical flow methods that include a global optimization experience the same problem. An error estimation of the presented method is difficult because the shape of the minimum of the cost function depends just on the noise level and not on the motion (see figure 4.19). However, the stability of the estimation was tested by applying the method to different consecutive images that contain the same motion information (see figure 4.33). This allowed to determine the limits of the simplified two-dimensional model.

Estimation of the diffusion coefficient

The parameter estimation method had been extended to model a projected three-dimensional velocity field in a straight channel by using an approximated analytical solution (see section 4.3.9). The diffusive process was described by a convolution with a Gaussian function (see Appendix A.5), which can be used to estimate the diffusion coefficient. This approach was tested on synthetic images, which had been produced with a three-dimensional numerical simulation of the diffusion equation with constant advection velocity (see section 4.3.8). The results for different diffusion coefficients are shown in figure 4.24 and reveal that the pressure drop and diffusion coefficient can be estimated quite stable for the second half of the image sequence. The motion estimates come close to the reference solution with a deviation of less than 3% and the estimated diffusion reaches 90% of the reference value. The 10% discrepancy is caused by the numerical diffusion and discretization artifacts.
Finally, this method was applied to the MTV datasets of Roetmann (2008) and the estimated parameters are shown in figure 4.25 for a sample dataset. The flow rate and the diffusion coefficient could be estimated quite stable for all flow rates of this dataset. The model parameters were determined for the other datasets as well and averaged (see figure 4.27). The flow rate could be estimated up to $(95 \pm 6)\%$ of the reference value and the diffusion coefficient to $(55 \pm 16)\,\mu\mathrm{m}^2/\mathrm{sec}$, which is very good, considering the underestimation of the approximated model by 4%. This value was compared to diffusion coefficients of similar molecules in water because there are no publications with respect to *caged Q-rhodamine dextran*. However, the estimated value lies in the appropriate range.

5.2 Future work

Like many other measurement techniques, the presented MTV images contain projections of a tracer substance that experiences a three-dimensional motion. An appropriate motion model for such experiments has to include the three-dimensional flow field in order to describe it accurately. The computation of such a flow field can be easily accomplished with Gascoigne but the optimization toolbox RoDoBo is not suited to perform computations in three dimensions with a two-dimensional cost function. Major adaptions of the RoDoBo framework have to be made to make it work. A further step towards the realization of the model presented in equation (4.14) involves a forward simulation of the diffusion equation, which can be incorporated into the framework. With this model it is possible to describe the three-dimensional effects and to quantify physical variables on the basis of the entire image sequence for arbitrary domains in x and y.

An important aspect is the regularization of the solution. The applied L^2-regularization can be replaced by higher-order regularizations that are not as restrictive. Tangential or normal derivatives come to mind but also a penalization of the curvature. A multilevel image scheme has to be introduced to overcome the restrictions of the Taylor approximation.

The concept of optimal control in combination with the finite element method brings many potential applications to mind. Rather than limiting the applications to viscous flows, it is possible to use the Navier-Stokes equations as constraints. Especially, the steady Navier-Stokes equation can be used to estimate the average flow from e.g. PIV data, which seems to be advantageous, because for many applications the average velocity component in direction of the camera cancels out. In such cases, a lower-dimensional model can be applied, which speeds up the computation and provides a reasonable representation of the underlying flow.

Instead of using control variables for the estimation of velocity or pressure, the RoDoBo framework allows also to implement control variables with non-linear dependencies. This gives the opportunity to estimate Reynolds numbers or Reynolds shear stresses for a given sequence of PIV images, which are of great interest for the modeling of turbulence. The general framework allows further to include every process that is related - directly or indirectly - to the images. This includes for instance chemical reactions that can be described by PDEs and have an influence on the recorded brightness. An example application are images of fluorescence light, which depend on the concentration of a certain substance that has to be estimated.

FEM computations are very cumbersome, especially in three-dimensions. The RoDoBo framework provides methods that refine the computational meshes according to some cost function. This gives the opportunity to apply numerical simulations on large images because the solution is just estimated with a high resolution where it is necessary. Regions that do not contain useful information can be sparsely sampled in order to gain computational speed and without sacrificing accuracy. This resembles the approaches of Miozzi (2004) and Theunissen (2010), who calculate only estimates where sufficient information exists. These estimates can be included into a fluid motion framework Vlasenko (2010) to estimate reliable solutions based on reliable data samples.

Bibliography

[Adelson and Bergen 1991] Adelson, Edward H. ; Bergen, James R.: The Plenoptic Function and the Elements of Early Vision. In: *Computational Models of Visual Processing*, MIT Press, 1991, p. 3–20 (Cited on page 21.)

[Adrian 1991] Adrian, Ronald J.: Particle-Imaging Techniques for Experimental Fluid Mechanics. In: *Annual Review of Fluid mechanics* 23 (1991), p. 281–304 (Cited on pages 3 and 25.)

[Adrian 2005] Adrian, Ronald J.: Twenty years of particle image velocimetry. In: *Exp Fluids* 39 (2005), p. 159–169 (Cited on page 25.)

[Alvarez et al. 1999] Alvarez, Luis ; Weickert, Joachim ; Sánchez, Javier: A scale-space approach to nonlocal optical flow calculations. In: *Lecture Notes in Computer Science* (1999), p. 235–246 (Cited on page 32.)

[Anandan 1989] Anandan, P: A computational framework and an algorithm for the measurement of visual motion. In: *International Journal of Computer Vision* 2 (1989), Nr. 3, p. 283–310 (Not cited.)

[Aris 1955] Aris, R: On the dispersion of a solute in a fluid flowing through a tube. In: *Proc. R. Soc. London Ser. A* 235 (1955), Nr. 1200, p. 67–77 (Cited on page 40.)

[Arnold and Hinsch 1989] Arnold, Wolfgang ; Hinsch, Klaus D.: Parallel optical evaluation of double-exposure records in optical metrology. In: *Applied Optics* 28 (1989), Nr. 4, p. 726–729 (Cited on page 3.)

[Arroyo and Greated 1991] Arroyo, G ; Greated, C: Stereoscopic particle image velocimetry. In: *Measurement Science and Technology* 2 (1991), p. 1181–1186 (Cited on page 26.)

[Astarita 2006] Astarita, Tommaso: Analysis of interpolation schemes for image deformation methods in PIV: effect of noise on the accuracy and spatial resolution. In: *Exp Fluids* 40 (2006), p. 977–987 (Cited on pages 25, 26, and 46.)

[Astarita and Cardone 2005] Astarita, Tommaso ; Cardone, G: Analysis of interpolation schemes for image deformation methods in PIV. In: *Exp Fluids* 38 (2005), p. 233–243 (Cited on page 26.)

[Bab-Hadiashar and Suter 1996] Bab-Hadiashar, A ; Suter, David: Robust optic flow estimation using least median of squares. In: *IEEE International Conference on Image Processing*, 1996, p. 513–516 (Cited on page 34.)

[Batchelor 2000] Batchelor, George K.: *An introduction to fluid dynamics*. Cambridge University Press, 2000. – ISBN 9780521663960 (Cited on page 36.)

[Bau et al. 2001] Bau, H H. ; Zhong, J H. ; Yi, M Q.: A minute magneto hydro dynamic (MHD) mixer. In: *Sensors and Actuators B-Chemical* 79 (2001), Nr. 2-3, p. 207–215 (Cited on page 35.)

[Beauchemin and Barron 1995] Beauchemin, Steven S. ; Barron, John: The computation of optical flow. In: *ACM Computing Surveys* 27 (1995), Nr. 3, p. 433–467 (Cited on page 23.)

[Becker and Braack 2001] Becker, R ; Braack, M: A finite element pressure gradient stabilization for the Stokes equations based on local projections. In: *Calcolo* 38 (2001), Nr. 4, p. 173–199 (Cited on page 20.)

[Becker and Braack 2005] Becker, Roland ; Braack, M: *The finite element toolkit GASCOIGNE*. Institute of Applied Mathematics, University of Heidelberg. 2005. – URL `http://www.gascoigne.de` (Cited on pages 5, 16, and 77.)

[Becker et al. 2005] Becker, Roland ; Meidner, D ; Vexler, Boris: *A C++ library for optimization with stationary and nonstationary PDEs*. Institute of Applied Mathematics, University of Heidelberg. 2005. – URL `http://www.rodobo.org` (Cited on pages 5, 16, and 77.)

[Beebe et al. 2002] Beebe, D ; Mensing, G ; Walker, G: Physics and applications of microfluidics in biology. In: *Annu. Rev. Biomed. Eng.* 4 (2002), p. 261–286 (Cited on page 35.)

[Bigün 2006] Bigün, Josef: *Vision with direction*. Springer-Verlag New York Inc, 2006. – ISBN 9783540273226 (Cited on page 29.)

[Bigün et al. 1991] Bigün, Josef ; Granlund, G H. ; Wiklund, J: Multidimensional orientation estimation with applications to texture analysis and optical flow. In: *IEEE Transactions on pattern analysis and machine intelligence*, 1991, p. 775–790 (Cited on page 29.)

[Black and Anandan 1993] Black, Michael J. ; Anandan, P: A framework for the robust estimation of optical flow. In: *Fourth International Conference on Computer Vision*, IEEE Computer Society Press, 1993, p. 231–236 (Cited on pages 34 and 98.)

[Black and Anandan 1996] Black, Michael J. ; Anandan, P: The robust estimation of multiple motions: Parametric and piecewise-smooth flow fields. In: *Computer Vision and Image Understanding* 63 (1996), Nr. 1, p. 75–104 (Cited on page 104.)

[Borzì et al. 2002] Borzì, Alfio ; Ito, K ; Kunisch, K: An optimal control approach to optical flow computation. In: *Int. J. Numer. Meth. Fluids* 40 (2002), Nr. 1-2, p. 231–240 (Cited on page 4.)

[Braess 2007] Braess, Dietrich: *Finite elements*. Cambridge University Press, 2007. – ISBN 9780521705189 (Cited on pages 19 and 20.)

[Brox et al. 2004] Brox, Thomas ; Bruhn, Andrés ; Papenberg, N ; Weickert, Joachim: High Accuracy Optical Flow Estimation Based on a Theory for Warping. In: *8th European Conference on Computer Vision*. Prague : Springer, 2004, p. 25–36. – ISBN 3540219846 (Cited on pages 3 and 46.)

[Bruhn and Weickert 2006] Bruhn, Andrés ; Weickert, Joachim: A confidence measure for variational optic flow methods. In: *Computational Imaging and Vision* 31 (2006), p. 283 (Cited on page 34.)

[Bruhn et al. 2005] Bruhn, Andrés ; Weickert, Joachim ; Schnörr, Christoph: Lucas/Kanade meets Horn/Schunck: Combining local and global optic flow methods. In: *International Journal of Computer Vision* 61 (2005), Nr. 3, p. 211–231 (Cited on pages 46 and 104.)

[Bruus 2007] Bruus, Henrik: *Theoretical microfluidics*. Oxford University Press, 2007. – ISBN 0199235090 (Cited on pages 35, 44, and 98.)

[Burnett 1936] Burnett, D: The distribution of molecular velocities and the mean motion in a non-uniform gas. In: *Proceedings of the London Mathematical Society* 2 (1936), Nr. 1, p. 382–435 (Cited on page 37.)

[Burt and Adelson 1983] Burt, P ; Adelson, Edward H.: The Laplacian pyramid as a compact image code. In: *IEEE Transactions on Communications* 31 (1983), Nr. 4, p. 532–540 (Cited on page 32.)

[Byerly 1917] Byerly, William E.: *Introduction to the calculus of variations*. Harvard University Press, 1917 (Cited on page 11.)

[Canny 1986] Canny, J: A computational approach to edge detection. In: *IEEE Transactions on pattern analysis and machine intelligence* (1986), p. 679–698 (Cited on page 69.)

[Chang et al. 2000] Chang, Wesley ; Tzebotich, D ; Lee, Luke P. ; Liepmann, Dorian: Blood flow in simple microchannels. In: *1st Annual International IEEE-EMBS Special Topic Conference on Microtechnologies in Medicine & Biology*, IEEE, 2000, p. 311–315. – ISBN 0780366034 (Cited on page 35.)

[Chatwin and Sullivan 1982] Chatwin, P ; Sullivan, P: The effect of aspect ratio on longitudinal diffusivity in rectangular channels. In: *J. Fluid Mech.* 120 (1982), p. 347–358 (Cited on pages 40, 41, and 98.)

[Cheng and Giordano 2002] Cheng, J T. ; Giordano, N: Fluid flow through nanometer-scale channels. In: *Physical Review E* 65 (2002), p. 031206 (Cited on page 37.)

[Corpetti et al. 2006] Corpetti, Thomas ; Heitz, Dominique ; Arroyo, G ; Mémin, Etienne ; Santa-Cruz, A: Fluid experimental flow estimation based on an optical-flow scheme. In: *Exp Fluids* 40 (2006), Nr. 1, p. 80–97 (Cited on page 3.)

[Corpetti et al. 2002] Corpetti, Thomas ; Mémin, Etienne ; Pérez, Patrick: Dense Estimation of Fluid Flows. In: *IEEE Transactions on pattern analysis and machine intelligence* 24 (2002), Nr. 3, p. 365–380 (Cited on pages 3 and 32.)

[Curtin et al. 2006] Curtin, Damian M. ; Newport, David T. ; Davies, Mark R.: Utilising μ-PIV and pressure measurements to determine the viscosity of a DNA solution in a microchannel. In: *Experimental Thermal and Fluid Science* 30 (2006), Nr. 8, p. 843–852 (Cited on page 60.)

[Day 1990] Day, Michael A.: The No-Slip Condition of Fluid Dynamics. In: *Erkenntnis* 33 (1990), Nr. 3, p. 285–296 (Cited on page 37.)

[Derpanis 2006] Derpanis, K G.: Characterizing image motion. York University, Toronto, Ontario, Canada, 2006. – Tech. report (Cited on page 23.)

[Doshi and Bors 2010] Doshi, Ashish ; Bors, Adrian G.: Robust Processing of Optical Flow of Fluids. In: *IEEE Transactions on Image Processing* 19 (2010), Nr. 9, p. 2332–2344 (Cited on page 33.)

[Doshi and Bors 2007] Doshi, Ashish ; Bors, AG: Navier-Stokes formulation for modelling turbulent optical flow. In: *Proceedings of the British Machine Vision Conference*, BMVC, 2007, p. 1–10 (Cited on page 4.)

[Doshi et al. 1978] Doshi, Mahendra R. ; Daiya, Pankaj M. ; Gill, William N.: Three dimensional laminar dispersion in open and closed rectangular conduits. In: *Chemical Engineering Science* 33 (1978), Nr. 7, p. 795–804 (Cited on page 40.)

[Duffy 2009] Duffy, Austen C.: An Introduction to Gradient Computation by the Discrete Adjoint Method. Florida State University, 2009. – Tech. report (Cited on page 15.)

[Durst et al. 1981] Durst, F ; Melling, A ; Whitelaw, James H.: *Principles and practice of laser-Doppler anemometry*. 2. Academic Press, 1981 (Cited on page 39.)

[Einstein 1906] Einstein, A: Eine neue Bestimmung der Moleküldimensionen. In: *Annalen der Physik* 19 (1906), p. 289–306 (Cited on page 38.)

[Einstein 1911] Einstein, A: Berichtigung zu meiner Arbeit: „Eine neue Bestimmung der Moleküldimensionen". In: *Annalen der Physik* 34 (1911), p. 591–592 (Cited on page 39.)

[Einstein 1905] Einstein, Albert: Über die von der molekularkinetischen Theorie der Wärme geforderte Bewegung von in ruhenden Flüssigkeiten suspendierten Teilchen. In: *Annalen der Physik* 322 (1905), Nr. 8, p. 549–560. ISBN 9783817132072 (Cited on page 65.)

[Elman et al. 2005] Elman, Howard C. ; Silvester, David J. ; Wathen, Andrew J.: *Finite elements and fast iterative solvers*. Oxford University Press, USA, 2005. – ISBN 9780198528685 (Cited on page 20.)

[Elsinga 2008] Elsinga, Gerrit E.: *Tomographic particle image velocimetry and its application to turbulent boundary layers*, Technical University Delft, PhD Thesis, 2008 (Cited on page 26.)

[Elsinga et al. 2006] Elsinga, Gerrit E. ; Scarano, Fulvio ; Wieneke, Bernhard ; Oudheusden, BW v.: Tomographic particle image velocimetry. In: *Exp Fluids* 41 (2006), p. 933–947 (Cited on page 26.)

[Evans 1998] Evans, L.C.: *Partial differential equations*. American Mathematical Society, 1998. – ISBN 0821807722 (Cited on pages 17 and 19.)

[Fieguth 2010] Fieguth, Paul: *Statistical Image Processing and Multidimensional Modeling*. Springer Verlag, 2010. – ISBN 9781441972934 (Cited on pages 54 and 101.)

[Fritzsche 2012] Fritzsche, W: *Optical nano-and microsystems for bioanalytics*. Springer, 2012. – ISBN 978-3-642-25497-0 (Cited on page 35.)

[Garbe et al. 2008] Garbe, C.S. ; Roetmann, Karsten ; Beushausen, V ; Jähne, Bernd: An optical flow MTV based technique for measuring microfluidic flow in the presence of diffusion and Taylor dispersion. In: *Exp Fluids* 44 (2008), Nr. 3, p. 439–450 (Cited on pages 39 and 62.)

[Gateaux 1919] Gateaux, René: Fonctions d'une infinité de variables indépendantes. In: *Bulletin de la Société Mathématique de France* 47 (1919), p. 70–96 (Cited on page 9.)

[Gee et al. 2001] Gee, KR ; Weinberg, ES ; Kozlowski, DJ: Caged Q-rhodamine dextran: a new photoactivated fluorescent tracer. In: *Bioorganic & Medicinal Chemistry Letters* 11 (2001), Nr. 16, p. 2181–2183 (Cited on page 40.)

[Gendrich and Koochesfahani 1996] Gendrich, CP ; Koochesfahani, MM: A spatial correlation technique for estimating velocity fields using molecular tagging velocimetry (MTV). In: *Exp Fluids* 22 (1996), Nr. 1, p. 67–77 (Cited on page 39.)

[Gennert and Negahdaripour 1987] Gennert, MA ; Negahdaripour, S: Relaxing the brightness constancy assumption in computing optical flow. In: *A.I. MIT Memo* 975 (1987) (Cited on page 3.)

[Gharib et al. 2002] Gharib, M. ; Kremers, D ; Koochesfahani, Manoochehr M. ; Kemp, M: Leonardo's vision of flow visualization. In: *Exp Fluids* 33 (2002), Nr. 1, p. 219–223 (Cited on page 3.)

[Girault and Raviart 1986] Girault, Vivette ; Raviart, Pierre-Arnaud: *Finite Element Methods for Navier-Stokes Equations*. Springer Verlag, 1986. – ISBN 3-540-15796-4 (Cited on page 20.)

[Gockenbach 2006] Gockenbach, Mark S.: *Understanding and Implementing the Finite Element Method*. SIAM, 2006. – ISBN 9780898716146 (Cited on page 20.)

[Goldstein 1938] Goldstein, Sydney: *Modern Development in Fluid Dynamics*. Clarendon Press Oxford, 1938. – ISBN 500344819 (Cited on page 37.)

[Gregor et al. 2005] Gregor, T ; Bialek, W ; Steveninck, R R. van ; Tank, D W. ; Wieschaus, E F.: Diffusion and scaling during early embryonic pattern formation. In: *Proceedings of the National Academy of Sciences of the United States of America* 102 (2005), Nr. 51, p. 18403–18407 (Cited on pages 60 and 66.)

[Gunzburger 2003] Gunzburger, Max D.: *Perspectives in flow control and optimization*. Society for Industrial Mathematics, 2003. – ISBN 9780898715279 (Cited on page 12.)

[Hadamard 1902] Hadamard, Jacques: Sur les problèmes aux dérivées partielles et leur signification physique. In: *Princeton University Bulletin* 13 (1902), p. 49–52 (Cited on page 22.)

[Haller 1977] Haller, W: Critical permeation size of dextran molecules. In: *Macromolecules* 10 (1977), Nr. 1, p. 83–86 (Cited on page 40.)

[Hardt and Schönfeld 2007] Hardt, Steffen ; Schönfeld, Friedhelm: *Microfluidic Technologies for Miniaturized Analysis Systems*. Springer Science+Business Media, 2007. – ISBN 9780387684246 (Cited on page 35.)

[Haußecker and Fleet 2001] Haussecker, HW ; Fleet, David J.: Computing optical flow with physical models of brightness variation. In: *IEEE Transactions on pattern analysis and machine intelligence* 23 (2001), Nr. 6, p. 661–673 (Cited on pages 3 and 32.)

[Heuser 2009] Heuser, Harro: *Lehrbuch der Analysis*. Vieweg+ Teubner Verlag, 2009. – ISBN 383480777X (Cited on page 9.)

[Heywood et al. 1996] Heywood, JG ; Rannacher, Rolf ; Turek, S: Artificial boundaries and flux and pressure conditions for the incompressible Navier-Stokes equations. In: *Int. J. Numer. Meth. Fluids* 22 (1996), Nr. 5, p. 325–352 (Cited on page 55.)

[Hinsch 2002] Hinsch, K: Holographic particle image velocimetry. In: *Meas. Sci. Technol* 13 (2002), p. R61–R72 (Cited on page 26.)

[Horn 1986] Horn, B K P.: *Robot Vision*. MIT Press, 1986. – ISBN 9780262081597 (Cited on pages 3 and 28.)

[Horn and Schunck 1981] Horn, B K P. ; Schunck, B G.: Determining Optical Flow. In: *Artificial Intelligence* 17 (1981), p. 185–203 (Cited on pages 3, 30, and 31.)

[Huang et al. 1993a] Huang, HT ; Fiedler, HE ; Wang, JJ: Limitation and Improvement of Piv .1. Limitation of Conventional Techniques Due to Deformation of Particle Image Patterns. In: *Exp Fluids* 15 (1993), Nr. 3, p. 168–174 (Cited on page 26.)

[Huang et al. 1993b] Huang, HT ; Fiedler, HE ; Wang, JJ: Limitation and Improvement of Piv .2. Particle Image Distortion, a Novel Technique. In: *Exp Fluids* 15 (1993), p. 263–273 (Cited on page 26.)

[Huang et al. 2013] Huang, Jian Y. ; Lo, Yu-Chieh ; Niu, Jun J. ; Kushima, Akihiro ; Qian, Xiaofeng ; Zhong, Li ; Mao, Scott X. ; Li, Ju: Nanowire liquid pumps. In: *Nature Nanotechnology* 8 (2013), p. 277–281 (Cited on page 1.)

[Jähne 2006] Jähne, Bernd: *Digitale Bildverarbeitung*. 6. Berlin : Springer, 2006. – ISBN 3-540-24999-0 (Cited on pages 23 and 29.)

[Joseph and Tabeling 2005] Joseph, P ; Tabeling, P: Direct measurement of the apparent slip length. In: *Physical Review E* 71 (2005), p. 035303(R) (Cited on pages 37, 54, and 78.)

[Kähler and Kompenhans 2000] Kähler, Christian J. ; Kompenhans, Jürgen: Fundamentals of multiple plane stereo particle image velocimetry. In: *Exp Fluids* 29 (2000), p. S70–S77 (Cited on page 26.)

[Karniadakis et al. 2005] Karniadakis, George E. ; Beskok, Ali ; Aluru, Narayana R.: *Microflows and nanoflows: fundamentals and simulation*. Springer Science, 2005. – ISBN 0387286764 (Cited on pages 35, 37, and 38.)

[Keane and Adrian 1990] Keane, RD ; Adrian, Ronald J.: Optimization of particle image velocimeters. Part I: Double pulsed systems. In: *Proceedings of SPIE* 1 (1990), p. 1202–1215 (Cited on pages 3 and 25.)

[Keane and Adrian 1992] Keane, RD ; Adrian, Ronald J.: Theory of cross-correlation analysis of PIV images. In: *Applied Scientific Research* 49 (1992), Nr. 3, p. 191–215 (Cited on page 25.)

[Kirby 2010] Kirby, Brian: *Micro- and Nanoscale Fluid Mechanics*. Cambridge University Press, 2010. – ISBN 9780521119030 (Cited on pages 35 and 39.)

[Koochesfahani 1999] Koochesfahani, Manoochehr M.: Molecular tagging velocimetry (MTV): progress and applications. In: *AIAA Paper* (1999), p. 99–3786 (Cited on page 39.)

[Koochesfahani and Nocera 2007] Koochesfahani, Manoochehr M. ; Nocera, Daniel: Molecular tagging velocimetry. In: Foss, John F. (Editor.) ; Tropea, Cameron (Editor.) ; Yarin, Alexander L. (Editor.): *Handbook of Experimental Fluid Dynamics*. Springer Verlag, 2007, p. 362–382 (Cited on page 39.)

[Ladyzhenskaya 1969] Ladyzhenskaya, Olga A.: *The mathematical theory of viscous incompressible flow*. Gordon & Breach Science Pub, 1969. – ISBN 500304858 (Cited on page 36.)

[Laurent et al. 1976] Laurent, Torvard C. ; Sundelöf, Lars O. ; Wik, K O. ; Wärmegard, Birgitta: Diffusion of dextran in concentrated solutions. In: *European Journal of Biochemistry* 68 (1976), Nr. 1, p. 95–102 (Cited on page 66.)

[Leger et al. 1997] Leger, L ; Hervet, H ; Massey, G ; Durliat, E: Wall slip in polymer melts. In: *Journal of Physics-Condensed Matter* 9 (1997), Nr. 37, p. 7719–7740 (Cited on page 38.)

[Lions 1971] Lions, Jacques L.: *Optimal Control of Systems Governed by Partial Differential Equations*. Springer Verlag, 1971. – ISBN 9783642650260 (Cited on pages 4 and 12.)

[Liou and Fang 2006] Liou, William W. ; Fang, Yichuan: *Microfluid Mechanics*. McGraw Hill Professional, 2006. – ISBN 9780071588881 (Cited on pages 35 and 37.)

[Liu 2009] Liu, Ce: *Beyond Pixels: Exploring New Representations and Applications for Motion Analysis*, Massachusetts Institute of Technology, PhD Thesis, 2009 (Cited on page 46.)

[Liu and Shen 2008] Liu, Tianshu ; Shen, Lixin: Fluid flow and optical flow. In: *J. Fluid Mech.* 614 (2008), p. 253–291 (Cited on pages 3 and 42.)

[Longuet-Higgins and Prazdny 1980] Longuet-Higgins, H C. ; Prazdny, K: The interpretation of a moving retinal image. In: *Proceedings of the Royal Society of London. Series B. Biological Sciences* 208 (1980), Nr. 1173, p. 385–397 (Cited on page 21.)

[Lucas and Kanade 1981] Lucas, B ; Kanade, T: An iterative technique of image registration and its application to stereo. In: *Proceedings of the 7th international joint conference on Artificial intelligence*, Morgan Kaufmann Publishers Inc., 1981, p. 674–679 (Cited on pages 3 and 28.)

[Luttman et al. 2011] Luttman, Aaron ; Bollt, E ; Basnayake, R: A Stream Function Approach to Optical Flow with Applications to Fluid Transport Dynamics. In: *Proceedings in Applied Mathematics and Mechanics* 11 (2011), Nr. 2, p. 855–856 (Cited on page 4.)

[Luttman et al. 2013] Luttman, Aaron ; Bollt, E M. ; Basnayake, R ; Kramer, S ; Tufillarob, N B.: A Framework for Estimating Potential Fluid Flow from Digital Imagery. In: *submitted to Chaos* (2013) (Cited on page 4.)

[Marr and Ullman 1981] Marr, David ; Ullman, Shimon: Directional selectivity and its use in early visual processing. In: *Proceedings of the Royal Society of London. Series B. Biological Sciences* 211 (1981), Nr. 1183, p. 151–180 (Cited on page 28.)

[Maxwell 1878] Maxwell, J C.: On Stresses in Rarefied Gases Arising from Inequalities of Temperature. In: *Proceedings of the Royal Society of London* 27 (1878), Nr. 185-189, p. 304–308 (Cited on page 37.)

[Meidner 2008] Meidner, D: *Adaptive Space-Time Finite Element Methods for Optimization Problems Governed by Nonlinear Parabolic Systems*, University of Heidelberg, PhD Thesis, 2008 (Cited on pages 15 and 16.)

[Meinhart and Zhang 2000] Meinhart, C D. ; Zhang, H: The flow structure inside a microfabricated inkjet printhead. In: *Microelectromechanical Systems, Journal of* 9 (2000), Nr. 1, p. 67–75 (Cited on page 35.)

[Merzkirch 1987] Merzkirch, Wolfgang: *Flow Visualization*. 2nd Edition. Academic Press Inc. (London) LDT., 1987. – ISBN 9780124913516 (Cited on page 2.)

[Meynart 1983] Meynart, Roland: Instantaneous velocity field measurements in unsteady gas flow by speckle velocimetry. In: *Applied Optics* 22 (1983), Nr. 4, p. 535–540 (Cited on page 3.)

[Mhetar and Archer 1998] Mhetar, Vijay ; Archer, L A.: Slip in entangled polymer melts. 1. General features. In: *Macromolecules* 31 (1998), Nr. 24, p. 8607–8616 (Cited on page 38.)

[Miozzi 2004] Miozzi, M: Particle Image Velocimetry using Feature Tracking and Delaunay Tessellation. In: *XII International Symposium on Applications on Laser Techniques to Fluid Mechanics* (2004) (Cited on page 80.)

[Nakajima et al. 2003] Nakajima, Y ; Inomata, H ; Nogawa, H ; Sato, Y ; Tamura, S ; Okazaki, K ; Torii, S: Physics-based flow estimation of fluids. In: *Pattern Recognition* 36 (2003), Nr. 5, p. 1203–1212 (Cited on pages 4, 32, and 33.)

[NASA 1994] NASA: *Wake Vortex Study at Wallops Island, EL-1996-00130*. Langley Research Center (NASA-LaRC). 1994. – URL `http://archive.org/details/NIX-EL-1996-00130`. – Date: May 28th 2013 (Cited on page 1.)

[NASA 2004] NASA: *Astronaut photograph ISS008-E-19646 was taken March 7, 2004*. Earth Observations Laboratory, Johnson Space Center. 2004. – URL `http://earthobservatory.nasa.gov/IOTD/view.php?id=4369`. – Date: 5. April 2013 (Cited on page 1.)

[Nguyen and Wereley 2002] Nguyen, Nam-Trung ; Wereley, Steve T.: *Fundamentals and applications of microfluidics*. Artech House Publishers, 2002. – ISBN 9781580533430 (Cited on pages 35, 38, and 39.)

[Nolen 2009] Nolen, J: Partial Differential Equations and Diffusion Processes. Stanford University, 2009. – Tech. report (Cited on page 100.)

[Paul et al. 1998] Paul, P ; Garguilo, M G. ; Rakestraw, D J.: Imaging of Pressure- and Electrokinetically Driven Flows through Open Capillaries. In: *Analytical Chemistry* 70 (1998), Nr. 13, p. 2459–2467 (Cited on page 39.)

[Press et al. 2002] Press, William H. ; Teukolsky, Saul A. ; Vetterling, William T. ; Flannery, Brian P.: *Numerical Recipes*. Cambridge University Press, 2002. – ISBN 9780521750363 (Cited on page 58.)

[Priezjev 2007] Priezjev, Nikolai V.: Rate-dependent slip boundary conditions for simple fluids. In: *Physical Review E* 75 (2007), Nr. 5, p. 051605 (Cited on page 38.)

[Quénot et al. 1998] Quénot, George M. ; Pakleza, J ; Kowalevski, T: Particle image velocimetry with optical flow. In: *Exp Fluids* 25 (1998), p. 177–189 (Cited on page 3.)

[Quéré 2008] Quéré, David: Wetting and roughness. In: *Annu. Rev. Mater. Res.* 38 (2008), p. 71–99 (Cited on page 38.)

[Raffel et al. 2007] Raffel, Markus ; Willert, Christian E. ; Wereley, Steve T. ; Kompenhans, Jürgen: *Particle image velocimetry: a practical guide*. 2nd Edition. Berlin : Springer, 2007. – ISBN 9783540723073 (Cited on pages 25 and 26.)

[Rannacher 2000] Rannacher, Rolf: Finite element methods for the incompressible Navier-Stokes equations. In: Galdi, P (Editor.) ; Heywood, JG (Editor.) ; Rannacher, Rolf (Editor.): *Fundamental Directions in Mathematical Fluid Mechanics*. Basel, 2000, p. 191–293. – ISBN 3764364149 (Cited on page 55.)

[Roetmann 2008] Roetmann, Karsten: *Entwicklung optischer Feldmessverfahren zur Charakterisierung mikrofluidischer Mischvorgänge*, University of Göttingen, PhD Thesis, 2008 (Cited on pages 1, 39, 64, 66, and 79.)

[Roetmann et al. 2008] Roetmann, Karsten ; Schmunk, W ; Garbe, C.S. ; Beushausen, V: Micro-flow analysis by molecular tagging velocimetry and planar Raman-scattering. In: *Exp Fluids* 44 (2008), Nr. 3, p. 419–430 (Cited on page 39.)

[Ruhnau 2006] Ruhnau, Paul: *Variational Fluid Motion Estimation with Physical Priors*, University of Mannheim, PhD Thesis, 2006 (Cited on pages 4 and 33.)

[Ruhnau and Schnörr 2006] Ruhnau, Paul ; Schnörr, Christoph: Optical Stokes flow estimation: an imaging-based control approach. In: *Exp Fluids* 42 (2006), Nr. 1, p. 61–78 (Cited on pages 4 and 33.)

[Ruhnau et al. 2007] Ruhnau, Paul ; Stahl, A ; Schnörr, Christoph: Variational estimation of experimental fluid flows with physics-based spatio-temporal regularization. In: *Measurement Science and Technology* 18 (2007), Nr. 3, p. 755–763 (Cited on page 4.)

[Samimy et al. 2003] Samimy, M ; Breuer, Kenneth S. ; Leal, L G. ; Steen, P H.: *A Gallery of Fluid Motion*. Cambridge University Press, 2003. – ISBN 9780521535007 (Cited on page 2.)

[Santiago et al. 1998] Santiago, Juan G. ; Wereley, Steve T. ; Meinhart, Carl D. ; Beebe, D ; Adrian, Ronald J.: A particle image velocimetry system for microfluidics. In: *Exp Fluids* 25 (1998), p. 316–319 (Cited on page 39.)

[Scarano 2002] Scarano, Fulvio: Iterative image deformation methods in PIV. In: *Measurement Science and Technology* 13 (2002), p. R1–R19 (Cited on page 26.)

[Scarano and Riethmuller 1999] Scarano, Fulvio ; Riethmuller, Michel L.: Iterative multigrid approach in PIV image processing with discrete window offset. In: *Exp Fluids* 26 (1999), Nr. 6, p. 513–523 (Cited on page 46.)

[Schnörr 1991] Schnörr, Christoph: Determining optical flow for irregular domains by minimizing quadratic functionals of a certain class. In: *International Journal of Computer Vision* 6 (1991), Nr. 1, p. 25–38 (Cited on page 31.)

[Sethian 1999] Sethian, James A.: Fast marching methods. In: *SIAM Review* 41 (1999), Nr. 2, p. 199–235 (Cited on page 70.)

[Silva et al. 2009] Silva, Gonccalo ; Leal, Nuno ; Semiao, Viriato: Determination of microchannels geometric parameters using micro-PIV. In: *Chemical Engineering Research and Design* 87 (2009), Nr. 3, p. 298–306 (Cited on page 53.)

[Sinton 2004] Sinton, D: Microscale flow visualization. In: *Microfluid Nanofluidics* 1 (2004), Nr. 1, p. 2–21 (Cited on page 38.)

[Squires and Quake 2005] Squires, T ; Quake, S: Microfluidics: Fluid physics at the nanoliter scale. In: *Reviews of modern physics* 77 (2005), p. 977–1026 (Cited on pages 35 and 36.)

[Stanislas et al. 2008] Stanislas, Michel ; Okamoto, K ; Kähler, Christian J. ; Westerweel, Jerry ; Scarano, Fulvio: Main results of the third international PIV challenge. In: *Exp Fluids* 45 (2008), Nr. 1, p. 27–71 (Cited on page 26.)

[Stanislas et al. 2003] Stanislas, Michel ; Okamoto, Koji ; Kähler, Christian J.: Main results of the First International PIV Challenge. In: *Meas. Sci. Technol* 14 (2003), p. R63–R89 (Cited on page 26.)

[Stanislas et al. 2005] Stanislas, Michel ; Okamoto, Koji ; Kähler, Christian J. ; Westerweel, Jerry: Main results of the second international PIV challenge. In: *Exp Fluids* 39 (2005), Nr. 2, p. 170–191 (Cited on page 26.)

[Strang 2007] Strang, Gilbert: Applied Mathematics and Scientific Computing. 2007. – URL `http://math.mit.edu/classes/18.086/2006/`. – Date: 25. August 2013 (Cited on page 20.)

[Takenaka et al. 2009] Takenaka, Shoji ; Pitts, Betsey ; Trivedi, Harsh M. ; Stewart, Philip S.: Diffusion of macromolecules in model oral biofilms. In: *Applied and Environmental Microbiology* 75 (2009), Nr. 6, p. 1750–1753 (Cited on page 66.)

[Taylor 1932] Taylor, Geoffrey I.: The viscosity of a fluid containing small drops of another fluid. In: *Proc. R. Soc. London Ser. A* 138 (1932), Nr. 834, p. 41–48 (Cited on page 39.)

[Taylor 1953] Taylor, Geoffrey I.: Dispersion of soluble matter in solvent flowing slowly through a tube. In: *Proc. R. Soc. London Ser. A* 219 (1953), p. 186–203 (Cited on page 40.)

[Temam 1979] Temam, Roger: *Navier-Stokes Equations*. North-Holland Publishing Company, 1979. – ISBN 0720428408 (Cited on page 36.)

[Theunissen 2010] Theunissen, Raf: *Adaptive image interrogation for PIV*, Vrije Universiteit Brussel, Belgium, PhD Thesis, 2010 (Cited on page 80.)

[Thiagarajah et al. 2001] Thiagarajah, J R. ; Pedley, K C. ; Naftalin, R J.: Evidence of amiloride-sensitive fluid absorption in rat descending colonic crypts from fluorescence recovery of FITC-labelled dextran after photobleaching. In: *The Journal of physiology* 536 (2001), Nr. 2, p. 541–553 (Cited on pages 60 and 66.)

[Thomas 1995] Thomas, J W.: *Numerical Partial Differential Equations: Finite Difference Methods*. Springer Verlag, 1995. – ISBN 9780387979991 (Cited on page 59.)

[Tikhonov and Arsenin 1977] Tikhonov, Andrey N. ; Arsenin, Vasily Y.: *Solutions of Ill Posed Problems*. John Wiley & Sons Inc. 1977 (Cited on pages 23, 27, and 30.)

[Trailović and Pao 2005] Trailović, Lidija ; Pao, Lucy Y.: Variance estimation and ranking of target tracking position errors modeled using Gaussian mixture distributions. In: *Automatica* 41 (2005), Nr. 8, p. 1433–1438 (Cited on page 66.)

[Tretheway and Meinhart 2002] Tretheway, D C. ; Meinhart, C D.: Apparent fluid slip at hydrophobic microchannel walls. In: *Physics of Fluids* 14 (2002), p. L9–L12 (Cited on page 38.)

[Tröltzsch 2009] Tröltzsch, F: *Optimale Steuerung partieller Differentialgleichungen*. Vieweg + Teubner, 2009. – ISBN 9783834808851 (Cited on pages 4, 12, and 15.)

[Tropea et al. 2007] Tropea, Cameron ; Yarin, Alexander L. ; Foss, John F.: *Springer Handbook of Experimental Fluid Mechanics*. Springer, 2007. – ISBN 9783540251415 (Cited on page 38.)

[Tveito and Winther 2005] Tveito, Aslak ; Winther, Ragnar: *Introduction to partial differential equations*. Springer Verlag, 2005. – ISBN 9783540225515 (Cited on pages 17 and 100.)

[Uras et al. 1988] Uras, S ; Girosi, F ; Verri, A: A computational approach to motion perception. In: *Biological Cybernetics* 60 (1988), p. 79–87 (Cited on page 3.)

[Verpoorte 2002] Verpoorte, E: Microfluidic chips for clinical and forensic analysis. In: *Electrophoresis* 23 (2002), p. 677–712 (Cited on page 35.)

[Vlasenko and Schnörr 2008] Vlasenko, A ; Schnörr, Christoph: Physically consistent variational denoising of image fluid flow estimates. In: *Lecture Notes in Computer Science* 5096 (2008), p. 406–415 (Cited on page 33.)

[Vlasenko 2010] Vlasenko, Andrey: *Physics-Based Fluid Flow Restoration Method*, University of Heidelberg, Germany, PhD Thesis, 2010 (Cited on page 80.)

[Weickert and Schnörr 2001a] Weickert, Joachim ; Schnörr, Christoph: A theoretical framework for convex regularizers in PDE-based computation of image motion. In: *International Journal of Computer Vision* 45 (2001), Nr. 3, p. 245–264 (Cited on page 104.)

[Weickert and Schnörr 2001b] Weickert, Joachim ; Schnörr, Christoph: Variational Optic Flow Computation with a Spatio-Temporal Smoothness Constraint. In: *Journal of Mathematical Imaging and Vision* 14 (2001), p. 245–255 (Cited on page 104.)

[Werlberger et al. 2009] Werlberger, M ; Trobin, W ; Pock, T ; Wedel, A ; Cremers, D ; Bischof, H: Anisotropic Huber-L1 optical flow. 34 (2009), p. 1–11 (Cited on page 104.)

[Westerweel et al. 1997] Westerweel, Jerry ; Dabiri, D ; Gharib, Morteza: The effect of a discrete window offset on the accuracy of cross-correlation analysis of digital PIV recordings. In: *Exp Fluids* 23 (1997), p. 20–28 (Cited on page 26.)

[Westerweel and Scarano 2005] Westerweel, Jerry ; Scarano, Fulvio: Universal outlier detection for PIV data. In: *Exp Fluids* 39 (2005), p. 1096–1100 (Cited on page 33.)

[White 1991] White, Frank M.: *Viscous fluid flow.* McGraw-Hill, 1991. – ISBN 9780070697126 (Cited on page 98.)

[Wiener 1930] Wiener, Norbert: Generalized harmonic analysis. In: *Acta mathematica* 55 (1930), Nr. 1, p. 117–258 (Cited on page 100.)

[Wildes et al. 1997] Wildes, Richard P. ; Lanzillotto, A M. ; Amabile, M J. ; Leu, Tzong-Shyng: Physically based fluid flow recovery from image sequences. In: *IEEE Computer Society Conference on Computer Vision and Pattern Recognition*, IEEE, 1997, p. 969–975. – ISBN 0818678224 (Cited on pages 3 and 32.)

[Willert and Gharib 1991] Willert, Christian E. ; Gharib, Morteza: Digital particle image velocimetry. In: *Exp Fluids* 10 (1991), p. 181–193 (Cited on pages 3 and 25.)

[Wright and Nocedal 1999] Wright, S. ; Nocedal, J.: *Numerical Optimization.* Springer, Berlin, 1999. – ISBN 0-387-98793-2 (Cited on pages 14 and 17.)

[Xu and Li 2004] Xu, Kun ; Li, Zhihui: Microchannel flow in the slip regime: gas-kinetic BGK–Burnett solutions. In: *J. Fluid Mech.* 513 (2004), Nr. 1, p. 87–110 (Cited on page 38.)

[Yager et al. 2006] Yager, P ; Edwards, T ; Fu, E ; Helton, K ; Nelson, K ; Tam, Milton R. ; Weigl, Bernhard H.: Microfluidic diagnostic technologies for global public health. In: *Nature* 442 (2006), p. 412–418 (Cited on page 35.)

Appendix

A.1 Nondimensional Navier-Stokes equation

The Navier-Stokes equations give a general description of physical flow phenomena in a continuum and read

$$\rho\left(\partial_t \boldsymbol{u} + (\boldsymbol{u}^T\nabla)\boldsymbol{u}\right) = -\nabla p + \mu\Delta\boldsymbol{u} + \boldsymbol{f}\,. \tag{A.1}$$

All variables in this non-linear PDE have units, which is inconvenient for running simulations. In order to allow a general analysis of the equations, all dimensional quantities and operators can be expressed as multiples of flow specific quantities, such as a length scale ℓ and a time scale T or a velocity scale U. Since the velocity can be expressed by a time and length scale, it is just necessary to define two out of the three. The third scale is then already determined. The variables and differential operators are scaled in the following way:

$$\begin{array}{llllll} \boldsymbol{u} & = \boldsymbol{u}^* \cdot U & , \quad \boldsymbol{x} & = \boldsymbol{x}^* \cdot \ell & , \quad p = p^*\rho \cdot U^2\,, \\ \nabla & = \frac{1}{\ell}\nabla^* & , \quad \partial_t & = \frac{1}{T}\partial_t^* = \frac{U}{\ell}\partial_t^* & . \end{array} \tag{A.2}$$

These identities are used to substitute the variables in equation (A.1) which gives the equation

$$\rho U\frac{U}{\ell}\partial_t^*\boldsymbol{u}^* + \rho\frac{U^2}{\ell}(\boldsymbol{u}^{*T}\nabla^*)\boldsymbol{u}^* = -\nabla^* p^*\frac{U^2\rho}{\ell} + \mu\frac{U}{\ell^2}\nabla^{*2}\boldsymbol{u}^* + \frac{\ell}{U^2}\boldsymbol{f}\,. \tag{A.3}$$

The dimensional variables can be reordered in such a way, that they appear in just two terms

$$\partial_t^*\boldsymbol{u}^* + (\boldsymbol{u}^{*T}\nabla^*)\boldsymbol{u}^* = -\nabla^* p^* + \underbrace{\frac{\nu}{U\ell}}_{=\frac{1}{\mathrm{Re}}}\nabla^{*2}\boldsymbol{u}^* + \frac{\ell}{U^2}\boldsymbol{f}\,. \tag{A.4}$$

The two new variables are the Reynolds number $\mathrm{Re} = \frac{\rho U \ell}{\mu}$ and if $\boldsymbol{f}$ is a gravitational force, the Froud number $\mathrm{Fr} = \frac{U^2}{\ell g}$. If no body force $\boldsymbol{f}$ acts on the fluid, all dimensional variables are bundled in the nondimensional Reynolds number, which is the ration of inertial forces to viscous forces. This means, that if the geometries of two flow phenomena are similar up to a scaling factor and the Reynolds numbers are the same, then the motion of both flow phenomena is the identical. This is a crucial statement, because it allows to scale the geometry of the flow domain and to get the unscaled result, assuming the Reynolds number is equal.

A.2 Nondimensional diffusion equation

As shown in previous paragraph for the momentum equation of the flow, the diffusion equation

$$\partial_t \rho + (\boldsymbol{u}^T \nabla)\rho = -\kappa \Delta \rho \tag{A.5}$$

can be nondimensionalized in the same manner. By introducing a reference density ρ_{ref} and expressing the density as $\rho = \rho^* \rho_{ref}$ allows to substitute the variables in equation (A.5). This yields

$$\frac{U\rho_{ref}}{\ell}\partial_t^* \rho' + \frac{U\rho_{ref}}{\ell}(\boldsymbol{u}^{*T}\nabla^*)\rho^* = \kappa \frac{\rho_{ref}}{v^2}\Delta' \rho' \tag{A.6}$$

$$\tag{A.7}$$

and again it is possible to reorder all dimensional variables into one term. The nondimensional formulation of the diffusion equation reads

$$\partial_t^* \rho^* + (\boldsymbol{u}^{*T}\nabla^*)\rho^* = \underbrace{\frac{\kappa}{\ell U}}_{=\frac{1}{Pe}} \Delta^* \rho^* \,, \tag{A.8}$$

where the Péclet number Pe is the ratio between the advective and the diffusive transport.

A.3 Solution of the Stokes equation in a rectangular channel

The geometry of a rectangular channel is sufficiently regular, so that an analytical solution of the motion can be derived. However, since the border of the domain is not smooth at all, the only chance is to develop the solution into a series. The Navier-Stokes equations simplify under the assumption of a steady flow ($\partial_t \boldsymbol{u} = 0$), a negligible advection ($\boldsymbol{u}^T \nabla \boldsymbol{u} \ll \frac{1}{\mathrm{Re}} \Delta \boldsymbol{u}$) and a purely streamwise motion to a one-dimensional Stokes equations of the form

$$\frac{1}{\mathrm{Re}} \Delta u = \partial_x p \,. \tag{A.9}$$

The pressure derivative can be replaced by the pressure drop over the length of the channel $\partial_x p = \frac{\delta p}{\ell}$. The motion can be expanded into a Fourier series over the rectangular y-z-domain and reads

$$u = \sum_{n=1}^{\infty} \sum_{m=1}^{\infty} u_{nm} \sin(n\frac{\pi}{W}y) \sin(m\frac{\pi}{H}z)\,, \tag{A.10}$$

where W is the width and H is the height of the channel. This ansatz function has to fulfill the boundary conditions, which are assumed to be of *no-slip* type. This yields the four identities

$$0 = u\big|_{y=0} = \sum_{n=1}^{\infty} \sum_{m=1}^{\infty} u_{nm} \sin(m\frac{\pi}{H}z) \tag{A.11}$$

$$0 = u\big|_{y=W} = \sum_{n=1}^{\infty} \sum_{m=1}^{\infty} u_{nm} \sin(n\pi) \sin(m\frac{\pi}{H}z) \tag{A.12}$$

$$0 = u\big|_{z=0} = \sum_{n=1}^{\infty} \sum_{m=1}^{\infty} u_{nm} \sin(n\frac{\pi}{W}y) \tag{A.13}$$

$$0 = u\big|_{z=H} = \sum_{n=1}^{\infty} \sum_{m=1}^{\infty} u_{nm} \sin(n\frac{\pi}{W}y) \sin(m\pi)\,. \tag{A.14}$$

The right hand side $\frac{\delta p}{\ell}$ can also be expanded into a Fourier series in both coordinates. Since it is independent of y and z, the identity function has to be expanded

$$\mathbb{1} = \sum_{n=1}^{\infty} a_n \cos(n\frac{\pi}{W}y) + b_n \sin(n\frac{\pi}{W}y)\,. \tag{A.15}$$

The coefficients a_n and b_n are calculated by the scalar product with of $\mathbb{1}$ with the basis functions. Therefore, the following constraints must be satisfied

$$a_n = \frac{2}{W} \int_0^W \cos(n\frac{\pi}{W}y)\mathrm{d}y = \frac{2}{n\pi} \left[\sin(n\frac{\pi}{W}y)\right]_0^W \tag{A.16}$$

$$b_n = \frac{2}{W} \int_0^W \sin(n\frac{\pi}{W}y)\mathrm{d}y = -\frac{2}{n\pi} \left[\cos(n\frac{\pi}{W}y)\right]_0^W\,. \tag{A.17}$$

The first condition (A.16) is always zero, which means that just sine functions are needed to expand the identity function. The second coefficient b_n is zero for even n and $\frac{4}{\pi n}$ for odd n. The very same procedure can be done for the dependency of the z-coordinate so that the right hand side can be written as

$$\frac{\delta p}{\ell} = -\frac{\delta p}{\ell} \frac{16}{\pi^2} \sum_{\text{odd } n,m} \frac{1}{nm} \sin(n\frac{\pi}{W}y) \sin(n\frac{\pi}{H}z)\,. \tag{A.18}$$

Putting the Fourier series of the left hand side (A.10) in the equation requires to calculate its Laplacian. The entire equation as Fourier series reads

$$\begin{aligned} -\pi^2 \sum_{n=1}^{\infty} \sum_{m=1}^{\infty} \left(\frac{n^2}{W} + \frac{m^2}{H} \right) u_{nm} \sin(n\frac{\pi}{W}y) \sin(m\frac{\pi}{H}z) \\ = -\frac{\delta p}{\ell} \frac{16}{\pi^2} \sum_{\text{odd } n,m} \frac{1}{nm} \sin(n\frac{\pi}{W}y) \sin(n\frac{\pi}{H}z) \,. \end{aligned} \tag{A.19}$$

Since the basis functions are identical, it is possible to compare the coefficients at both sides to get to the expression

$$u_{nm} = \frac{16}{\pi^4} \frac{\delta p}{L} \frac{1}{nm \left(\frac{n^2}{W^2} + \frac{m^2}{H^2} \right)} \,. \tag{A.20}$$

Putting now all together yields the solution presented in equation (4.7)

$$u(y,z) = \frac{16}{\pi^4} \frac{(p_{out} - p_{in})}{\mu L} \sum_{odd\ n,m}^{\infty} \frac{1}{\left(\frac{n^2}{W^2} + \frac{m^2}{H^2} \right) nm} \sin\left(n\frac{\pi}{W}y \right) \sin\left(m\frac{\pi}{H}z \right) \,. \tag{A.21}$$

Similar derivations can be found in White (1991), (Bruus, 2007, p. 48) and Chatwin and Sullivan (1982).

A.4 Correct norm for Gaussian noise

Black and Anandan (1993) investigated robust norms to improve the performance of optical flow algorithms. The standard L^2-norm is widely used because it renders the data term convex, which allows the application of many efficient optimization techniques. The L^2-norm penalizes extreme outliers disproportionately because they contribute quadratically to the costs. This can corrupt the estimation of all statistical moments. On the other hand, data points close to the average are difficult to improve because they contribute hardly to the costs. The following argument demonstrates that the L^2-norm is the appropriate choice in case of Gaussian noise.

Theorem 1. Assuming that two images I_1 and I_2 can be related by

$$I_2(\boldsymbol{x}) = I_1(\boldsymbol{x} + \boldsymbol{u}) + noise(\boldsymbol{x}) \tag{A.22}$$

where $noise(\boldsymbol{x}) \propto \mathcal{N}(0, \sigma)$, $\forall i \in \Omega$ is Gaussian noise with zero mean and variance σ. The noise is assumed to be independently and identically distributed for each pixel. Then the Euclidean norm is the correct norm to estimate the deviation and $\|I_2 - I_1\|_\Omega$ is the corresponding error.

Proof: The probability distribution function (pdf) for the noise is a Gaussian function of the form

$$\mathrm{pdf}(N, \boldsymbol{x}) = \frac{1}{\sqrt{2\pi}\sigma} \exp\left(-\frac{\varepsilon^2(\boldsymbol{x})}{2\sigma^2}\right), \tag{A.23}$$

where $\varepsilon^2(\boldsymbol{x}) = (I_2(\boldsymbol{x}) - I_1(\boldsymbol{x}))^2$ is the deviation of the model to the measurement. This implies that the pdf for $I_2(\boldsymbol{x})$ given $I_1(\boldsymbol{x})$ dependents on $\boldsymbol{u}(\boldsymbol{x})$ and can be formulated as conditional pdf

$$\mathrm{pdf}(I_2|I_1; \boldsymbol{u}, \boldsymbol{x}) = \frac{1}{\sqrt{2\pi}\sigma} \exp\left(-\frac{(I_2(\boldsymbol{x}) - I_1(\boldsymbol{x}+\boldsymbol{u}))^2}{2\sigma^2}\right), \tag{A.24}$$

which is valid for each pixel. The likelihood function $\mathscr{L}$ describes the probability of the image I_2 given the image I_1 and the velocity field $\boldsymbol{u}$. Since each pixel has independent noise, the joint pdf for the image factorizes into a product of the individual pixel pdfs. The likelihood reads

$$\mathscr{L}(\boldsymbol{u}) = \prod_{\boldsymbol{x}\in\Omega} \mathrm{pdf}(I_2|I_1; \boldsymbol{u}, \boldsymbol{x}) \tag{A.25}$$

in which the Gaussian pdf model can be substituted to get the relation

$$\mathscr{L}(\boldsymbol{u}) = \prod_{\boldsymbol{x}\in\Omega} \frac{1}{\sqrt{2\pi}\sigma} \exp\left(-\frac{(I_2(\boldsymbol{x}) - I_1(\boldsymbol{x}+\boldsymbol{u}))^2}{2\sigma^2}\right). \tag{A.26}$$

The multiplication of individual but identically distributed pdfs can be assimilated into the exponential function and turns into a summation

$$\left(\frac{1}{\sqrt{2\pi}\sigma}\right)^N \exp\left(-\sum_{\boldsymbol{x}\in\Omega} \frac{(I_2(\boldsymbol{x}) - I_1(\boldsymbol{x}+\boldsymbol{u}))^2}{2\sigma^2}\right). \tag{A.27}$$

The most probable image I_2 given the first image I_1 can be found by maximizing the likelihood function $\mathscr{L}$ with respect to the motion estimation $\boldsymbol{u}$. The problem of maximizing a Gaussian function corresponds to minimizing its argument. Therefore, the problem is to solve

$$\arg\max_{\boldsymbol{u}} \mathscr{L}(\boldsymbol{u}) \equiv \arg\min_{\boldsymbol{u}} \sum_{\boldsymbol{x}\in\Omega} (I_2(\boldsymbol{x}) - I_1(\boldsymbol{x}+\boldsymbol{u}))^2,$$

which corresponds to the Euclidean norm. This means that for regession problems with Gaussian noise, the L^2-norm is the norm that yields the most likely estimates.

A.5 Equivalence of diffusion and kernel convolution

Solving for the evolution of diffusive effects requires computing partial differential equations. Rather than solving PDEs, there is an alternative approach to compute the diffusion via the fundamental solution of the diffusion equation (Tveito and Winther, 2005, p. 375ff; Nolen, 2009, p. 14ff).

Theorem 2. Diffusive processes can be described as a convolution of the initial state of the system with the fundamental solution of the diffusion equation, which is a time-dependent Gaussian function

Proof: Let $\rho : \mathbb{R}^n \times T \to \mathbb{R}$ be a scalar density function whose temporal evolution can be described by the parabolic diffusion equation

$$\partial_t \rho = \kappa \Delta \rho \tag{A.28}$$

$$\rho(\boldsymbol{x}, 0) = \rho_0(\boldsymbol{x}) \tag{A.29}$$

where ρ_0 is the initial density at time $t = 0$. The second-order PDE can be transformed into the Fourier space with respect to its spatial coordinates ($\boldsymbol{x} \to \boldsymbol{k}$), which yields

$$\partial_t \tilde{\rho} = -\kappa \boldsymbol{k}^T \boldsymbol{k} \tilde{\rho} \,. \tag{A.30}$$

This equation can be easily solved by the separation of the variable and gives already the solution in frequency domain

$$\tilde{\rho} = \tilde{\rho}_0 \exp(-\kappa \boldsymbol{k}^T \boldsymbol{k} t) \,. \tag{A.31}$$

This product can be seen as a multiplication of two frequency spectra, $\tilde{\rho}_0$ and $\exp(-\kappa |\boldsymbol{k}|^2 t)$. According to the Wiener-Kinchin-Theorem (Wiener, 1930) this product equals a convolution of the initial Intensity ρ_0 with a fundamental diffusion solution (Gauss-Weierstrass-Kernel). This solution is the Fourier transform of the above Gaussian function and reads

$$\Phi(\boldsymbol{x}, t) = \frac{1}{(4\pi\kappa t)^{n/2}} \exp\left(-\frac{|\boldsymbol{x}|^2}{4\kappa t}\right) . \tag{A.32}$$

The time-evolved state of the density ρ can then be determined by the convolution product

$$\rho(\boldsymbol{x}, t) = \Phi(\boldsymbol{x}, t) * \rho_0(\boldsymbol{x}) \,. \tag{A.33}$$

A.6 Relation between 3D and 2D diffusion

Photographic images provide just projections of physical phenomena. It has to be clarified that the diffusion coefficients, which are estimated from projections,

are equivalent to the diffusion coefficients determined from the three-dimensional phenomenon. Therefore, it has to be shown that the projection operator $\hat{P}^{\downarrow}$ does not alter the diffusion coefficient κ.

Without loss of generality, it can be assumed that the operator $\hat{P}^{\downarrow}$ projects the z coordinate to zero and has no effect on the other coordinates. Applying $\hat{P}^{\downarrow}$ to the general time-dependent solution from (A.32) allows to change the order of integration

$$\begin{aligned}\hat{P}^{\downarrow}\rho(\boldsymbol{x},t) &= \int_{-\infty}^{\infty} \Phi(\boldsymbol{x},t) * \rho_0(\boldsymbol{x})\mathrm{d}z \\ &= \iiiint_{-\infty}^{\infty} \Phi(\boldsymbol{x}-\boldsymbol{x}',t)\rho_0(\boldsymbol{x}')\mathrm{d}x'\mathrm{d}z \\ &= \frac{1}{\sqrt{4\pi\kappa t}^3} \iiiint_{-\infty}^{\infty} \exp\left(-\frac{|\boldsymbol{x}-\boldsymbol{x}'|^2}{4\kappa t}\right)\rho_0(\boldsymbol{x}')\mathrm{d}\boldsymbol{x}'\mathrm{d}z\,.\end{aligned} \tag{A.34}$$

The two integrations over the z-direction can be easily done because of the modest nature of Gaussian functions and with the assumption of a uniformly distributed density over the height. It gives the factor $\sqrt{4\pi\kappa t}$, which cancels with the existing factor in front of the integral. However, the remaining equation is equivalent to the convolution of a two-dimensional diffusion on a projected density

$$\hat{P}^{\downarrow}\rho(\boldsymbol{x},t) = \frac{1}{\sqrt{4\pi\kappa t}^2} \iint_{-\infty}^{\infty} \exp\left(-\frac{|\boldsymbol{x}-\boldsymbol{x}'|^2}{4\kappa t}\right)(\hat{P}^{\downarrow}\rho_0)(\boldsymbol{x}')\mathrm{d}\boldsymbol{x}'\,. \tag{A.35}$$

This shows once more again, that diffusion is separable in all spatial dimensions and can be treated independently. Of course, the identity in equation (A.35) is just valid if the integration is done over the entire $\mathbb{R}$. However, since borders effects have to be taken into consideration, this equation is certainly valid for the bulk, where the distance to the border is larger than $\sqrt{2n\kappa t}$. For small times $t \ll 1$ this relation is nearly satisfied in entire domain.

A.7 Dependency of the image structure on the control

The boundary controlled PDE motion estimation is highly dependent on the image data. Figure A.1 shows the results that were obtained with three different images. All images were processed with the model from equation (4.19) and the regularization parameter $\alpha = 1$. The images picture a dot-like pattern, a grid-like pattern and a random pattern using a plate model (Fieguth, 2010, Example 8.3). The brightness structures of the images are very different, especially the distributions of the image gradients that enter the cost functional. The *normal flow* is extremely dominant for the line grid image, because of the abundance of high magnitude gradients. In particular, these gradients effect the shape of the boundary control, which is less regularized than the inner parts of

the image. It makes sense to connect the regularization parameter α to the distribution of the image gradients to get a comparable regularization of the solution throughout the image and independence of the brightness structures.

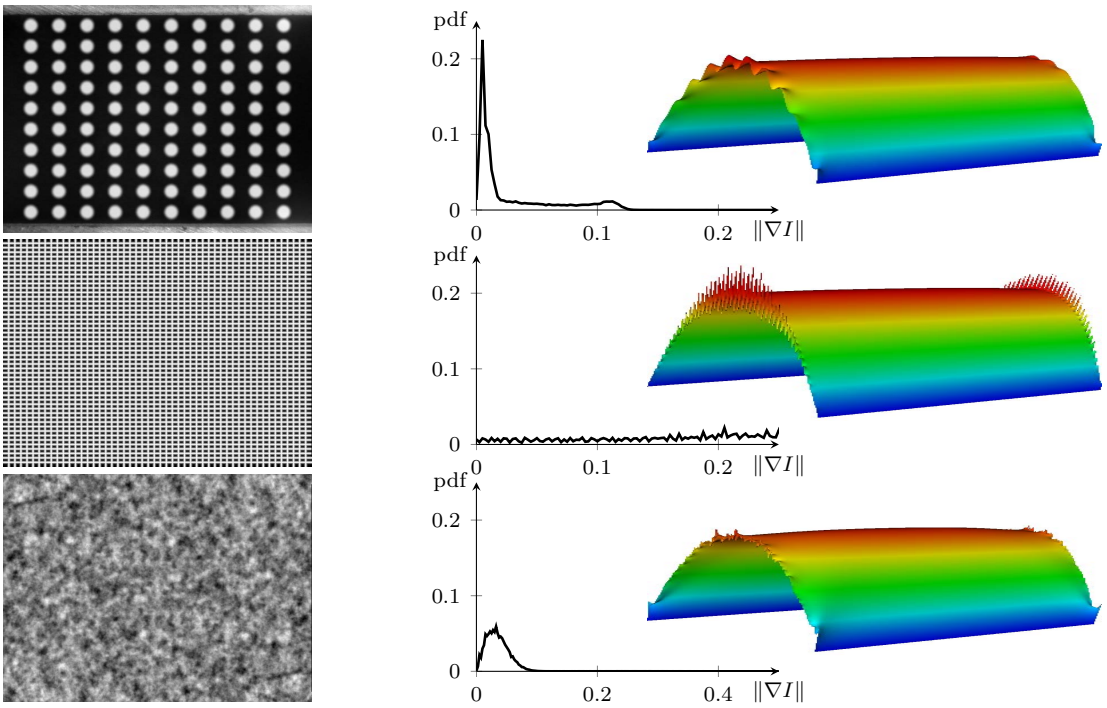

Figure A.1: This figure shows the influence of the image data onto the PDE constraint motion estimation using a boundary control. The images have very different distributions of image gradients $\|\nabla I\|$, which is shown in the histograms. This effects the boundary control differently, as it can be seen in the corresponding u-velocities.

A.8 Influence of $\partial_y I$ on the motion

As already pointed out, the spanwise image gradients contribute to the motion and have a significant influence on the boundary controlled motion estimation from section 4.3.7.1. The influence of the general brightness pattern was already demonstrated in the previous chapter A.7. Since this effect could also be caused by the streamwise gradients $\partial_x I$, the following investigation was performed. The standard BCCE from equation (3.10) was changed to prefer the streamwise gradients. This was done by scaling the spanwise gradients with the factor $c = \{0.5, 1, 2.5, 5, 10, 20\}$. The new BCCE reads

$$0 = \partial_t I + u\partial_x I + c \cdot v\partial_y I \,. \tag{A.36}$$

The factor has the effect that it balances the importance between $\partial_x I$ and $\partial_y I$. If $c > 1$, then the velocity component v is smaller than normal in order to satisfy the equation. Assuming an infinitely large $c\partial_y I$ forces v to be zero. Consequently, it is possible to

control the importance of the gradients for the motion estimates. If the oscillations of the boundary function originate from the spanwise gradients, then this effect should be reduced by choosing $c > 1$. Indeed, figure A.2 shows the boundary functions at the inlet for six different choices of the scaling parameter c and the dot and line image patterns. It can be clearly seen, that oscillations wear off with increasing c, thus approaching the shape of the parabolic profile. It also shows that the magnitude of the boundary function is hardly effected. Just for large c the cost of the gradient exceed the costs of the regularizing term and the total profile is estimated smaller. The same effect can be seen for the line pattern image. This proves, that the oscillations at the boundary are produced by the spanwise gradients.

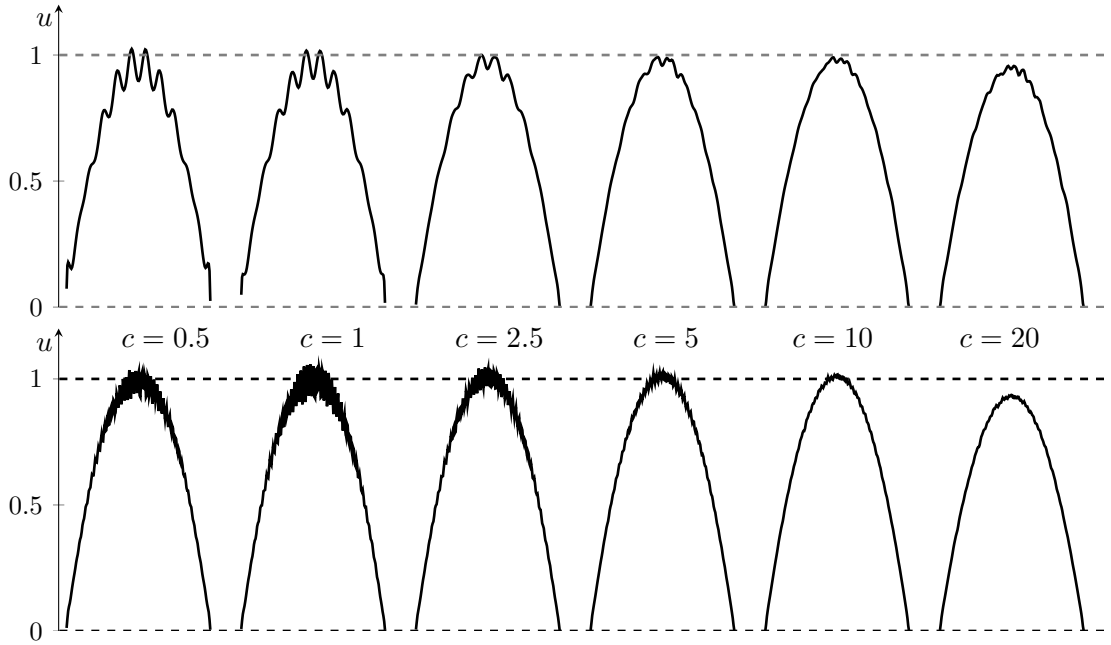

Figure A.2: This figure demonstrate the effect of the spanwise image gradient onto the estimated boundary profile for (top row) the dot pattern images and (bottom row) the line pattern images for six choice of c.

A.9 General regularized optical flow

Restricting the cost functionals to Euclidean estimators is often not appropriate. Examples are discontinuous velocity fields as they appear in images containing object motion. The L^2-norm penalizes optimal for Gaussian noise (see A.4) but this might not be always the case. Therefore, more general norms φ and ψ can be used to relax this limitation in the data term or the regularization term, respectively. The cost functional can be written as

$$J(\boldsymbol{u}) = \int_\Omega \varphi(\boldsymbol{u}^T \nabla I + \partial_t I) \mathrm{d}\boldsymbol{x} + \int_\Omega \alpha\psi(\nabla \boldsymbol{u}) \mathrm{d}\boldsymbol{x}\,. \tag{A.37}$$

Then, the minimum has to satisfy the first-order necessary condition for a variation of $\boldsymbol{u} \to \boldsymbol{u} + \varepsilon\delta\boldsymbol{u}$, which leads to

$$J'(\boldsymbol{u})(\delta\boldsymbol{u}) = \int_\Omega \varphi'(\boldsymbol{u}^T \nabla I + \partial_t I)\nabla I \delta\boldsymbol{u} \mathrm{d}\boldsymbol{x} + \int_\Omega \alpha\psi'(\nabla \boldsymbol{u})\nabla\delta\boldsymbol{u} \mathrm{d}\boldsymbol{x} = 0\,. \tag{A.38}$$

Integration by parts of the last term yields

$$0 = \int_\Omega \left\{\varphi'(\boldsymbol{u}^T \nabla I + \partial_t I)\nabla I - \nabla(\alpha\psi'(\nabla \boldsymbol{u}))\right\} \delta\boldsymbol{u} \mathrm{d}\boldsymbol{x}\,. \tag{A.39}$$

Since this has to be valid for any appropriate function $\delta\boldsymbol{u}$, the integrand has to be zero everywhere in Ω. This yields the differential equation

$$0 = \varphi'(\boldsymbol{u}^T \nabla I + \partial_t I)\nabla I - \nabla(\alpha\psi'(\nabla \boldsymbol{u}))\,. \tag{A.40}$$

Up to now, no assumption were made on α. Usually it is a scalar variable but it can be a function that weights locally the contribution of the velocity gradients. By expanding the parenthesis one finds

$$\begin{aligned} 0 &= \varphi'(\boldsymbol{u}^T \nabla I + \partial_t I)\nabla I - \psi'(\nabla \boldsymbol{u})\nabla\alpha - \alpha\nabla\psi'(\nabla \boldsymbol{u}) \\ &= \varphi'(\boldsymbol{u}^T \nabla I + \partial_t I)\nabla I - \psi'(\nabla \boldsymbol{u})\nabla\alpha - \alpha\psi''(\nabla \boldsymbol{u})\Delta\boldsymbol{u} \end{aligned} \tag{A.41}$$

which is a partial differential equation for $\boldsymbol{u}$

$$0 = \Delta\boldsymbol{u} + f(\nabla\boldsymbol{u}) + g(\boldsymbol{u}, \nabla\boldsymbol{u}) \qquad \text{with} \begin{cases} f : \nabla u & \mapsto -\frac{\psi'(\nabla u)}{\alpha\psi''(\nabla u)} \\ g : (\boldsymbol{u}, \nabla u) & \mapsto -\frac{\varphi'(u^T\nabla I + \partial_t I)}{\alpha\psi''(\nabla u)} \end{cases}. \tag{A.42}$$

Many norms have been tested for modeling but also computational reasons. The interested reader is referred to the publications Black and Anandan (1996), Bruhn et al. (2005), Weickert and Schnörr (2001b), Weickert and Schnörr (2001a) and Werlberger et al. (2009).

A.10 Well-posedness of Horn & Schunck

Theorem 3. The problem

$$\min_{\boldsymbol{u}} \|\partial_t I + \boldsymbol{u}^T \nabla I\|_\Omega^2 + \frac{\alpha^2}{2}\|\nabla \boldsymbol{u}^T\|_\Omega^2 \tag{A.43}$$

is has a unique solution for any $\alpha^2 > 0$.

Proof: The introduction of new variables allows to simplify equation (3.23): the matrix $\boldsymbol{A} = \left[\nabla I \nabla I^T + \alpha^2 \mathbb{1}\right]^{-1}$ and the vector $\boldsymbol{b} = (\alpha^2 \bar{\boldsymbol{u}} - \partial_t I \nabla I)$. Then the linear system can be written as $\boldsymbol{u} = \boldsymbol{A}\boldsymbol{b}$. The invertibility of $\boldsymbol{A}$ can be tested by calculating its eigenvalues with

$$\det(\boldsymbol{A} - \lambda \mathbb{1}) = 0\,. \tag{A.44}$$

This equation corresponds to a root-finding problem of the second-order polynomial

$$\lambda^2 + b\lambda + c = 0 \qquad \text{with} \qquad \begin{cases} b = (-{I_x}^2 - {I_y}^2 - 2\alpha^2) \\ c = \alpha^2({I_x}^2 + {I_y}^2 + \alpha^2) \end{cases}\,. \tag{A.45}$$

The roots of this quadratic equation can be calculated in a closed form and read

$$\begin{aligned} \lambda_{1/2} &= \frac{1}{2}\left({I_x}^2 + {I_y}^2 + 2\alpha^2 \pm \sqrt{({I_x}^2 + {I_y}^2)^2}\right) \\ &= \begin{cases} {I_x}^2 + {I_y}^2 + \alpha^2 \\ \alpha^2 \end{cases} \end{aligned} \tag{A.46}$$

This shows directly, that $\boldsymbol{A}$ is invertible because for $\alpha^2 > 0$ both eigenvalues are strictly positive. In particular this means that this linear system has a unique solution.

The corresponding eigenvectors $\boldsymbol{e}_{1/2}$ can be computed by solving $(\boldsymbol{A} - \lambda_{1/2}\mathbb{1})\boldsymbol{e}_{1/2} = 0$. Since $\boldsymbol{A}$ is a symmetric positive definite matrix, the eigenvectors are orthogonal and can be found by calculating explicitly the inverse of $\boldsymbol{A}$

$$\begin{aligned} \boldsymbol{A} = \left[\nabla I \nabla I^T + \alpha^2 \mathbb{1}\right]^{-1} &= \begin{bmatrix} {I_x}^2 + \alpha^2 & I_x I_y \\ I_x I_y & {I_y}^2 + \alpha^2 \end{bmatrix}^{-1} \\ &= \frac{1}{\alpha^2({I_x}^2 + {I_y}^2 + \alpha^2)} \begin{bmatrix} {I_y}^2 + \alpha^2 & -I_x I_y \\ -I_x I_y & {I_x}^2 + \alpha^2 \end{bmatrix}. \end{aligned} \tag{A.47}$$

The eigenvectors to this matrix are

$$\boldsymbol{e}_1 = \frac{I_x}{\|\nabla I\|^2} \begin{pmatrix} I_x \\ I_y \end{pmatrix} \qquad \text{and} \qquad \boldsymbol{e}_2 = \frac{I_y}{\|\nabla I\|^2} \begin{pmatrix} I_y \\ -I_x \end{pmatrix}, \tag{A.48}$$

which are indeed orthogonal.

A.11 L^2-norm of the boundary control

In the main body of this thesis, it was argued, that the L^2-norm is not appropriate to estimate the error of PDE constrained motion analysis involving boundary controls. The reason is that it cannot deal with non-Gaussian outliers, especially not with systematic outliers. Figure A.3 shows a comparison of the estimated L^1- and L^2-errors. Besides the larger magnitude of the L^2-error, there is also a severely altered dependency on the noise level. Almost all systematic relations that are visualized with L^1-errors, are lost for L^2-errors. Just for $u_{max} > 3.5$ the boundary effects, which are caused by the normal flow, loose their dominance.

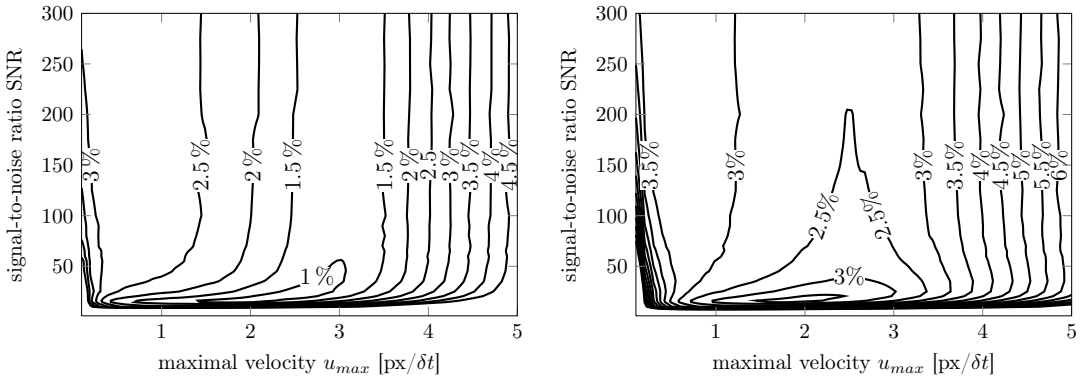

Figure A.3: This Figure shows the L^1-norm (left) and the L^2-norm (right) for the PDE constraint minimization problem including boundary control. The corresponding problem is formulated in equation (4.19).

A.12 Intensity increase of MTV images

Figure A.4 is shown to justify the introduction of a scaling parameter into the model of equation (4.32). The left graph shows the scaling parameter for each time step, as it was estimated from the dataset and the right graph shows the corresponding integrated brightness $\int_\Omega I_i \mathrm{d}x$. The pattern is written at $t = 0\,\mathrm{sec}$. The resemblance is astonishing because even extreme values of s reappear in the integrated intensity graph. It has to be mentioned, that the intensity graph appears to be shifted one frame to the left because it is calculated on a single image and not on a pair of images. The right graph illustrates the unsaturated fluorescence light that has just half of the intensity of the following image.

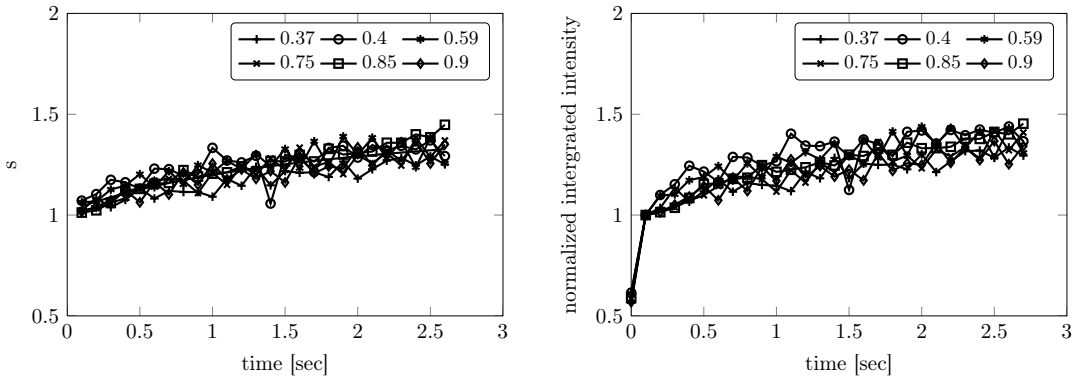

Figure A.4: These graphs show a direct comparison of the scaling parameter s from equation (4.32) (left) and the integrated image intensity over time (right).

A.13 Categorization of image motion algorithms